

## ABSTRACT

PALEOCRASSAS, ALEXANDER GRANT. Process Characterization of Low Speed, Fiber Laser Welding of AA 7075-T6 - Application to Fatigue Crack Repair. (Under the direction of Dr. Juei-Feng Tu.)

Aluminum alloys are widely used in the aerospace industry as structural materials, mainly due to their high strength to weight ratio. However, fatigue-induced cracks start to appear on aircraft components and, unless replaced or repaired, propagate to critical lengths which may result in catastrophic failure. A method that is being considered for crack repair is fusion (welding). However, aluminum alloys are some of the most challenging metals to weld successfully. Since cracks do not propagate in straight lines low speed welding is required to avoid high acceleration and deceleration effects. A process characterization was performed investigating low speed welding from 10 mm/s down to 1 mm/s. Results showed that the welding followed the expected trend until the speed dropped below a threshold ( $\sim 1$  mm/s) at which there was a significant change in the process, causing shallow, inefficient welds with many defects. Experimental evidence suggested that a large molten pool is created at low speeds. As a result, the CW laser beam mainly irradiates at the molten pool, which absorbs a large portion of the beam energy near the surface, and subsequently transfers the energy into the bulk material via more effective convection and conduction. Consequently, the welding process becomes inefficient and the welds become shallow and wide. Pulsed welding was tested as part of a hypothesis to improve the Fresnel absorption (multiple reflections) and therefore achieve deeper weld penetration without overheating the molten pool. Results showed that decreasing the average power by pulsing creates a much more efficient process; however, solidification cracking became a problem. Therefore, the best CW welding condition was applied to thinner sheets for full penetration welding and crack repair. Tensile tests showed that the best ultimate strength recovery was about 75% percent of the base material. This result is highly encouraging, considering the alloy is only 50% as strong before heat treatment. In combination with a composite patch this process might prove to be a viable solution for fatigue crack repair.

Process Characterization of Low Speed, Fiber Laser Welding of AA 7075-T6 -  
Application to Fatigue Crack Repair

by  
Alexander Grant Paleocrassas

A dissertation submitted to the Graduate Faculty of  
North Carolina State University  
in partial fulfillment of the  
requirements for the Degree of  
Doctor of Philosophy

Mechanical Engineering

Raleigh, North Carolina

2009

APPROVED BY:

---

Dr. Clement Kleinstreuer

---

Dr. Kara J. Peters

---

Dr. Pierre A. Gremaud

---

Dr. Juei-Feng Tu  
Chair of Advisory Committee

## **BIOGRAPHY**

Alexander Grant Paleocrassas was born on August 31, 1980. He grew up in Athens, Greece and attended Greek public school until freshman year in high school. He then transferred to an American/International high school, ACS, (American Community School of Athens), where he spent his sophomore, junior and senior years. The fact that his brother and sister were both alumni and the reputation of the engineering school influenced him in his decision to attend NC State University. In May 2003, he received his Bachelor of Science in Aerospace Engineering and then enrolled in the Mechatronics, Master of Science program. He received his Master of Science in Mechanical Engineering in August of 2005.

## ACKNOWLEDGMENTS

As with most major accomplishments, this research would not be possible without help from other people. First and foremost, I would like to thank Dr. Tu, who was a significant influence on me and my research. I could not have done it without his help and support. In addition to Dr. Tu, I would like to thank Dr. Kleinstreuer, Dr. Peters and Dr. Gremaud, for taking time out of their schedule to serve on my committee. Dr. Gremaud also made himself available to me for some of my modeling related questions, so I just want to express my appreciation for those extra hours as well. Additionally, I would like to say thank you to the Mechanical and Aerospace Engineering Department of NC State and the National Science Foundation for the financial support they have provided me throughout the past four years. I also owe my gratitude Dr. Tu's former colleague at Purdue University, Dr. Sun. With his help, I was able to create the fatigue cracked samples that were later repaired through laser welding. His graduate student Haiyang was also a great help in showing me the details on how to work their UTS machine. I want to also thank Ryan, Stephen, Larry, PJ, Guillaume, Annie, Fredrik, Nilesh, Ted and Brad for all their help throughout the years.

Finally, I would like to thank my family and friends for all their support. My parents, brother and sister have always been there for me, showing me their unconditional love and support, and provided me with anything I might have needed over the years. I really appreciate it and I consider myself extremely lucky to have such a great family. Some of my best friends, Alex and Marc have also been there for me providing me with great friendship. We have had a lot of great times together which have helped me stay motivated through tough times and I thank them very much for those moments. Last but not least, I would like to thank my girlfriend Susan for her love and support through some of the hardest moments of this process. I love you very much baby!

## TABLE OF CONTENTS

LIST OF TABLES .....	viii
LIST OF FIGURES .....	ix
1 INTRODUCTION	1
1.1 Motivation.....	1
1.2 Significance of the Problem.....	1
2 BACKGROUND INFORMATION	3
2.1 Aluminum Alloys.....	3
2.2 Conventional Welding of Aluminum Alloys.....	6
2.3 Laser Welding.....	7
2.4 Weld Regions.....	10
2.4.1 Fusion Zone (FZ).....	11
2.4.2 Partially Melted Zone (PMZ).....	12
2.4.3 Heat Affected Zone (HAZ).....	12
2.5 Weld Defects.....	13
2.5.1 Porosity.....	13
2.5.2 Cracking.....	15
2.5.3 Oxide Inclusions.....	17
2.5.4 Loss of Alloying Elements.....	17
2.6 Defect Minimization Techniques.....	18
2.7 Mechanical Properties of Aluminum Alloy Welds.....	20
2.7.1 Hardness.....	20
2.7.2 Tensile Strength.....	21
2.7.3 Fatigue Strength.....	22
2.8 Fiber Laser Characteristics.....	22
3 LITERATURE REVIEW IN LASER WELDING OF ALUMINUM ALLOYS	24
3.1 Weld characterization results.....	24

3.2	Fiber Laser Welding .....	25
3.3	Additional research studies .....	26
4	SPECIFIC RESEARCH OBJECTIVES	28
5	RESEARCH APPROACHES	29
6	EXPERIMENTAL APPARATUS	32
7	EXPERIMENTAL PROCEDURES	44
7.1	Determination of the Laser Beam's Focusing Position.....	44
7.2	Bead-on-Plate CW and Pulsed Laser Welding.....	45
7.3	High Speed Camera Experiments .....	47
7.4	Photodiode Relative Intensity Measurements.....	48
7.5	Spectroscopic Characterization of Vapor/Plasma Plume .....	50
7.6	Pulsed Laser Welding .....	51
7.7	Thin Plate Precision Laser Welding .....	53
7.8	Tensile Testing.....	53
8	RESULTS AND DISCUSSION	55
8.1	Process Characterization of High Brightness, Low Speed, Partial Penetration Laser Welding of AA 7075-T6.....	55
8.2	Laser Power Distribution .....	57
8.3	Idealized Welding Model.....	58
8.3.1	Model Validation: High Speed Welding of SUS 304 Steel Data .....	62
8.3.2	Data Comparison of Low Speed Welding of AA 7075-T6 .....	65
8.3.3	Process Observations .....	67
8.4	Effect of Various Focusing Positions on Low Speed Welding.....	67
8.5	Energy Based Process Characterization.....	69
8.5.1	Effective Weld Energy vs. Keyhole Fluence.....	71
8.5.1.1	“Global Efficiency” .....	73
8.5.1.2	“Local Efficiency” .....	74
8.6	Investigation of Poor Welding Efficiency at Low Speeds.....	75

8.6.1	High Speed Camera .....	76
8.6.2	Vapor/Plasma Plume Relative Intensity Measurements .....	77
8.6.3	Relationship between Penetration Depth and Vapor/Plasma plume intensity .....	78
8.6.4	Laser Beam Reflectivity Relative Intensity Measurements.....	79
8.6.5	Spectroscopic Characterization of Vapor/Plasma Plume Produced during Low Speed Laser Welding. ....	82
8.6.5.1	Electron Temperature ( $T_e$ ).....	85
8.6.5.2	Electron Density ( $n_e$ ) .....	87
8.6.5.3	Electron Temperature Estimation .....	90
8.6.5.4	Electron Density Estimation .....	94
8.6.5.5	Absorption Coefficient Estimation .....	95
8.6.5.6	Aluminum Plasma Temperature based on Measured Spectrum.....	96
8.6.5.7	Aluminum Plasma Temperatures in other studies .....	99
8.7	Pulsed Welding Experiments for the Improvement of Aspect Ratio, Efficiency and Weld Quality .....	100
8.7.1	Weld Width and Penetration Depth vs. Keyhole Fluence .....	101
8.7.2	Aspect Ratio vs. Keyhole Fluence .....	102
8.7.3	Relative EWE and “Global Efficiency” vs. Keyhole Fluence.....	104
8.7.4	Selecting Best Pulsed Welding Condition .....	105
8.7.5	Vapor/Plasma Plume Intensity comparison: CW vs. Pulsing.....	106
8.8	Non-zero Low Power Pulsing Tests as a Potential Solution to Solidification Cracking.....	110
8.9	Thin Sheet Full Penetration Laser Welding for Crack Repair.....	112
8.9.1	Process Uncertainty in Full Penetration, Thin Sheet, Bead-on-Plate Laser Welding.....	113

8.9.2	Thin Sheet Crack Repair using Low Speed, Full Penetration Laser Welding .....	120
8.9.3	Mechanical Testing: Bead-on-Plate Weld Strength and Repaired Crack Strength .....	122
9	SUMMARY	125
10	FUTURE WORK	128
11	REFERENCES	130
REFERENCES .....		138
1.1	Aluminum Grinding and Polishing.....	139
1.2	Matlab Code.....	140
1.2.1	Aluminum Alloy 7075-T6 Penetration Model.....	140
1.2.2	Temperature Distribution Model .....	141
1.2.3	SUS 304 Penetration Model.....	143
1.2.4	Beam Profile .....	144

## LIST OF TABLES

Table 3.1: Experimental Studies of Laser Welding of Aluminum Alloys.....	27
Table 8.1: Cr I and Fe I Atomic Spectral Line Data.....	91
Table 8.2: Electron temperatures calculated from Boltzmann plots using two sets of lines.....	93
Table 8.3: Electron densities for various processing conditions based on Stark electron broadening of Fe I (381.58) .....	95
Table 8.4: Absorption coefficients for various processing conditions .....	95

## LIST OF FIGURES

Figure 3.1: Schematic of Keyhole Welding (Lankalapalli, Tu, <i>et al.</i> , 1996).....	9
Figure 6.1: 300 W Ytterbium, single-mode fiber laser power unit.....	32
Figure 6.2: Optical isolator connection to collimator, used to divert away reflected laser light into a beam dump.....	33
Figure 6.3: XY Linear motors with attached work plate fixture.....	34
Figure 6.4: Galil X-Y axes motion controllers .....	34
Figure 6.5: dSPACE 4.0 data acquisition system .....	35
Figure 6.6: Beam expander and laser head setup.....	37
Figure 6.7: X,Y, Z micrometer linear stages .....	38
Figure 6.8: Tektronix 3012B oscilloscope.....	39
Figure 6.9: Zeiss Inverted Microscope .....	40
Figure 6.10: Saphir 520 Grinder / Polisher.....	41
Figure 6.11: Ocean Optics HR4000 spectrometer .....	42
Figure 6.12: Hamamatsu Si S1336-18BQ photodiode .....	43
Figure 7.1: Spot welds or holes at different focusing locations.....	45
Figure 7.2: Initial bead-on-plate Welding Aluminum Plate Setup .....	46
Figure 7.3: High Speed Camera Experimental Setup .....	47
Figure 7.4: Photodiode Experimental Setup .....	49
Figure 7.5: Spectroscopic experimental setup .....	51
Figure 7.6: Laser pulse shape diagram for non-zero, “low” power pulsing .....	53
Figure 8.1: Keyhole Profile (Lankalapalli, Tu, <i>et al.</i> , 1996) .....	59
Figure 8.2: Variation of Penetration with Change in Péclet Number .....	62
Figure 8.3: Melting Point Isotherms of SUS 304 Steel @ Péclet = 1.....	64
Figure 8.4: Theoretical vs. Experimental Penetration in SUS 304.....	65
Figure 8.5: Data Comparison at Low Speed Welding of AA 7075-T6 .....	66

Figure 8.6: Effects of Variation of Focusing Position on Penetration for Different Welding Speeds .....	68
Figure 8.7: Schematics showing the submerged beam surface area ( $A_b$ ), the weld's cross-sectional area ( $A_w$ ) and the profile radius ( $r_{profile}$ ) .....	71
Figure 8.8: Variation of Effective Weld Energy with respect to Keyhole Fluence.....	73
Figure 8.8: High speed camera stills; Rows from top to bottom: 0.5, 1, 2, 4 and 10 mm/s.....	76
Figure 8.9: Vapor/Plasma Plume Intensity Measurements.....	78
Figure 8.10: Relationship between Penetration and Average Vapor/Plasma Intensity ....	79
Figure 8.11: Laser beam reflectivity relative intensity; From top to bottom: 10, 4, 2 and 1 mm/s welding conditions respectively .....	81
Figure 8.12: Aluminum Vapor/plasma spectrum for 1 $\mu$ s pulsing, 100 % power (~ 1,500 W) .....	83
Figure 8.13: Vapor/plasma spectrum for 1 $\mu$ s pulsing, 100 % power (~ 1,500 W).....	92
Figure 8.14: Boltzmann plot for 1 $\mu$ s pulsing, 100 % power (~ 1,500 W).....	93
Figure 8.15: Zoomed in aluminum vapor/plasma spectrum for 1 $\mu$ s pulsing, 100 % power (~ 1,500 W).....	97
Figure 8.16: Boltzmann plot for aluminum vapor/plasma spectrum for 1 $\mu$ s pulsing, 100 % power (~ 1,500 W).....	98
Figure 8.17: Pulsed Welding Cross-Sections for Pulse Durations ranging from 0.5 – 1000 ms.....	100
Figure 8.18: Variation of Weld Width and Penetration Depth with increasing Keyhole Fluence .....	101
Figure 8.19: Variation of Aspect Ratio with Increase in Keyhole Fluence.....	103
Figure 8.20: Variation of EWE and “Global Efficiency” with Increase in Keyhole Fluence.....	104

Figure 8.21: Comparison of CW with pulsed laser welding; From top to bottom: 10 mm/s CW, 1 mm/s CW, 1 mm/s, 200 ms pulsing period, 50% duty cycle (100 ms pulse duration).....	107
Figure 8.22: A closer look at the pulsed welding vapor intensity (T = 200 ms) .....	109
Figure 8.23: Cross-sections for 10 mm/s CW, 1 mm/s CW and 100 ms pulsed welding conditions .....	110
Figure 8.24: Pulsed Welding Cross-Sections for 10 ms Pulse Duration Welds with Various Low Power Percentages Ranging from 12.5-90 % .....	111
Figure 8.25: Top view of first attempt of a thin sheet, full penetration, bead-on-plate weld.....	113
Figure 8.26: Top view of inconsistent, thin-sheet, full penetration, bead-on-plate welds .....	115
Figure 8.27: Cross-sectional view of inconsistent, thin sheet, full penetration, bead-on-plate welds .....	116
Figure 8.28: Initial fixturing method for thin sheet, full penetration, bead-on-plate welding.....	117
Figure 8.29: Modified fixturing method for thin sheet, full penetration, bead-on-plate welding.....	118
Figure 8.30: Top view of consistent, thin sheet, full penetration, bead-on-plate weld....	119
Figure 8.31: Cross-sectional view of a consistent, thin sheet, full penetration, bead-on-plate weld.....	120
Figure 8.32: Single-pass laser welded fatigue crack.....	121
Figure 8.33: Double-pass laser welded fatigue crack .....	122
Figure 8.34: Base AA 7075-T6 compared to single and double pass bead-on-plate welds .....	123

# 1 INTRODUCTION

## *1.1 Motivation*

Aluminum alloys are widely used as structural materials mainly due to their high strength to weight ratio. The aerospace and automobile industries are two examples where aluminum alloys are the preferred materials. Especially in the aerospace industry, it is important to reduce the weight of aircraft as much as possible. However, despite their high strength and ductile characteristics aluminum alloys are susceptible to fatigue failure. After several thousand flights, fatigue-induced cracks start to appear on aircraft components and, unless replaced or repaired, propagate to critical lengths which may result in catastrophic failure. Hence, when aircraft parts have cracks that surpass a certain critical length, they are usually replaced or at best repaired by lightweight composite patches, which can extend the part's fatigue life. Replacing parts every so often can be very costly and the composite patches have had limited success in increasing the fatigue life. Another method that is being considered for crack repair is fusion (welding). The challenge is that aluminum has been known to be one of the most challenging metals to weld successfully. Some of the factors affecting the welding quality of aluminum alloys include high reflectivity, different kinds of porosity formation, hot tearing, solidification cracking, oxide inclusions and loss of alloying elements.

## *1.2 Significance of the Problem*

Laser welding offers several advantages over conventional welding particularly at high speeds. However, it is often not feasible to use high speed laser welding to repair cracks because, in general, fatigue cracks do not propagate in straight lines. In order to trace the

crack there is a constant need to accelerate and decelerate to change directions, which makes high speed welding not practical. However, low speed welding poses additional problems and overcoming them is not trivial. Therefore, it is of interest to establish an economical and efficient aluminum low speed laser welding process that will not only create welds with adequate penetration, but will also be able to repair cracks successfully by ensuring minimal to no defects.

## 2 BACKGROUND INFORMATION

In this section, the related aspects of laser welding aluminum are discussed. Initially, aluminum alloys and their material properties are discussed, in order to develop a good understanding of their behavior under specific conditions (i.e. rapid heating by a laser). The next section describes what different aluminum welding techniques exist today, listing advantages and disadvantages between conventional (MIG, TIG, etc.) and laser (CO<sub>2</sub> and Nd:YAG) welding. Laser welding of aluminum is then discussed in more detail, to identify current processes, results and obstacles (defects in welds, etc.). Finally, the characteristics of fiber lasers are discussed and their advantages over traditional lasers.

### 2.1 *Aluminum Alloys*

Aluminum alloys are light-weight, have relatively high strength, retain good ductility at subzero temperatures, have high resistance to corrosion, and are non-toxic. They have a melting range between 482 and 660 °C, depending upon the alloy. There is discoloration in the alloys when heated to the welding temperature range. They have high electrical and thermal conductivity (compared to steel) and they rapidly develop oxide films when exposed to air. Other important properties of aluminum alloys include high reflectivity, hydrogen solubility, high thermal expansion and solidification shrinkage (Mandal, 2002).

There are international standards based on which aluminum alloys are designated. These alloys are distinguished by a four-digit number, which is followed by a temper designation code. The first digit corresponds to the principal alloying constituent(s). The second digit corresponds to variations of the initial alloy. The third and fourth digits

correspond to individual alloy variations. Finally the temper designation code corresponds to different strengthening techniques (ibid).

1xxx—Pure Al (99.00 % or greater)  
2xxx—Al-Cu Alloys  
3xxx—Al-Mn Alloys  
4xxx—Al-Si Alloys  
5xxx—Al-Mg Alloys  
6xxx—Al-Mg-Si Alloys  
7xxx—Al-Zn Alloys  
8xxx—Al + Other Elements  
9xxx—Unused Series

Temper Designation System:

F → As fabricated  
O → Annealed  
H → Strain-Hardened  
W → Solution heat-treated  
T → Thermally treated to produce stable tempers other than F, O, or H

Subdivisions of T Temper, thermally treated:

T1 → Naturally aged after cooling from an elevated temperature shaping process, such as extruding.  
T2 → Cold worked after cooling from an elevated temperature shaping process and then naturally aged.  
T3 → Solution heat-treated and naturally aged.  
T5 → Artificially aged after cooling from an elevated temperature shaping process.  
T6 → Solution heat-treated and artificially aged.  
T7 → Solution heat-treated and stabilized (over aged).  
T8 → Solution heat-treated, cold worked and artificially aged.  
T9 → Solution heat-treated, artificially aged and cold worked.  
T10 → Cold worked after cooling from an elevated temperature shaping process and then artificially aged.

Aluminum alloys can be separated into two major categories: Non heat-treatable and heat-treatable. The initial strength of non heat-treatable alloys depends primarily upon

the hardening effect of alloying elements such as silicon, iron, manganese and magnesium. The non heat-treatable alloys are mainly found in 1xxx, 3xxx, 4xxx and 5xxx series. Additional strength is usually achieved by solid-solution strengthening or strain hardening (ibid).

The initial strength of heat-treatable alloys depends upon the alloy composition, just as the non heat-treatable alloys. In order to improve their mechanical properties they need to undergo solution heat treating and quenching followed by either natural or artificial aging (precipitation hardening). This treatment involves holding the work piece at an elevated temperature and followed by controlled cooling in order to achieve maximum hardening. The heat-treatable alloys are found primarily in the 2xxx, 6xxx and 7xxx alloy series (ibid).

The 7xxx series alloys contain zinc in amounts between 4 and 8 % and magnesium in amounts between 1 and 3 %. Both have high solid solubility in aluminum. The addition of magnesium produces a marked increase in precipitation hardening characteristics. Copper additions between 1 and 2 % increase the strength by solid solution hardening, and form the basis of high strength aircraft alloys. The addition of chromium, typically up to 0.3 %, improves stress corrosion cracking resistance. The 7xxx series alloys are used predominantly in aerospace applications, 7075-T6 being the principal high strength aircraft alloy (Ion, 2000). Research will be focused more on this alloy's characteristics after laser welding has been performed, mainly because of its applicability in aircraft components.

## 2.2 *Conventional Welding of Aluminum Alloys*

There are many different types of conventional welding suitable for aluminum welding. These include oxyacetylene welding, shielded metal arc welding, gas-tungsten arc welding, plasma arc welding, gas-metal arc welding, flux-core arc welding, submerged arc welding, electroslag welding, electron beam welding, resistance spot welding (Kou, 2003). Of these techniques the most popular are oxyacetylene welding (OAW), gas-tungsten arc welding (GTAW), gas-metal arc welding (GMAW) and electron beam welding (EBW). GTAW is a process that melts and joins metals by heating them with an arc established between a non-consumable tungsten electrode and the metals. OAW is the most commonly used gas welding process due to its high flame temperature. The main difference between GTAW and GMAW is that GMAW uses a continuously fed filler wire as an electrode instead of tungsten. These welding processes use inert gases such as argon and helium to provide shielding of the arc and the molten weld pool. This is why GTAW and GMAW are also called tungsten-inert gas (TIG) and metal-inert gas (MIG) welding processes, respectively. EBW is a process that melts and joins metals by heating them with an electron beam. These electrons are accelerated by an electric field between a negatively charged bias electrode and the anode. They pass through a hole in the anode and are focused by an electromagnetic coil to a point at the workpiece surface (ibid). EBW is characterized by high power densities (as high as  $10^{10}$  W/m<sup>2</sup>), which enables it to use a deep penetration welding method called keyholing. EBW should probably be categorized with laser beam welding, since the power densities are much higher than conventional welding.

The conventional welding techniques are usually desirable due to their simplicity, low cost, portability (in most types) and are generally used in maintenance, repair and field construction sites (ibid). On the other hand, some of the disadvantages associated with

conventional welding, are the low aspect ratios compared to electron and laser beam welding, the large heat affected zone, high distortion and slower welding speeds.

### **2.3 Laser Welding**

Laser welding is a process that melts and joins metals by heating them with a laser beam. The laser beam can be produced either by a solid-state laser or a gas laser. In either case, the laser beam can be focused and directed by optical means to achieve high power densities. In a solid-state laser, a crystal is doped with small concentrations of transition elements or rare earth elements. For instance, in a Nd:YAG laser the crystal of yttrium-aluminum-garnet (YAG) is doped with neodymium. The electrons of the dopant element can be selectively excited to higher energy levels through exposure to high-intensity flash lamps or light emitting diodes (LEDs). Lasing occurs when these excited electrons return to their normal energy state by emitting energy in the form of light (ibid).

Out of all the welding techniques that exist today, laser welding is one of the most promising metal joining methods because it provides high productivity, high weld quality, high welding speed, high weld aspect ratio, low heat input, low distortion, manufacturing flexibility and ease of automation (Cao, *et al.*, 2003b). According to a study on phase transformations in weldments (Cieslak, 1992), solidification rates of  $10^2$  to  $10^3$  °C/sec encountered in conventional arc welding processes, are much lower compared to high-energy density laser processes which reach  $10^5$  to  $10^6$  °C/sec as a result of low heat input experienced at high travel speeds. Under these processing conditions the weld metal microstructure may bear no resemblance to that expected as the result of arc welding. Consequently, the weldment (specifically the fusion zone) is mostly comprised by fine-grained microstructures.

There are two fundamental modes of laser welding: a) conduction welding and b) keyhole or penetration welding. The main difference between these two modes is that the surface of the weld pool remains unbroken during conduction welding and opens up to allow the laser beam to enter the melt pool during keyhole welding. In keyhole welding, the molten metal vaporizes, forming a cavity in the molten pool due to the recoil and vapor pressure which are counteracted by the surface tension and hydrostatic and hydrodynamic pressures (trying to close the keyhole). Once this cavity is formed, the laser absorption is enhanced due to multiple reflections in the keyhole walls. This is called Fresnel absorption. Figure 3.1 shows a visualization of keyhole welding. Conduction welding offers less perturbation to the system because laser radiation does not penetrate into the material being welded. As a result, conduction welds are less susceptible to gas entrapment (porosity) during welding. With keyhole welding, intermittent closure of the keyhole can result in porosity (Duley, 1999).

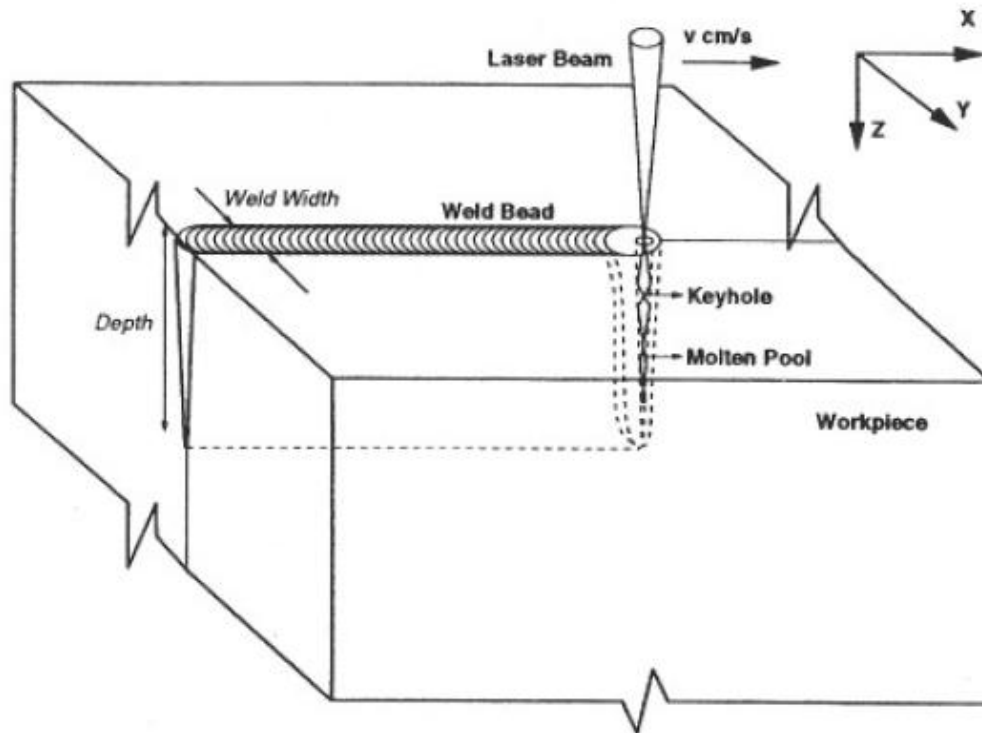


**Figure 3.1: Schematic of Keyhole Welding (Lankalapalli, Tu, *et al.*, 1996)**

Since maximum penetration depth, as well as high aspect ratio (depth to width ratio) welds are desired, keyhole welding is the welding mode of choice for this study. In general, it is more difficult to generate keyhole mode welding in aluminum alloys as compared to steel, due to their high reflectivity and high thermal diffusivity. This problem must be overcome by sufficient laser power and proper focusing, in order to achieve the required power density.

One of the most important parameters affecting laser weldability of aluminum is penetration. In order to create any penetration at all, the laser beam's power density must surpass a certain threshold above which the molten aluminum reaches its vaporization temperature. Due to its high reflectivity, aluminum requires a relatively high power

density in order to be able to create a keyhole, which is approximately of the order of  $10^6$ - $10^7$  W/cm<sup>2</sup>. Power densities of this magnitude are easily achieved with commercially available CO<sub>2</sub> lasers; however, considerations must include spot size at focus, as well as maximum power output (Martukanitz and Smith, 1995). The absorptivity of a material also has to be taken into account and is a function of the laser beam's wavelength. Typically, lower wavelength lasers have demonstrated higher absorptivity with metallic surfaces. This is an advantage the fiber laser has over CO<sub>2</sub>, in addition to a better beam profile (nearly perfect Gaussian distribution) and therefore better focusability (down to 9 μm). However, there are other factors that affect penetration such as welding speed. According to a mathematical model for estimating penetration (Lankalapalli, Tu, *et al.*, 1996)—which used two dimensional heat conduction and conical keyhole geometry among its major assumptions—the depth of the weld is related to incident power, thermal conductivity of the material, the difference between the vaporization temperature of the material and room temperature and a quantity called the Péclet number. Essentially, the Péclet number is the product of the welding speed and keyhole radius divided by twice the thermal diffusivity of the material.

#### **2.4 Weld Regions**

During laser welding there are three different regions that are produced, the fusion zone (FZ), the partially melted zone (PMZ), and the heat affected zone (HAZ). These regions have been categorized based on the temperatures that occur during welding. The thickness of these three zones put together is usually much narrower than conventional welding techniques (Cao, *et al.*, 2003b).

### 2.4.1 Fusion Zone (FZ)

The material in the fusion zone is completely melted during welding with temperatures surpassing the liquidus temperature of the alloy. According to a study performed on laser welding alloy A6061-T6 (Hirose, *et al.*, 1999) with a CO<sub>2</sub> laser, the FZ was found to be approximately half the width of what it was in TIG welded joints. The defects found in this region are usually porosity, solidification cracking and sometimes loss of alloying elements (Cao, *et al.*, 2003b). Contrary to casting processes in which a large fraction of equiaxed grains is encountered, the grain structure in laser-welded alloys (5xxx and 6xxx) primarily consists of fine columnar dendrites, originating from the fusion line and some equiaxed grains in the weld center. Higher travel speeds lead to a more elongated weld pool which leads to finer dendrite structures and grain sizes, resulting from low heat input. Also, columnar grains grow approximately normal to the welding direction at higher speeds. In contrast, lower welding speeds cause columnar grains to curve away from the normal and they align themselves with the welding direction eventually. Therefore, as has been observed, there is a decrease in ductility with increase in welding speed. Also, columnar grain structures are very susceptible to hot tearing. Equiaxed grains are more desirable because they are isotropic. They increase weld strength, reduce susceptibility to solidification cracking because of better resistance to crack formation and propagation (Gaumann and Kurz, 1998). As a result, research and development efforts are directed toward obtaining fine-grained equiaxed growth during laser welding. There are several ways to promote this transition from columnar to equiaxed growth: a) decreasing the solidification rate or welding speed, b) decreasing temperature gradient in the weld pool (by preheating or increasing size of melt pool), c) adjusting chemical composition (higher initial solute concentration), d) decreasing nucleation under cooling and e) increasing number of nucleation sites (*ibid*). During solidification, rejection of solute atoms ahead of the solid or liquid solidification front requires adequate time for diffusion. The faster the solidification rate, the greater the probability that solute atoms

will be trapped within the growing solid. Thus it is expected that the segregation in laser welds is not serious. However, laser-welded joints are characterized by high degrees of anisotropy. Inhomogeneity will have important effects on mechanical properties and service (Cao, *et al.*, 2003b).

#### 2.4.2 *Partially Melted Zone (PMZ)*

The PMZ experiences temperatures between eutectic and liquidus temperatures of the alloy (Zhao, *et al.*, 1999). Therefore, the low melting point eutectic phases which commonly exist at the grain boundaries of recrystallized grains remelt during laser welding. Liquation cracking may occur along the weakened grain boundaries in the PMZ. The PMZ in laser welded aluminum alloys is generally narrow approximately one or two grains wide (*ibid.*).

#### 2.4.3 *Heat Affected Zone (HAZ)*

The HAZ is the outermost area of the three and is characterized by its softness. This softened region is defined as the area where hardness values fall below 90% those of the base metal. It experiences temperatures below the eutectic temperatures of the alloy. No bulk metal melting occurs. It has been shown that the widths of softened regions in the HAZs of the laser welds are of the order of one seventh to one quarter those for TIG welds (Hirose, *et al.*, 1999). Although the HAZs of laser-welded joints are very narrow, many solid-state reactions such as grain growth and precipitate coarsening may occur in the zone. In non heat-treatable aluminum alloys, softening occurs because of localized annealing in HAZ by grain growth or loss of strain hardened structure. However, in heat-treatable alloys, welding heat will destroy the temper in the HAZ. Softening in

precipitate-hardenable alloys involves the dissolution of strengthening phases and formation and growth of non-strengthening phases (Guitierrez, *et al.*, 1996).

## 2.5 *Weld Defects*

In laser welded joints there is a variety of defects that can occur. A deep hole made in liquid is principally unstable, which is likely to lead to characteristic defects or unstable phenomena in laser welding. Also, the thermal cycle of laser welding is extremely high and hence the solidification rate of the weld pool becomes very rapid, which enhances the formation of cracking (Matsunawa, 1994). The understanding of these defects—how they occur and how they affect the mechanical properties of the joint—is imperative in order to improve the quality of the welds. There are four major categories in which defects can be classified: a) porosity, b) cracking, c) inclusions and d) loss of alloying elements. These categories can be broken down further into subcategories, like for example hydrogen porosity, oxide inclusions, and so on (Cao, *et al.*, 2003b).

### 2.5.1 *Porosity*

Hydrogen porosity: Hydrogen is very soluble in aluminum and its alloys. Most gas porosities precipitated in aluminum alloys are attributed to hydrogen. The solubility of hydrogen in liquid aluminum is an exponential function of temperature, which is why its porosity is a much bigger problem in laser welding (than in conventional welding) due to increased temperatures. Also, the high cooling rate is very unfavorable because it does not allow for diffusion or floatation of the trapped hydrogen. Normal hydrogen levels in molten Al vary from approximately 0.10 to 0.40 mL/100g. It is worth noting here that in order for a part to pass aerospace quality inspections, the gas contents have to be less than

0.06 mL/100g. There possibly exists a critical welding speed at which formation and growth of hydrogen porosity can be prevented. Also, another way to reduce hydrogen porosity is to increase power density, because it keeps the keyhole stable, increases solidification time, allowing the hydrogen to escape (Cao, *et al.*, 2003b). Another thing to keep in mind is that hydrogen porosity can depend on the alloy's composition.

According to a study conducted on porosity formation (Kutsuna and Yan, 1998), the rate of hydrogen porosity shows a tendency to rise considerably as the magnesium content increases. This happens because magnesium in aluminum alloys raises the hydrogen solubility in the molten pool and hence the segregation of magnesium enhances the segregation of hydrogen during solidification. In other words, aluminum alloys containing a large amount of magnesium will have higher hydrogen solubility in the liquid phase than pure aluminum, since magnesium itself has a higher hydrogen solubility than aluminum. During solidification a large quantity of hydrogen generates gas bubbles at the solid-liquid interface, interacting with the segregated magnesium.

*Porosity caused by collapse of unstable keyholes:* Even with the proper control of the material surface preparation, laser parameters, shielding gas and material compositions, aluminum alloys are susceptible to random blowholes while laser welding (Weeter, 1998). Keyhole instability and the coupling of the laser beam into the metal are suspected to cause these random events. These blowholes have irregular or turbular form and are large enough to be visible with x-ray analysis (Dausinger, *et al.*, 1997). They are usually located in the keyhole path, whereas hydrogen pores are more or less equally distributed with slight enrichment at the melting line. The number of cavities is strongly influenced by processing parameters such as the power per unit welding depth, focusability and wavelength. Most likely, stability is increased with the shorter wavelength lasers (Nd:YAG) because the beams are not as drastically affected by the weld plume as the beams with larger wavelengths (CO<sub>2</sub>). In the latter case, the weld plume periodically blocks the beam from impinging on the metal and thus causes an

instability in the keyhole. The shorter wavelength laser beams can pass through the plume and can provide a more consistent heat input into the metal (Weeter, 1998). It has also been observed that the highest level of porosity is concentrated in the regions where an unstable keyhole is formed. They are mainly composed of metal vapor but will condense at room temperature. The way to reduce this type of porosity is to keep the keyhole stable, but this can be achieved by welding at high speeds and the addition of filler wire. Also, the use of high-power continuous wave (CW) can improve the stability of keyholes (Cao, *et al.*, 2003b).

### 2.5.2 Cracking

Aluminum alloys exhibit a strong propensity for welding crack formation because of their large solidification temperature range, high coefficient of thermal expansion, and large solidification shrinkage. The restrained contraction of a weld during cooling sets up tensile stresses in the joint which may cause cracking. There are two types of hot cracking: cracking that occurs in the weld FZ during solidification of the weld metal is known as solidification cracking, whereas cracking that takes place in the PMZ due to tearing of the liquate is called liquation cracking (Zhao, *et al.*, 1999).

Solidification cracking: Solidification cracking occurs at high temperatures above the solidus under circumstances where the material has low ductility and is under high contraction stresses. Solidification of the liquid weld metal begins at one temperature (the liquidus) and completes at a somewhat lower temperature (the solidus). Between the two levels the alloy forms an incompletely solidified mass which is brittle and has little or no ductility until cooled to lower temperatures. The brittleness is present in liquid films which surround the solidifying grains or dendrites and when subjected to the high transverse contraction stresses, during weld cooling, solidification cracking may result in

the film boundaries; usually those near the centerline of the weld which are the last to cool. If the materials are prone to cracking and the addition of suitable elements (filler wire, powder metal, etc.) to modify the weld is not possible, partial penetration welds should be avoided and, where possible, modifications to the joint design should be made to reduce the weld contraction stresses on cooling. Also, to combat contraction stresses if possible, the weld faces should be held together under pressure during the weld cycle (Dawes, 1992). Certain special features are commonly observed when solidification cracking occurs: a) the fractured surface is always dendritic in nature, b) fracture usually occurs at the grain boundaries, c) the crack tip is dull, and d) the fractured surface is usually covered with oxides if the crack reaches the specimen surface where it can be exposed to oxygen, otherwise it has a silvery color characteristic of unoxidized metal (Zhao, *et al.*, 1999).

These cracks are detrimental to the integrity of the weld since they form areas of high stress concentration and will significantly reduce the strength of the weld, probably leading to catastrophic failure. Preventing solidification cracks will be one of the key challenges in this research study.

*HAZ liquation cracking:* The low melting point grain boundary films may also be present in the HAZ and may melt and form fine cracks under the influence of thermal stresses induced during welding (Dawes, 1992). Liquation cracking usually takes place in heat-treatable alloys as a result of the large quantities of alloying additions that are available to form eutectic phases with low melting points. The liquate (melt) will tear if sufficient stress is present, especially in high heat input conditions. Liquation cracking can be reduced by minimizing heat input and small HAZ and PMZ. However, liquation cracking still needs to be further investigated in laser welding of aluminum alloys in which alloy composition, cooling rate, material thickness, and weld geometry may all influence cracking susceptibility (Cao, *et al.*, 2003b).

### 2.5.3 Oxide Inclusions

Oxides are one of the main types of inclusions in aluminum alloys. During keyhole laser welding, because the vaporization of alloying elements in keyholes is not uniform and keyhole positions vary with time, the inherently unstable keyhole flow may entrap shielding gas or even air because of imperfect gas shielding (Matsunawa, *et al.*, 1998). The shielding gas cannot be truly pure. Therefore, some oxide particles may occur in the keyhole vapor. The surface of liquid metal in weld pools (strictly speaking, the surface here should be referred to as the interface between the liquid metal in the weld pool and metal vapor or shielding gas) may also be partly oxidized to form oxide films because of the entrapment of air or shielding gas into the pools. Depending on the Mg contents in Al alloys, oxides such as  $\text{Al}_2\text{O}_3$ ,  $\text{Al}_2\text{MgO}_4$ ,  $\text{MgO}$ , or their combination may occur. When aluminum alloys contain magnesium, because it is surface active in liquid aluminum, the oxidizing tendency of the molten aluminum increases rapidly with magnesium contents. When the aluminum alloys contain a trace of magnesium, a mixed oxide ( $\text{MgAl}_2\text{O}_3$ ), spinel, is formed. When the magnesium content of the alloy exceeds approximately 2%, the liquid oxidizes rapidly to form  $\text{MgO}$ . The oxides entrained into welded metal because of surface turbulent flow in welding are referred to as young oxide. Oxides in base metal originally from primary processing of aluminum alloys are termed old oxides.

### 2.5.4 Loss of Alloying Elements

The high power density used for laser welding may cause selective vaporization of some alloying elements with a low fusion point such as lithium, magnesium, and zinc because of their higher equilibrium vapor pressure than aluminum. Selective vaporization of alloying elements can take place in both keyhole and conduction mode laser welding. The vaporization mechanism is divided into three stages. The first involves transport of

vaporization elements from the bulk to the surface of the molten weld pool. Then the vaporization of elements occurs at the liquid/vapor interface, and finally the vaporized species are transported into the surrounding gas phases (Cao, *et al.*, 2003b). This will also cause a void on the top of the weld called underfill. It was found that the intrinsic vaporization of alloying elements at the weld pool surface controls the overall vaporization (Zhao, *et al.*, 1999).

## **2.6 Defect Minimization Techniques**

Some techniques have been developed that minimize the defect formations in the weld seams. Some of these include variable welding speeds, variation of power, use of shielding gases, filler metals etc. However, it is also true that using one technique might minimize one type of defect, but can be the cause of several others. For example, porosity can be minimized by keeping the keyhole stable (only achievable during high speed welding) and high power density input. However, high power density can lead to liquation cracking, while high speed welding decreases penetration and keeps the grain growth columnar, which is more susceptible to hot tearing. Also, these effects vary with different alloys and different types of heat sources (lasers). Therefore, it is imperative to find a balance of these techniques that would produce the highest strength welds.

Based on a study that was conducted to develop porosity prevention procedures it was concluded that with high welding speed, the amount of porosity was reduced and sometimes produced no pores. Also, full penetration welding, pulse-modulated welding, welding in vacuum or under low pressure welding with tornado nozzle were reported to be able to reduce or suppress porosity. Finally, it was also reported that the forward welding with about 15 to 20 deg. of beam inclination was able to reduce porosity (Katayama, *et al.*, 2003). However, these approaches are not completely effective.

The loss of alloying elements can be minimized by controlling the beam power density distribution during continuous wave (CW) laser welding, which can influence the temperature of the molten metal in the welding pool (Cao, *et al.*, 2003b). Another way of reducing this loss is through the use of filler metal, which is used as an auxiliary source of material to fill the gap. It also provides a means of controlling the metallurgy of the weld bead and ensures weld quality (Ion, *et al.*, 2001), by helping replenish the loss of alloying elements and also prevent solidification cracking. However, there are some drawbacks involved with this method. Firstly, welding with a filler wire requires an increase in heat input, which is a function of air gap width, due to the larger melt volume produced. The use of filler metal in laser welding is justified only if the joint gap and sheet metal thickness is larger than the beam and loss of alloying elements is significant (Molian, 2004). The melting efficiency is reduced if the wire is fed to at a higher or lower position compared with the optimum, which is the focal point. An offset from the focal point of 2 mm reduces the efficiency by 35 % and an offset of 4 mm produces a reduction of 50 % in efficiency. In the case that the filler wire is too thick, powder metal can also be used (Salminen, *et al.*, 1994). Some skepticism remains about the process, mainly because it is considered to be complex and requires high precision. The interactions between the large number of process variables involved are also not well understood (Ion, *et al.*, 2001).

A shielding gas flow coaxial with the laser beam or impinging on the laser from the sides serves several purposes and is a common feature in laser welding systems. The first role of this gas often is to prevent oxidation of the weldment and creation of slag in the vicinity of the fusion zone. A second, and critical function is to suppress plasma formation in the vapor over the weld zone and to blow away any plasma that may be created in the welding process. The latter role ensures that the laser beam can reach the weld zone with minimal interruption, thus improving weld quality and enhancing the

uniformity of such factors as penetration depth and weld bead profile. It is not unusual to have both coaxial and side flow gas nozzles directing gas at the weld region (Duley, 1999).

Helium and Argon are commonly used as shielding gases, with He the gas of choice because of its high ionization potential and resistance to breakdown. Nitrogen also is commonly used as a replacement for He and has many of the same properties but is much cheaper. Gas flow rates are typically 10-40 l/min, with the higher rates necessary for high-speed welding (>10 m/min) (ibid).

## ***2.7 Mechanical Properties of Aluminum Alloy Welds***

The most important goal of laser welding fatigue cracks in aluminum alloys is to ensure that the mechanical properties of the weld are not significantly deteriorated compared to the rest of the part. This is especially important when dealing with aerospace components, because they have been designed with very low safety factors in order to minimize weight. If the mechanical properties of the welds are significantly less than what the part has been designed for, there is a serious concern for catastrophic failure originating from the weld seams. Therefore, it is imperative to examine the effect that laser welding has in the FZ, the PMZ and the HAZ. The properties which need to be examined are hardness, tensile strength and fatigue strength.

### ***2.7.1 Hardness***

In contrast to steel generally showing an increased hardness in the weld zone due to martensitic hardening, in the case of aluminum alloys the effect of precipitation or work

hardening is destroyed partially or totally by the heat load of the laser welding process (Dausinger, *et al.*, 1997). The amount of thermal damage is considerably lower than with arc welding, however, and decreases with increasing beam quality, allowing higher welding speed. In the case of heat-treatable alloys, the loss of precipitates in the welds and overaging in the HAZ has been identified as the main cause of hardness reduction. Solution and aging heat treatments after welding can be used to recover the hardness to the level of the base metal. However, it is undesirable to perform solution treatment at high temperatures after welding. Natural aging usually cannot achieve recovery of a hardness level within the FZ and the HAZ comparable to that of the base metal (Cao, *et al.*, 2003b).

### 2.7.2 *Tensile Strength*

Aluminum alloys usually do not display significant differences in tensile and yield strengths before and after welding, if welded in fully annealed conditions. However, they still display some decrease in strength after laser welding. Higher power and shorter wavelengths are beneficial in the production of higher strength joints of aluminum alloys. Welding speed was reported to have an important influence on the tensile properties of laser-welded joints. The tensile strength usually decreases with increasing welding speed because of less penetration depth. Results have shown that the total elongation in the longitudinal and transverse directions decreased with increasing travel speed. It was thought that the orientation of the grains has the predominant effect on the decreased ductility with increasing travel speed. For heat-treatable alloys, Nd:YAG and CO<sub>2</sub> laser welds have approximately 60% to 80% of the original metal tensile strengths and reduced elongation to failure of 1% to 3%. Depending on what alloys are welded and what type of heat treatment they have undergone before welding these percentages can vary (*ibid*).

The mechanical properties of weld joints are mainly controlled by welding defects, composition, microstructure and metallurgical states of weld metal and neighboring base metal. The presence of defects will reduce the mechanical properties of the joints. Alloy composition dominates solid solution and precipitation strengthening. Selective vaporization of volatile constituents from the laser-welded FZ degrades the mechanical properties of the weld metal. The loss of tensile strength for the precipitation-hardened alloys is caused by dissolution of the precipitate phases and the presence of weld defects such as porosity and hot cracking (ibid).

### *2.7.3 Fatigue Strength*

Fatigue properties of laser butt-welded aluminum alloys have shown to decrease to approximately 60% of the base material properties. Also, it has been observed that failure during fatigue testing occurred at the FZ interfaces. Geometrical defects usually have a strong influence on fatigue properties. The joints welded with filler material have shown a smoother transition between the workpieces, thus the sensitivity to fatigue failure was reduced. However, one cannot draw substantial conclusions about the fatigue properties of welded joints since very little data has been published on fatigue properties of laser welded aluminum alloys (ibid).

## *2.8 Fiber Laser Characteristics*

The power source used in this study is a 300 W, Single-Mode, Ytterbium Fiber Optic Laser. The power unit consists of six 50 W modules which are combined to produce an output power of 300 W. Each module contains a fiber optic bundle in which the laser

light resonates. The fiber is doped with a rare earth called ytterbium, and acts as the laser medium. Each module contains several diode lasers which serve as the pump.

The characteristic that sets the fiber laser apart from Nd:YAG lasers is the excellent beam quality, with an  $M^2$  value of approximately 1.04 which is very close to a Gaussian (normal) power distribution. This allows the beam to be focused to much smaller spots and therefore achieving higher power densities. In addition to the excellent beam quality, this laser has a wavelength of approximately 1,075 nm (near infrared spectrum), which is relatively short compared to CO<sub>2</sub> lasers. This allows for good penetration which is needed when welding highly reflective materials, like aluminum. The beam diameter exiting the collimator is approximately 7 mm, and can be focused down to about 10  $\mu$ m. At 300 W, a maximum power density of about 382 MW/cm<sup>2</sup> can be achieved.

### 3 LITERATURE REVIEW IN LASER WELDING OF ALUMINUM ALLOYS

#### 3.1 *Weld characterization results*

Since there is a wide range of research performed in laser material processing, it is important to review some of the results of the more relevant studies.

Dausinger, *et al.*, (1996) report that with a 2.2 kW Nd:YAG laser, weld depths of up to 3.7 mm in AA 6082 have been obtained at approximately 16.7 mm/s, at a power density of 3 MW/cm<sup>2</sup>. Also, Yoshikawa, *et al.* (1995), report that successful butt welds of 3 mm thick 5 and 6 series aluminum alloys can be obtained. They also used high duty cycle power modulation (pulsing) in order to prevent cracks. In a different study, a 3 kW CO<sub>2</sub> laser has been able to achieve approximately 2.5mm weld depth in aluminum alloy 7075-T6 at about 25 mm/s (Katayama and Mizutani, 2002). Also, a 4.5 kW CO<sub>2</sub> produced penetration depths of 3.5 mm in aluminum alloy series 5000 (non heat-treatable) and 6000 (heat-treatable), at a speed of approximately 33 mm/s; in comparison, a 4 kW Nd:YAG produced weld depths of 4 mm at same speed (Cao, *et al.*, 2003a). Even though the speeds at which these welds were pretty high (approximately 16 mm/s), the laser output power is still significantly high compared to the 300 W fiber laser. In addition, Ramasamy and Albright (2000) showed that when welding with a pulsed 2 kW Nd:YAG, or a 3 kW continuous wave Nd:YAG, or a 3-5 kW CO<sub>2</sub> laser, vaporization of magnesium and/or silicon can occur from aluminum alloy 6111-T4 and also the metal hardness was reduced. This means that when operating at very high power densities, loss of alloying elements is a significant problem.

Some other more recent studies are also worth being reviewed. Oi et al. (2006) used a slab CO<sub>2</sub> laser for bead-on-plate and filling wire welding of 2.4 mm thick AA 7075-T6. Mechanical properties of these welds were examined and, after heat treatment, they were able to achieve tensile strengths between 75 and 84 percent (depending on the filler metal added) of the base metal. Another study on the mechanical properties of laser welded heat-treatable aluminum was conducted by Xu et al. (2008). They used a CO<sub>2</sub> laser to weld AA 2519-T87 and examined the weld's microstructure and tensile strength. Results showed that the grains in the welds were very fine and the tensile strength, after heat treatment, reached up to 75 percent of the base metal as compared to 61 percent for MIG welding.

### **3.2 *Fiber Laser Welding***

There has been limited research done on laser welding using fiber lasers. Prof. Miyamoto was one of the first to realize the advantages of the fiber laser and propose that it be used in laser welding (Miyamoto, *et al.*, 2003). The experiments were performed on stainless steel foil with a limited output power (~50 W).

Ever since, there have been others who have recognized the value of fiber lasers in laser material processing. Allen et al. (2006) used a high power fiber laser as part of a broader study in welding of 7000 series aluminum alloy of thicknesses between 6 and 12 mm. The processing parameters of power and welding speed were not mentioned, for proprietary information purposes. Another more recent study (Brown, 2008) focused on keyhole welding on several different metals, including AA 1100, using a moderate power fiber laser (600 W). Uniform high aspect ratio welds were observed, which were in reasonable agreement with the two dimensional Rosenthal model for a moving-line heat source that was used for comparison. Also, Katayama et al. (2008) used a high power

fiber laser to investigate the various welding conditions on penetration and defect formation, on several aluminum alloys and in particular AA5083. Power densities ranged from  $40 \text{ kW/cm}^2$  to  $90 \text{ MW/cm}^2$ . At  $64 \text{ MW/cm}^2$  and  $10 \text{ m/min}$  ( $166.7 \text{ mm/s}$ )  $10 \text{ mm}$  thick plates were penetrated fully. Porosity was generated at certain processing conditions reasons for which were given by interpreting the keyhole and molten metal behaviors, observed using a high speed camera and micro-focused X-ray transmission. It was found that nitrogen gas was more effective than argon, in minimizing or even preventing porosities.

Other research using fiber lasers includes a study on micromachining using a  $100 \text{ W}$ , single mode fiber laser (Naeem and Lewis, 2006). This research group has focused their study on micro joining and micro cutting various metals using both continuous wave and pulsed modes. Similarly, Wagner (2006) studied high speed micro welding of thin sheets of various metals including aluminum, assessing the potentials for low distortion at high speeds. The processing speeds employed reached  $100 \text{ m/min}$  ( $1667 \text{ mm/s}$ ).

### ***3.3 Additional research studies***

There has been additional research in laser welding using both  $\text{CO}_2$  and Nd:YAG lasers for various alloys, both heat-treatable and non-heat treatable, investigating various weld properties, such as penetration and aspect ratio, weld quality and microstructure and mechanical strength for various different joint configurations. This research has been summarized in professor Duley's book "Laser Welding" (Duley, 1999) and is listed in Table 3.1.

Table 3.1: Experimental Studies of Laser Welding of Aluminum Alloys

Material	Laser	Power Level (kW)	Measured Parameter	Reference
Al 5456	CO <sub>2</sub>	8	Mechanical properties, elemental analysis	Moon and Metzbower (1983)
Aluminum alloys, 5000, 6000 series	CO <sub>2</sub>	3	Weld profile, hardness, penetration depth, effect of shield gas	Behler et al. (1988)
Al 8090	CO <sub>2</sub>	2	Weld width, penetration depth, focal position, lap welds	Kamalu, McDarmaid and Steen (1991)
Al 2090	CO <sub>2</sub>	1.3	Penetration depth, effect of surface penetration	Molian and Srivatsan (1991)
Various alloys	CO <sub>2</sub>	5	Effect of assist gas, focal position on weld profile	Matsumura et al.
Al 5000, 6000 series	CO <sub>2</sub>	5-10	Tensile strength, elongation, porosity, filler	Jones et al. (1992)
Al 2000, 6000, 7000 series	CO <sub>2</sub>	To 2.5	Effect of filler, gas flow, lap welds	Bonello and Bailo (1993)
Al 5000, 6000 series	CO <sub>2</sub>	To 5.0	Porosity, tensile strength	Rapp et al. (1993)
Al 2219 to Al 6061	CO <sub>2</sub>	To 3.7, pulsed 5 kHz	Microstructure, hardness	Gopinathan et al. (1993a)
Al 5000, 6000 series	Nd:YAG	0.4, 0.6 Pulsed	Microprobe studies, penetration depth, cracking	Cieslak and Fuerschbach (1988)
Al 1050	Nd:YAG		Effect of pulse length, focusing on bead shape and penetration, lap welds	Watanabe and Yoshida (1990)
Al 5052, 5152	Nd:YAG, pulsed and CW	0.7	Penetration depth, bead width, cracking	Aruga et al. (1992)
Al 5052, 5083	Nd:YAG	4.2	Penetration depth, porosity	Nishimi et al. (1996)
Al 5052, 5083	Nd:YAG	0.9-1.6	Effect of focus, surface preparation	Xijing, Katayama and Matsunawa (1997)
Al 5754-0, 6111-T4	CO <sub>2</sub>	3	Elongation, microstructure	Venkat et al. (1997)

#### 4 SPECIFIC RESEARCH OBJECTIVES

This research focuses on the following objectives:

A) The first objective is to provide a thorough process characterization of low speed laser welding of AA 7075-T6 and to understand the factors causing weld defects at very slow welding speeds.

B) The second research objective is to test the following hypothesis: The low aspect ratio, low efficiency, and large porosities observed in the weld by slow speed welding are due to overheating of the molten pool. At slow speeds, a large molten pool is created. As a result, the CW laser beam mainly irradiates at the molten pool, which absorbs a large portion of the beam energy near the surface, and subsequently transfers the energy into the bulk material via more effective convection and conduction. Consequently, the welding process becomes inefficient and the welds become shallow and wide. As the speed slows further, the excessive energy absorbed by the molten pool can also lead to boiling, resulting in large porosities. Therefore, by utilizing a pulsing scheme to turn off the laser beam until it moves to a solid front, we should be able to create welds with higher efficiency, improved aspect ratio, and no large porosities.

C) The third research objective is to apply a cooling delay technique to reduce the steep temperature gradients induced in pulsed welding. The high cooling rate of a molten pool during laser welding leads to transverse and longitudinal solidification cracks; by heating the molten pool properly to slow down the cooling rate, the solidification cracks can be avoided.

D) The fourth research objective is to repair fatigue cracks via laser welding.

## 5 RESEARCH APPROACHES

With respect to the above research objectives, the following research approaches are proposed:

For research objective (A):

- Adapt a previously developed model (Lankalapalli, et al., 1996) that predicts weld penetration with respect to Péclet number (proportional to processing speed) for stainless steel, to predict the upper bound weld penetration in AA 7075-T6 for much lower speeds.
- Create a series of bead-on-plate welds at different processing speeds (10, 4, 2 and 1 mm/s) for a variety of focal positions, and compare the best results with the model prediction.
- Investigate the effects of various focus positions on weld penetration.
- Characterize results in such a way that will take all of the major processing parameters (power, speed, focusing) into account at the same time.
- Use online measurement methods such as high speed photography, vapor intensity measurements and spectroscopy to draw conclusions of the differences between the different process parameters.

For research objective (B):

- Create bead-on-plate welds by pulsing the laser at 1 mm/s processing speed for a range of pulse durations from 0.5 – 1000 ms and duty cycles adjusted in such a way to maintain a certain overlap percentage (80 % is an industry standard) and determine the best pulsing parameters based on weld quality (absence of blowholes and porosities), geometry (conical keyhole with high aspect ratio) and high efficiency.
- Compare pulsed welds cross-sections with CW and characterize the differences in weld efficiency, amount and type of defects and aspect ratio.

For research Objective (C):

- Create pulsed bead-on-plate welds through pulsed laser welding by modulating the power of the laser from 100% power to a lower power, ranging from 12.5 – 90 %, with the intension of reducing the cooling rate of the melt pool. Determine the best low power pulsing condition based on weld quality (absence of solidification cracks and good aspect ratio) and penetration.
- Create pulsed welds under the best condition found from the above tests and compare with pulsing 100 % high and 0 % low power. Compare the weld quality and penetration.

For research Objective (D):

- Create full penetration bead-on-plate welds on thin plates (approximately 800  $\mu\text{m}$  thick) according to best welding conditions determined during the partial penetration process characterization.
- Adjust process parameters in order to optimize the full penetration welding result.
- Apply best process parameters for full penetration welding of thin plates to the repair of cracked thin plates via laser welding.
- Perform tensile tests to determine and compare the ultimate tensile strength of the repaired cracks, the full penetration bead-on-plate welds and the reference base material (AA 7075-T6).

## 6 EXPERIMENTAL APPARATUS

A 300 W Ytterbium, Single-Mode, Fiber Laser (Figure 6.1) is used for this research. A NEMA two-phase 220V outlet provides electric power to the laser. Its near infrared (1,075 nm) beam is fiber deliverable and comes out of the collimator as a cylindrical 5 mm beam.



**Figure 6.1: 300 W Ytterbium, single-mode fiber laser power unit**

The laser beam quality is near Gaussian ( $M^2 \sim 1.04$ ). An optical isolator (shown in Figure 6.2) was attached to the collimator and is used to divert any reflected light away from the collimator in order to avoid damage to the fiber due the high reflectivity of

aluminum. The beam diameter and beam quality were modified slightly (beam diameter  $\sim 7$  mm,  $M^2 \sim 1.15$ ).

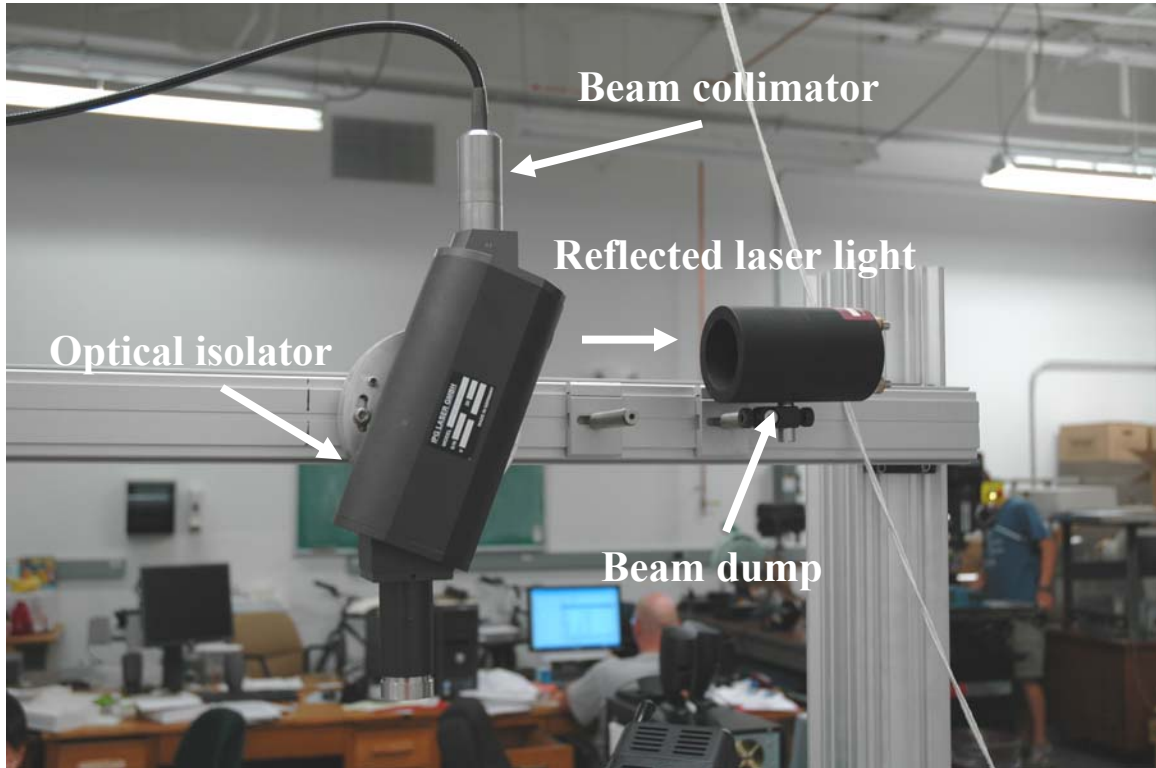
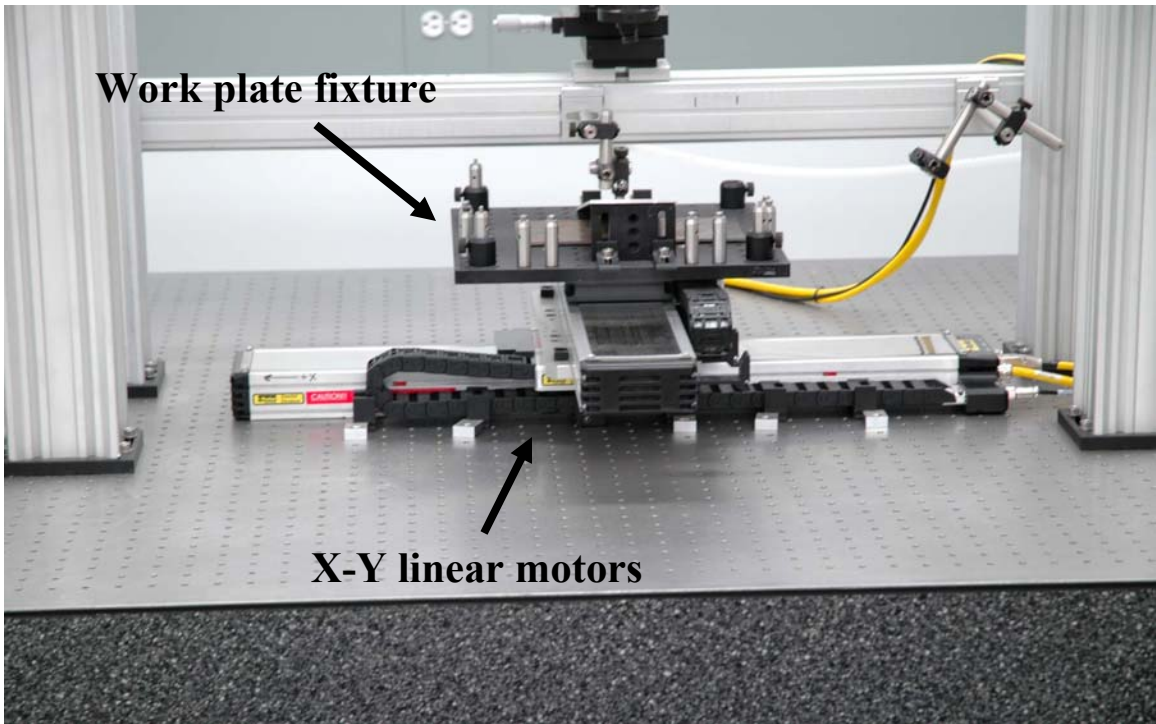


**Figure 6.2: Optical isolator connection to collimator, used to divert away reflected laser light into a beam dump**

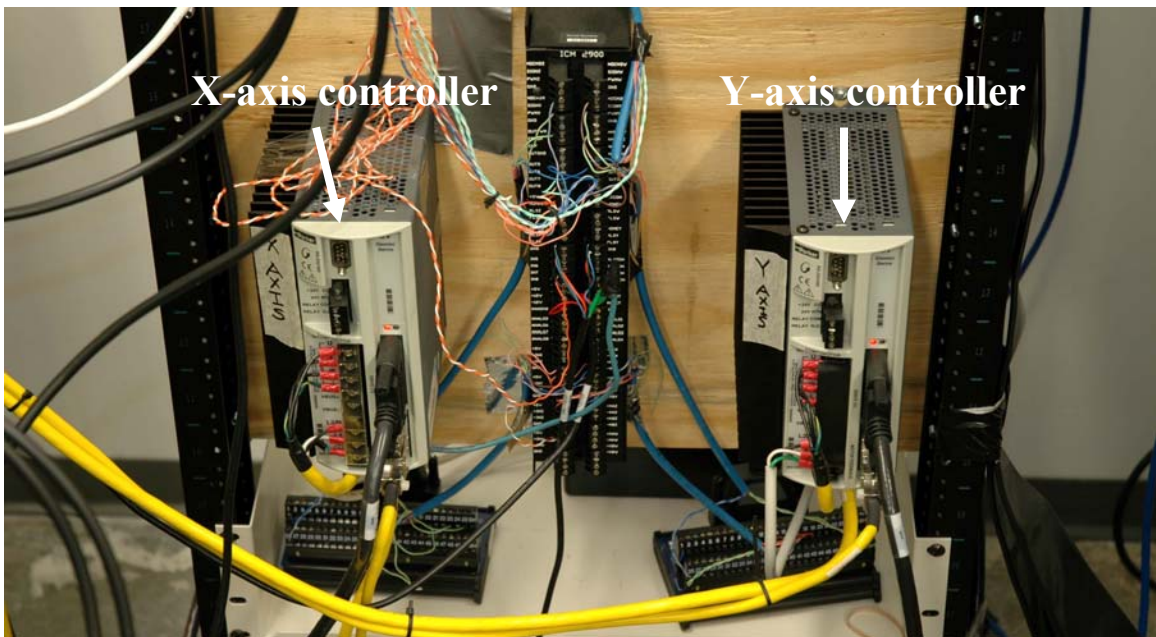
The Parker Automation X-Y linear motors (Figure 6.3) are used to move the workpieces and are controlled by the Galil X-Y axes motion controllers (Figure 6.4). The motors have a resolution of  $.5 \mu\text{m}$  and a range of 1 m. The maximum acceleration and deceleration is  $\pm 2$  g's and maximum speed is 1.5 m/s.



**Work plate fixture**

**X-Y linear motors**

**Figure 6.3: XY Linear motors with attached work plate fixture**



**X-axis controller**

**Y-axis controller**

**Figure 6.4: Galil X-Y axes motion controllers**

The data acquisition system used is dSPACE 4.0 (Figure 6.5). It is mainly used as an external control for the laser and for acquiring data from sensors (photodiode). This helps automate the operation of the laser. Simulink is used to create different operation schemes and can be synchronized with the movement of the linear motors.

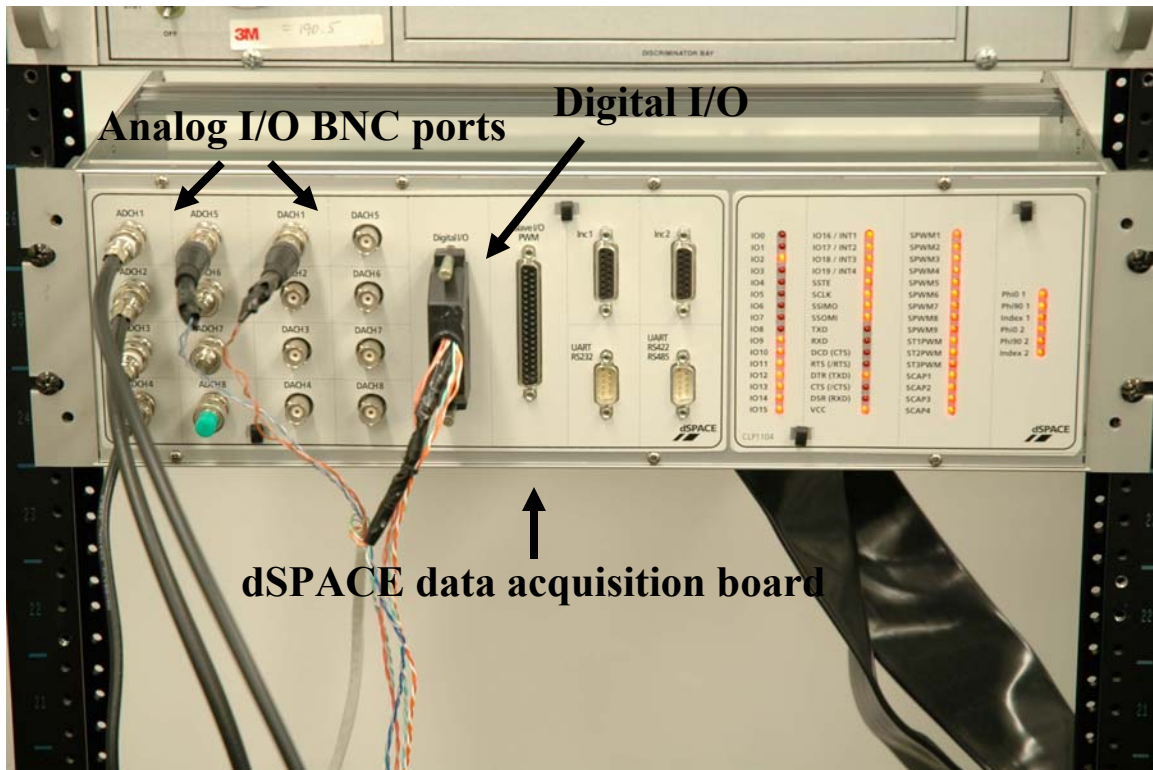
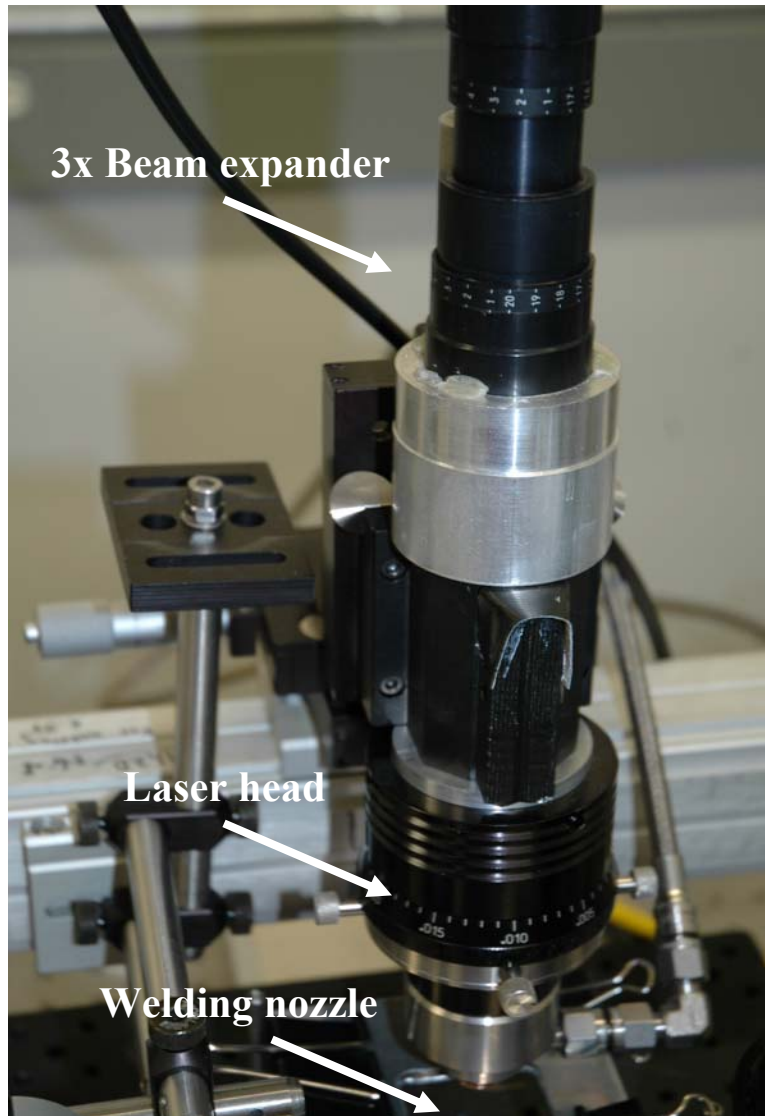


Figure 6.5: dSPACE 4.0 data acquisition system

A 3x beam expander is used in combination with the 100.1 mm OptoSigma triplet lens to obtain a minimum focus spot size of 12.01  $\mu\text{m}$ . Equation 6.1 shows how to calculate the minimum spot size.

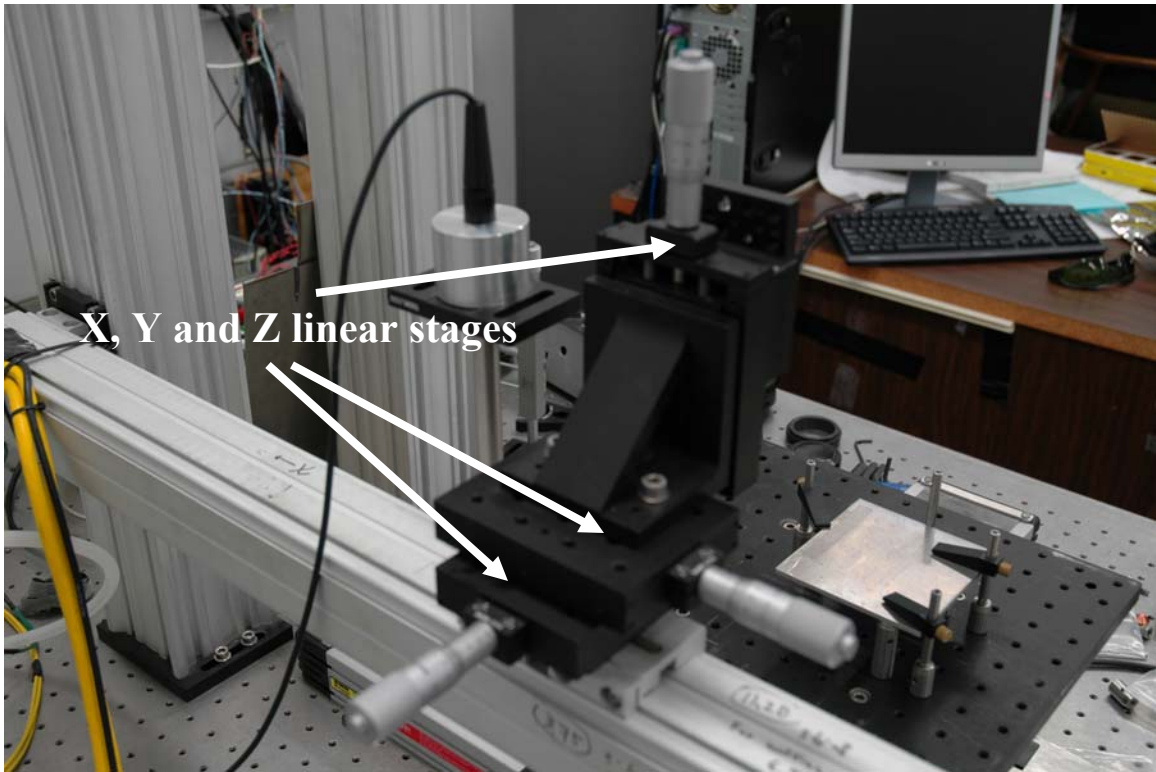
$$\begin{aligned} \text{Spot size} &= \frac{\text{Lens Focal Length}}{\text{Collimator Optics Focal Length} * \text{Beam Expansion Factor}} * \text{Fiber Diameter} \\ &= \frac{100.1 \text{ mm}}{25 \text{ mm} * 3} * 9 \mu\text{m} = 12.01 \mu\text{m} \end{aligned} \quad (6.1)$$

Figure 6.6 shows the optical setup. The laser beam is centered with respect to the beam expander and the laser head. The laser head contains the focusing triplet and can be adjusted using the outer ring. At the bottom of the cutting head there is a chamber that allows for shielding to flow out through the welding nozzle. This chamber is sealed by a special cover glass and a rubber gasket.



**Figure 6.6: Beam expander and laser head setup**

X, Y, Z Linear Micrometer Stages (Figure 6.7) are used to align the optics with the beam. Also, the Z stage is used to change the focusing of the beam, as well as the nozzle height with respect to the workpiece surface. The resolution of the micrometer stages is  $10\ \mu\text{m}$  and their range is approximately 26 mm.



**Figure 6.7: X,Y, Z micrometer linear stages**

For data acquisition, a Tektronix 3012B oscilloscope was used, shown in Figure 6.8. It has two input channels and the sampling rate capabilities go up to 100 MHz. It always acquires 10,000 samples and the sampling rate is determined by the time range that is chosen.

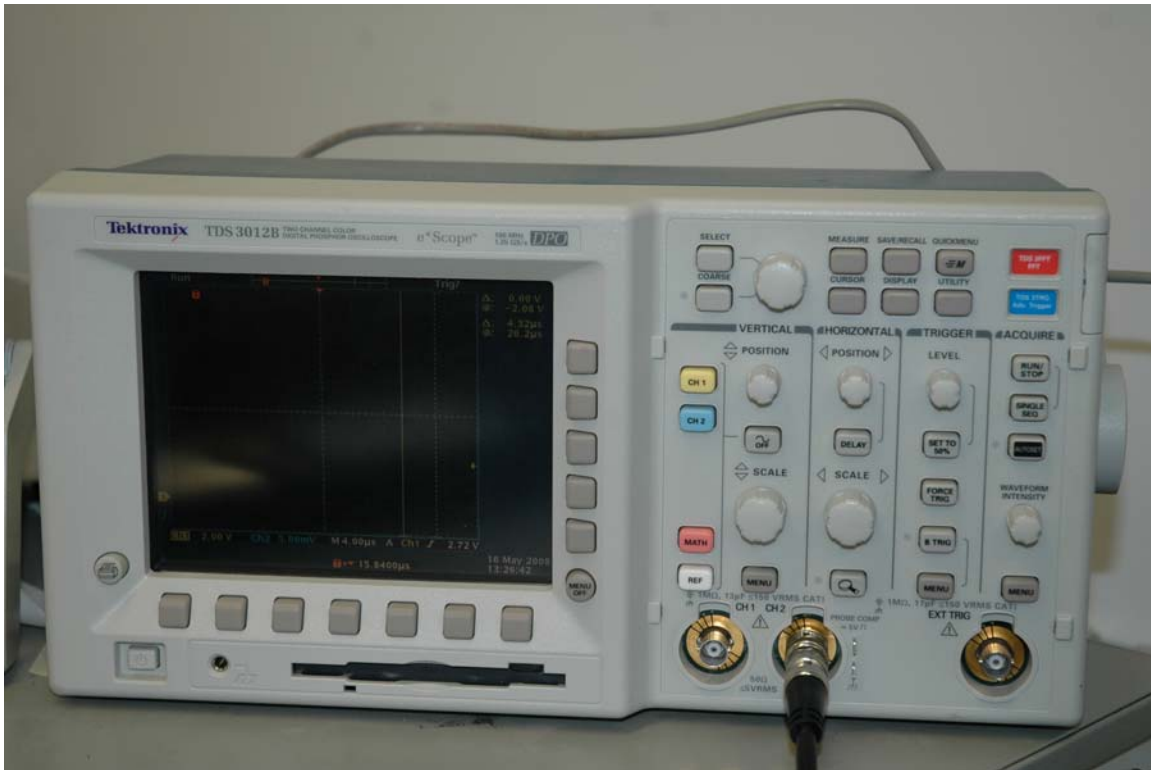


**Figure 6.8: Tektronix 3012B oscilloscope**

The Zeiss (Figure 6.9) inverted microscope was used to enlarge all the weld cross-sections and obtain pictures. There are a number of different magnifications that can be obtained. The current objectives are 2.5x, 8x, 16x, 40x and 80x. There is also an additional 2x magnification factor that can be multiplied to these aforementioned objective magnifications. Also, the eyepieces provide the user with a 10x magnification. Therefore, the maximum magnification that can be obtained is 1600x.



**Figure 6.9: Zeiss Inverted Microscope**

A Saphir 520 Grinder/Polisher (Figure 6.10) was used to polish the aluminum welds to a mirror finish. The grinding/polishing wheel can reach up to 600 rpm and 100 N of force can be applied to the samples. The grinding polishing head also spins at a constant 60 rpm and can be adjusted to spin clockwise or counter-clockwise.



**Figure 6.10: Saphir 520 Grinder / Polisher**

The vapor/plasma spectrums were obtained using an Ocean Optics HR4000 spectrometer (Figure 6.11), with groove density of  $2400 \text{ mm}^{-1}$  and resolution of approximately 0.05 nm. The wavelength range for the particular spectrometer is 349 – 443 nm.

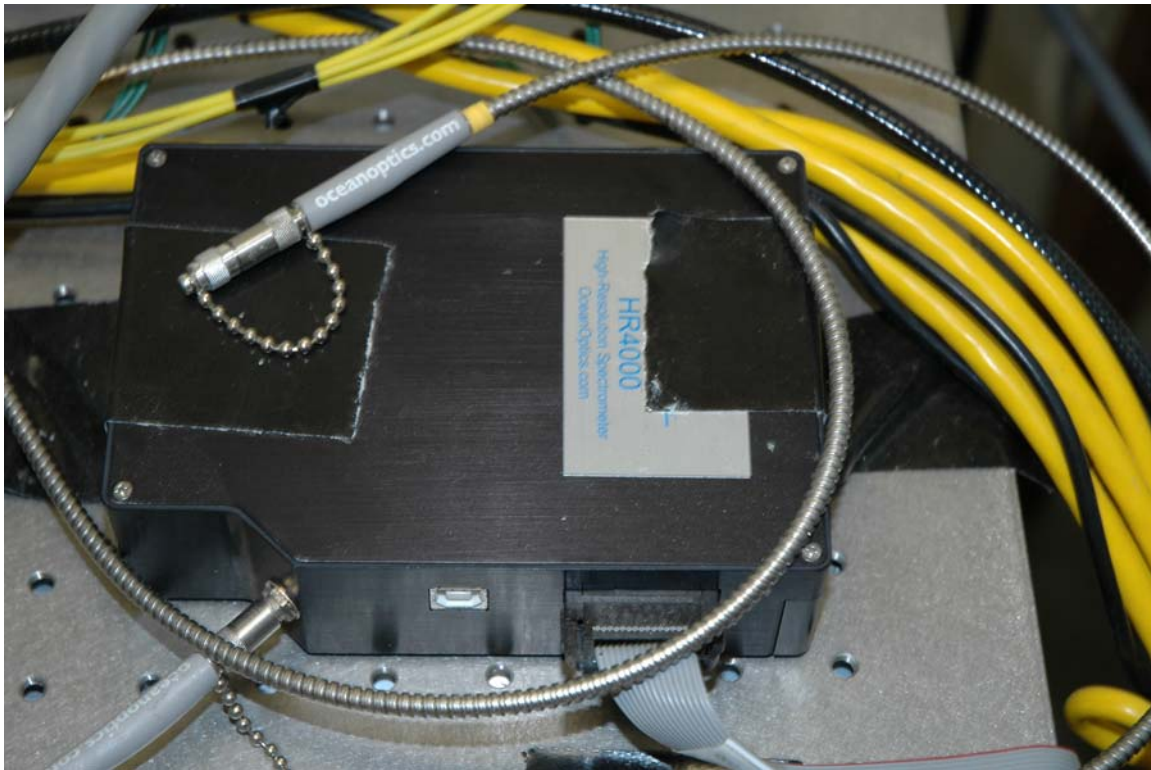


**Figure 6.11: Ocean Optics HR4000 spectrometer**

The vapor/plasma intensity measurements were obtained using a Hamamatsu silicon S1336-18BQ photodiode (Figure 6.12). This photodiode is most sensitive (80-90% transmission) in the visible spectrum. However, it also has moderate sensitivity (50-60% transmission) in the near-infrared region which includes the wavelength of the laser (1,075 nm). In order to separate this signal during photodiode experiments a colored glass bandpass filter was used that can filter out the reflected laser radiation. During reflectivity measurements, the filter was removed and both the visible and near-infrared spectrums were measured. Since the reflectivity measurements were much stronger than the vapor/plasma measurements, it was important to make sure that the signal was not being saturated and that the measurements were taken in the linear range of the photodiode. The saturating point is approximately 5.76 volts and all the measurements were well below that voltage.

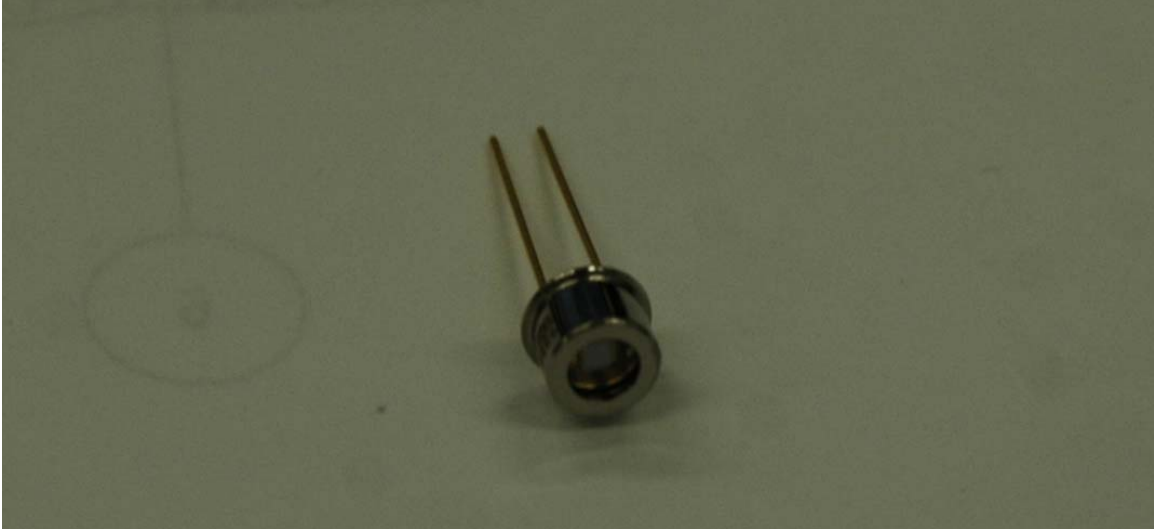


**Figure 6.12: Hamamatsu Si S1336-18BQ photodiode**

## 7 EXPERIMENTAL PROCEDURES

The experimental procedures are described in the subsequent subsections. The first step was to determine the laser beam's focusing position, using a very simple but effective focusing technique based on experimental observations from laser spot welding and drilling. The procedure used to create CW and pulsed welds for a variety of processing conditions is described next, along with the experimental setup. Several online measurements were required. The setup with respect to the welding experiments is described for the high speed camera, photodiode and spectroscopic measurements. Subsequently, the specific details of the pulsed welding experiments are discussed and finally, the experimental procedure for the full penetration welding and crack repair and the tensile testing procedure are discussed in the final subsections.

### *7.1 Determination of the Laser Beam's Focusing Position*

The determination of the laser beam's focusing position was done by using a laser drilling technique. One of the fiber laser's particular characteristics is that when a laser pulse is released, there is an approximately 1,500 W power spike that is output for about 1  $\mu$ s before it drops to the steady-state power value of 300 W. By pulsing the laser for a very short time, approximately 3  $\mu$ s, we can take advantage of this power spike and create a very high power density at the focus plane. This enables us to perform laser ablation (drilling). The focusing technique utilizes this process, by creating spot welds or holes at different z-positions, every 10  $\mu$ m. A picture is taken of each of these groups of welds/holes and using special calibrated software, the radii are measured and plotted versus the z-focus position (Figure 7.1).

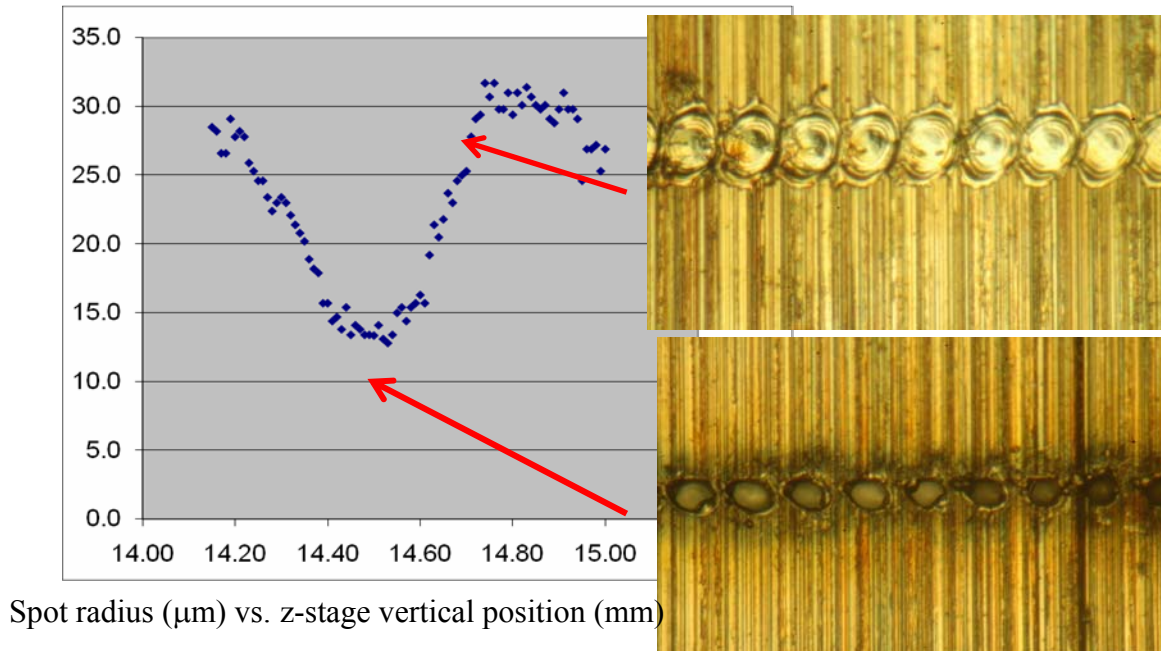


**Figure 7.1: Spot welds or holes at different focusing locations**

Since the power densities are so different at different focusing positions, the pulsing will either create very small holes, approximately on the order of the focused beam spot size, or it will create larger spot welds. When all the radii are plotted, the minimum of the resulting curve shows the approximate location of the focusing plane. This is a relatively quick and effective way to find the location of the focus.

## **7.2 *Bead-on-Plate CW and Pulsed Laser Welding***

The procedures for performing CW and pulsed welding are very similar. A thick aluminum (AA 7075-T6) square plate of appropriate thickness (usually 0.125 in.) is placed on top of three posts which are firmly attached to the linear motor's threaded plate, which is then placed under the laser optics (Figure 7.2). Typically with thicker pieces, the accuracy of this method was sufficient since the experiments were quite repeatable.

However, since full penetration, thin sheet welding proved to be extremely sensitive to focusing changes, a higher precision method was employed. The workpiece was sandwiched between two other square plates, each with a 40 mm square slot in the center, clamped with three binder clips and then placed on the posts. Using a dial gage and a height gage, the plates can be checked for flatness and relative (to a certain position of the height gage, 1.854 in) height repeatability.

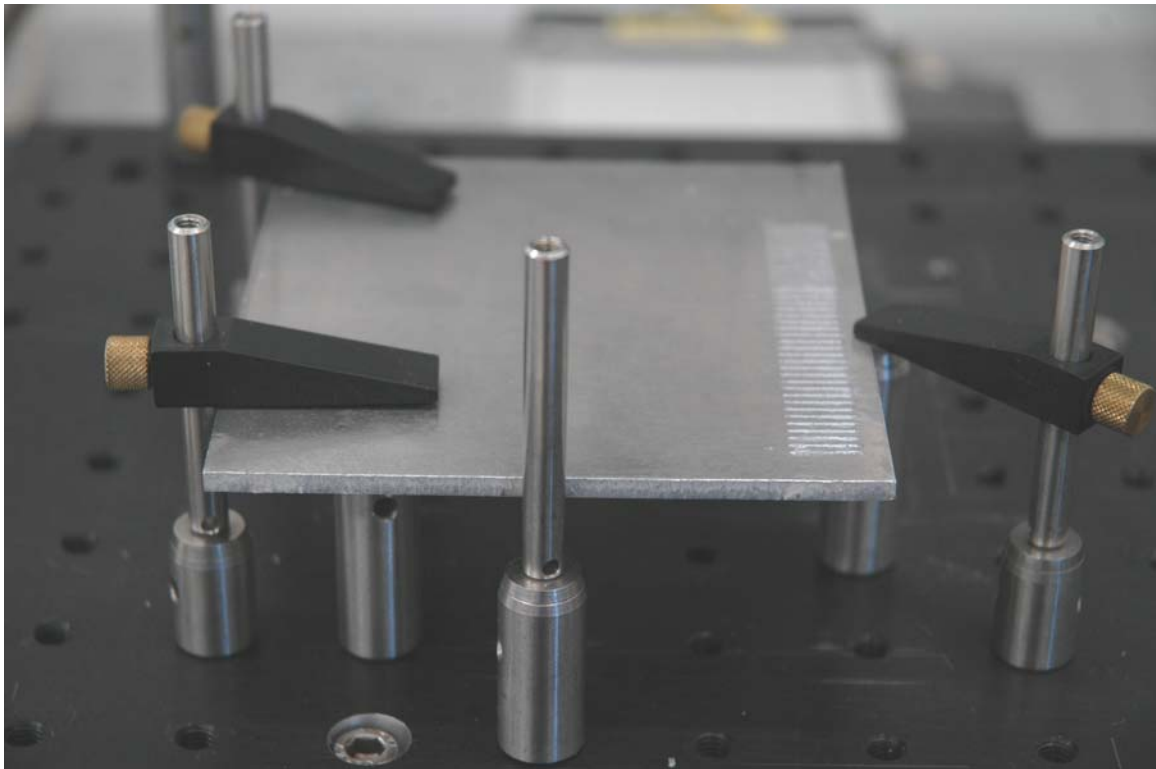


**Figure 7.2: Initial bead-on-plate Welding Aluminum Plate Setup**

Using a visible (red) guide laser, the spot is placed at the desired location and the focus is adjusted accordingly (usually the beam is focused into the workpiece) using the micrometer to adjust the height of the nozzle from the workpiece and the cutting head's focusing ring to adjust the internal lens triplet. A Motion Control program is then used to translate the workpiece at the desired speed, for a specified distance (usually 30 mm).

At the same time synchronization signals are sent to the dSPACE/Simulink program, which in turn sends the control signals to the laser. Before the program sends the linear motors into motion, it turns the laser on for 5 seconds, to ensure the output power stabilizes. Also, before the program is executed, the shielding gas is set to the appropriate pressure (3 psi). When the particular weld is done, the linear motor moves back to the same location and moves over approximately 1.5 – 2 mm and is ready for the next weld.

### ***7.3 High Speed Camera Experiments***

The high speed camera was set up as shown in Figure 7.3.

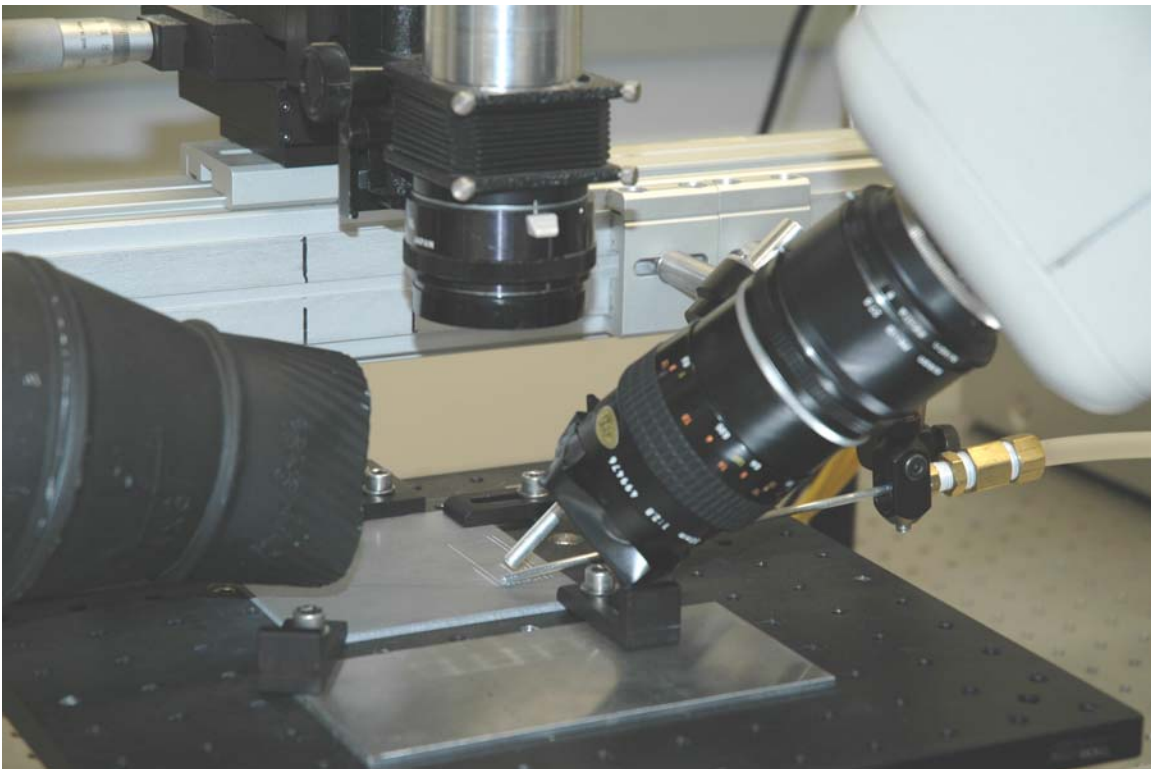


**Figure 7.3: High Speed Camera Experimental Setup**

Bead-on-plate weld experiments were done with the high speed camera recording from approximately a  $60^\circ$  angle. The camera lens was protected by a near-infrared filter from any reflected laser radiation. The frame rate at which the camera recorded the vapor/plasma plume pictures was 4500 frames per second (fps) and recorded for a couple seconds (until the buffer was full). The camera was started by an external trigger that was sent out from the Simulink program synchronized with the beginning of the laser output. The welding speeds at which the high speed camera experiments were done were 1 mm/s, 2 mm/s, 4 mm/s and 10 mm/s.

#### ***7.4 Photodiode Relative Intensity Measurements***

A silicon photodiode was used to record the intensity of the vapor/plasma plume, as well as of the laser beam reflectivity and is shown in Figure 7.4.



**Figure 7.4: Photodiode Experimental Setup**

The photodiode was set up at an approximately  $45^\circ$  angle, placed in the focusing plane of a camera which was used to focus the light into the photodiode. The sampling rate at which the data was acquired was 25 kHz for the vapor/plasma experiments and 1 kHz for the reflectivity experiments. The welding speeds at which photodiode data was acquired and analyzed were 10, 4, 2, 1 and 0.5 mm/s as well as during pulsed welding with 200 ms period and a 50 percent duty cycle, while moving at 1 mm/s. The reflectivity experiments were done at 10, 4, 2 and 1 mm/s respectively, as well as for an experiment which starts at 1 mm/s and speeds up to 10 mm/s mid-process. For the reflectivity measurements the filter was removed and the combined vapor/plasma and reflectivity signals were measured. The combination did not cause a problem because the reflected laser beam signal proved to be much stronger than the vapor/plasma signal (over 10 times).

## ***7.5 Spectroscopic Characterization of Vapor/Plasma Plume***

Experiments were conducted at three different processing conditions: 1  $\mu$ s pulses at 100 % power ( $\sim 1,500$  W), 1  $\mu$ s pulses at 70 % power ( $\sim 1,050$  W) and CW welding at 1 mm/s and 100 % power ( $\sim 300$  W). For the pulsing conditions, five hundred 1  $\mu$ s pulses are shot and the spectrometer acquires and integrates the data in 100 ms increments, which are averaged over 5 scans. In order to ensure that each pulse will irradiate a “smooth” surface each time the target surface (SUS 316) is translated at an appropriate speed. For the welding condition, a weld is made and the spectrometer acquires and integrates the data in 200 ms increments, which are averaged over 40 scans. In addition to contributing to repeatability, averaging over several scans helps increase the signal-to-noise ratio. It was found that the welds have a much lower vapor/plasma signal and so it was necessary to average over more scans than what the pulsing conditions required.

The experiments were conducted in the absence of shielding and control gases, in order to obtain the maximum possible absorption coefficient (worst case scenario). For this reason, the angle at which the signal was acquired was at an almost vertical position ( $\sim 60^\circ$ ), so as to get contributions from both the keyhole and the plume above it. Figure 7.5 shows the experimental setup.

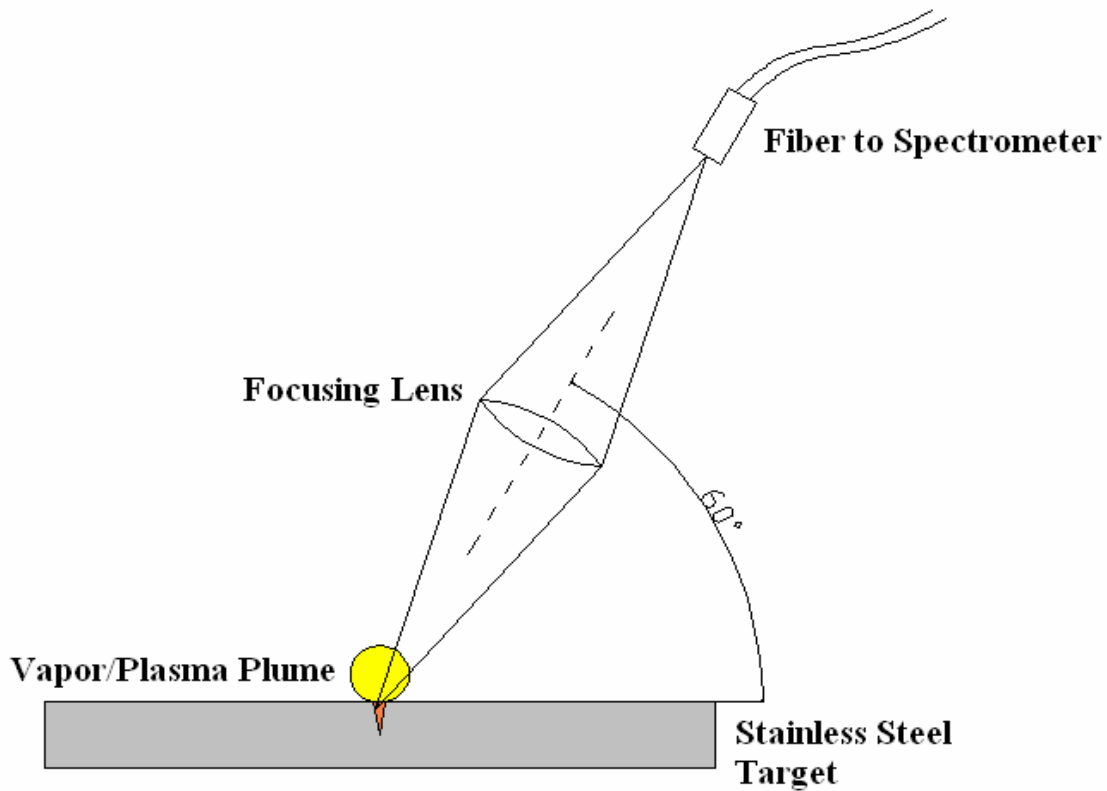


**Figure 7.5: Spectroscopic experimental setup**

The light signal was delivered to the spectrometer using an Ocean Optics XSR fiber with diameter 200  $\mu\text{m}$  and transmission of approximately 65 % in the spectrometer's bandwidth (349 nm – 443 nm). The light was focused into the fiber using a Leica camera with a 50 mm focal length Focotar lens.

## ***7.6 Pulsed Laser Welding***

Bead-on-plate pulsed welding experiments were done with various pulse durations and duty cycles (the time the laser is on divided by the total period) to maintain an 80 weld overlap percentage. The pulse durations that were selected were 0.5, 1, 10, 100, 500 and

1000 ms. In order to determine the duty cycle required to maintain an 80 percent overlap percentage, the approximate weld width of each pulsing condition was required. An experiment was done at a speed of 1 mm/s (the pulsed welding speed condition) with an extremely low duty cycle, allowing spot welds to occur 1 mm or so from each other. These spot welds were measured, and their average width was measured and recorded. Using these widths the following equations (8.1 and 8.2) were used to calculate the corresponding duty cycles.

$$\text{Duty Cycle} = \frac{\text{Pulse duration}}{\text{Pulse duration} + \text{Off time}} \quad (8.1)$$

$$\text{Off time} = (1 - \text{Overlap \%}) \cdot \frac{w}{v} \quad (8.2)$$

where  $w$  is the spot weld width and  $v$  is the weld processing speed.

Finally, the pulsed welding experiments with a low non-zero power were performed in the same way for the condition of a 10 ms pulse duration at the appropriate duty cycle (calculated as stated above), and using low powers of 12.5, 15, 20, 25, 30, 35, 40, 45, 50, 60, 70, 80 and 90 percent. Figure 7.6 shows an example of what the pulse shape looks like.

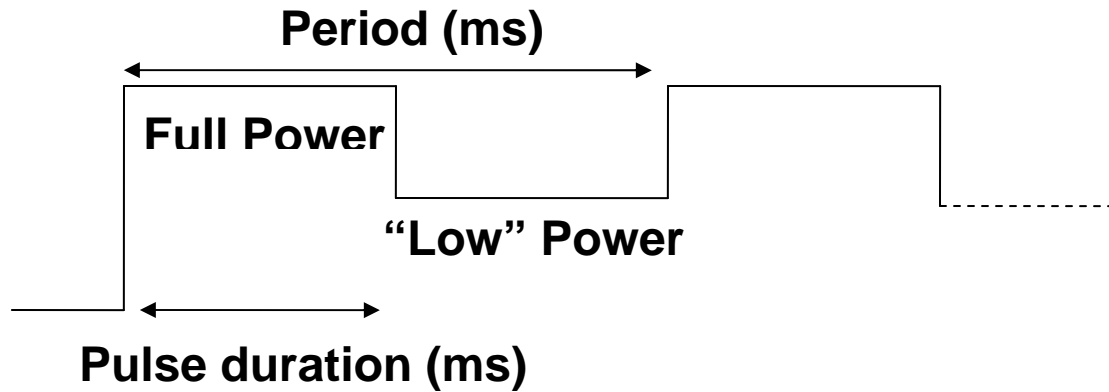


Figure 7.6: Laser pulse shape diagram for non-zero, “low” power pulsing

### 7.7 *Thin Plate Precision Laser Welding*

The thin plate laser welds were conducted in a similar fashion as the bead-on-plate welds. Making sure the plate was flat was very important because thin plate full penetration welding is much more sensitive to focusing changes. Extra care was taken to check the height and flatness after each weld, due to high distortion, and the focus was adjusted accordingly.

### 7.8 *Tensile Testing*

The tensile testing was conducted on coupons shaped in accordance with the ASTM E8 standard for tension test samples. The tensile test was performed on 0.8 mm thick coupons with a 6 mm gage width. First, tensile tests were done on base material in order to establish a control for comparison with the welded samples. Then, tensile tests were done on bead-on-plate full penetration welds for single and double passes, to compare the best weld case scenarios with the base material results and once the cracked samples were

repaired, tensile tests were performed on those as well to evaluate the success of the repair.

The sample was mounted on the top grip first making sure it was aligned with the tensile testing direction and that it was not gripped in the gage (thinner, 6mm) section. Then the lower grip was moved into place and then tightened at the lower part of the specimen. Once this had been done the tester was “zeroed” to remove any residual load caused by the gripping. The testing was ready to be performed. The max load was selected so as to make sure the sample would break (800 lbf). The load rate was selected to be 20 lbf/s, and the profile was selected as a ramp. Once the sample broke, the maximum load was recorded from the tensile tester’s display.

## 8 RESULTS AND DISCUSSION

### *8.1 Process Characterization of High Brightness, Low Speed, Partial Penetration Laser Welding of AA 7075-T6*

This main focus of this research is on studying and understanding low speed laser welding of aluminum alloys using a high brightness, 300 W fiber laser. As mentioned in the introduction, research on low speed welding might be necessary when non-straight seams are in need of welding because large accelerations and decelerations (required to maintain a high speed) could affect the consistency of the weld. This low speed welding process has been studied under various conditions and will be characterized in the following sections.

The most important observation that has been made is that there is a speed, below which the laser welding process breaks down, resulting in decrease in penetration (contrary to model predictions), reduction of aspect ratio and a significant increase in defects (such as blowholes) throughout the welds. Usually, at high irradiances, laser welding processes break down with CO<sub>2</sub> laser welding, due to the growth and high absorptivity of a vapor/plasma plume above the keyhole. However, with the fiber laser, the resulting vapor/plasma plume appears to be optically thin due to its shorter wavelength. This was confirmed via spectroscopic techniques that can approximate the electron temperature and density of the vapor/plasma, which are then used to calculate the absorption coefficient of the vapor/plasma. As experimental evidence suggests, if strongly absorbing plasma was not the cause of the process breakdown, then an explanation of this new process is required, with a proposed solution to create welds that could be applied to crack repair.

The next few sections will characterize the laser welding process of aluminum at low speeds by showing certain trends in penetration and process efficiency, until a certain point when the speed becomes too slow and the trends no longer apply. This means that the specific process has broken down due to the effect of unknown factors. The following experimental analysis will provide reasonable explanations of what these factors are.

Section 8.1 describes how input power is distributed into different components during laser welding and discusses which ones are considered potential power loss components and which contribute positively to the creation of a weld. Section 8.2 describes an effective heat conduction model that can be used to predict the upper bound penetration of the weld based on the amount of power absorbed and conducted through the keyhole walls. This model is validated using experimental data from high speed welding of stainless steel. It is then modified in order to be used to predict the upper bound penetration in AA 7075-T6 at low speeds. The data obtained shows good correlation down to a certain low speed threshold. Section 8.3 examines the effect of focusing on weld penetration. Section 8.4 then defines a metric for total irradiated energy density per weld length that takes into account the major process parameters (power, speed, focusing and beam profile) at the same time. In the same section another metric is defined that is used to characterize the weld efficiency; that is, how much of the total input energy is used to create the weld and how “well” it is used (high aspect ratio vs. low aspect ratio). The weld data is then characterized using these metrics and several conclusions can be made based on how efficiently they have coupled the input energy relative to different focusing positions and processing speeds. Section 8.5 investigates possible factors that could be responsible for the poor welding efficiency observed at the lower speeds. Section 8.6 discusses several online measurement techniques that could give better insight of what changes in the process as processing speed is decreased. In sections 8.7

and 8.8 the results of the testing of the second and third hypotheses are presented, giving further insight of what might be happening with low speed welding. Section 8.9 is where the best process parameters have been applied to thin sheet, full penetration laser welding, for application to crack repair. Limited mechanical testing was done to provide a preliminary evaluation of crack repair success.

## 8.2 Laser Power Distribution

In order to understand the laser welding process, it is important to know how the total input power from the laser is distributed. It can be broken down into several components, as shown in the following equation:

$$P_{in} = P_{weld} + P_{cond} + P_{evap} + P_{ref} + (1 - \alpha) \cdot P_{vap/plasma} + P_{scat} \quad (8.1)$$

where  $P_{in}$   $\equiv$  Input power from laser ,

$P_{weld}$   $\equiv$  Power absorbed by the weld ,

$P_{cond}$   $\equiv$  Power conducted away ,

$P_{evap}$   $\equiv$  Power absorbed by ejected vaporized metal ,

$P_{ref}$   $\equiv$  Power reflected ,

$P_{vap/plasma}$   $\equiv$  Power absorbed by vapor/plasma plume ,

$P_{scat}$   $\equiv$  Powerscatteredby particlesin vapor/plasma plume,

and  $\alpha$   $\equiv$  fraction of vapor/plasma redeposited in weld .

Except for the power used to create the weld, the rest of the power components represent losses. These losses can be negligible or can increase depending on the process

parameters. For example, even though the laser beam has been shown to be scattered and defocused by the fine vapor particles (Rayleigh scattering) in high power CO<sub>2</sub> welding (Tu et al., 2002), it is extremely unlikely that it has a similar effect in this research, due to the fact that the scattered power will be reduced by 10<sup>4</sup> due to the fiber laser's wavelength being 10 times shorter than the CO<sub>2</sub> laser wavelength. In any case, the objective is to increase the power coupling into the  $P_{weld}$  component in the most efficient way (high depth/width aspect ratio). The  $P_{weld}$  and  $P_{cond}$  can be accounted for by using a 2D quasi steady state heat conduction model (described in the following section) reasonably well. If the welding process deviates significantly from the model prediction, this means that the power coupling has changed and one of the remaining loss components has increased. By knowing the possible power loss components, post processing and online data analysis can be used to determine the cause of this change in the process.

### **8.3 Idealized Welding Model**

Before proceeding with experimentation, it is of interest to be able to predict the behavior of the welding process theoretically; penetration is one of the most important issues concerning this type of research. Since the maximum thickness of the part to be welded depends on the depth of the weld, it is imperative to predict the maximum penetration possible at the available power range. This can be done through the use of the theoretical, 2-D heat conduction model (Lankalapalli, Tu, *et al.*, 1996) discussed previously. This model makes several assumptions which significantly reduce its complexity. The general idea of the model is to calculate the heat conduction over an infinitesimally thin layer of thickness (depth)  $dz$  at a specific distance from the top of the surface (Figure 8.1).

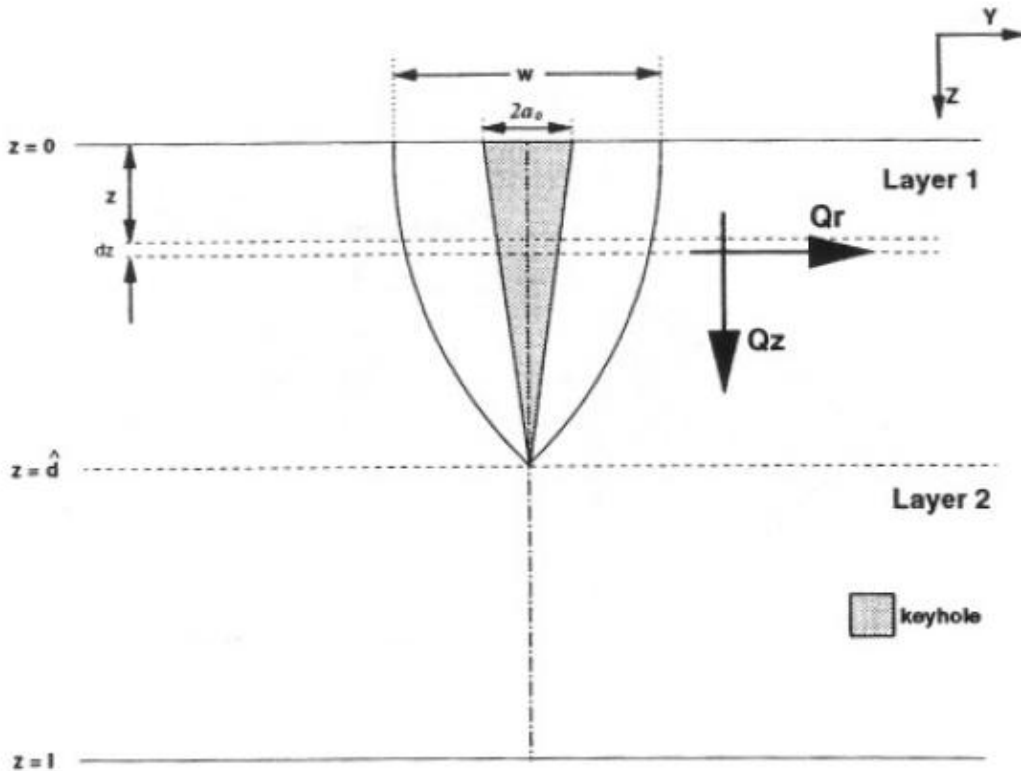


Figure 8.1: Keyhole Profile (Lankalapalli, Tu, *et al.*, 1996)

One of the assumptions made, is that the walls of the keyhole within this layer are perpendicular to the surface and that heat conducted in the  $z$ -direction is much less than the heat conducted in the radial direction. Therefore, a conical keyhole can be divided into an infinite number of such infinitesimally thin layers and the depth can be approximated by cylindrical heat sources of varying radii, moving together at a constant speed in each of these thin layers. Another assumption made is that there is a quasi-steady state environment in which a cylindrical surface of radius  $a$ , at uniform temperature  $T_V$ , is moving with a constant speed,  $v$ , along the  $x$  direction, in an infinite medium initially at constant temperature,  $T_0$ . Finally, assuming that the thermal properties of the medium are constant and that the axis of the cylindrical surface passes

through the origin of the coordinate system, the governing differential equations and boundary conditions for the temperature distribution can be written as:

$$\frac{\partial^2 T}{\partial x^2} + \frac{\partial^2 T}{\partial y^2} + \frac{v}{\alpha} \frac{\partial T}{\partial x} = 0 \quad (8.2)$$

$$T = T_v \text{ at } x^2 + y^2 = a^2 \quad (8.3)$$

$$T(x, y) \rightarrow T_0 \text{ as } x \rightarrow \pm \infty \text{ and } y \rightarrow \pm \infty \quad (8.4)$$

where  $x$  and  $y$  are the surface coordinates,  $z$  is the depth coordinate,  $a$  is the keyhole radius,  $v$  is the welding speed,  $\alpha$  is the thermal diffusivity,  $T_0$  is the initial temperature and  $T_v$  is the vaporization temperature of the material (Carslaw and Jaeger, 1962).

After several derivations, the following equation which estimates penetration was found as (Lankalapalli, Tu, *et al.*, 1996)

$$d = \frac{P_i}{k(T_v - T_0)} \frac{1}{\sum_{i=1}^6 \frac{c_i}{i} (Pe_0)^{i-1}} \quad (8.5)$$

where  $k$  is the thermal conductivity of the material and  $c_i$  are coefficients to a polynomial fit to the equation that was evaluated numerically for 100 different values of  $Pe$  in the operating range of 0 - 0.025:

$$g(Pe) = \int_0^{2\pi} G(\theta, Pe) d\theta = C_1 + C_2 Pe + C_3 Pe^2 + C_4 Pe^3 + C_5 Pe^4 + C_6 Pe^5 \quad (8.6)$$

where

$$G(\theta, Pe) = -Pe^* e^{(-Pe \cos \theta)} * \left[ \sum_{n=0}^{\infty} \varepsilon_n I_n(Pe) \cos(n\theta) \left( \frac{n}{Pe} - \frac{K_{n+1}(Pe)}{K_n(Pe)} - \cos \theta \right) \right] = \frac{\partial}{\partial r^*} \left( \frac{T_V - T}{T_V - T_0} \right) \Big|_{r^*=1} \quad (8.7)$$

where

$$\frac{T_V - T}{T_V - T_0} = 1 - e^{(-Pe^* r^* \cos \theta)} * \sum_{n=0}^{\infty} \varepsilon_n \frac{I_n(Pe)}{K_n(Pe)} K_n(Pe^* r^*) \cos(n\theta) \quad (8.8)$$

is the closed-form solution in polar coordinates (r,θ) of the aforementioned governing differential equation with the specified boundary conditions for the temperature distribution, where Pe = v\*a / (2α) is the Péclet number, r\* = r/a is the normalized radial coordinate, ε<sub>n</sub> = 1 for n = 0 and 2 for n ≥ 1, I<sub>n</sub> is a modified Bessel function of the first kind, of order n and K<sub>n</sub> is a modified Bessel function of the second kind of order n.

Figure 8.2 shows the predicted variation of penetration in 7075-T6 aluminum with respect to changes in Péclet number, at different absorbed powers (P<sub>i</sub> = 240 – 300 W). Penetration values were calculated using equation 8.5 (see Appendix, section 12.2.1 for MATLAB model).

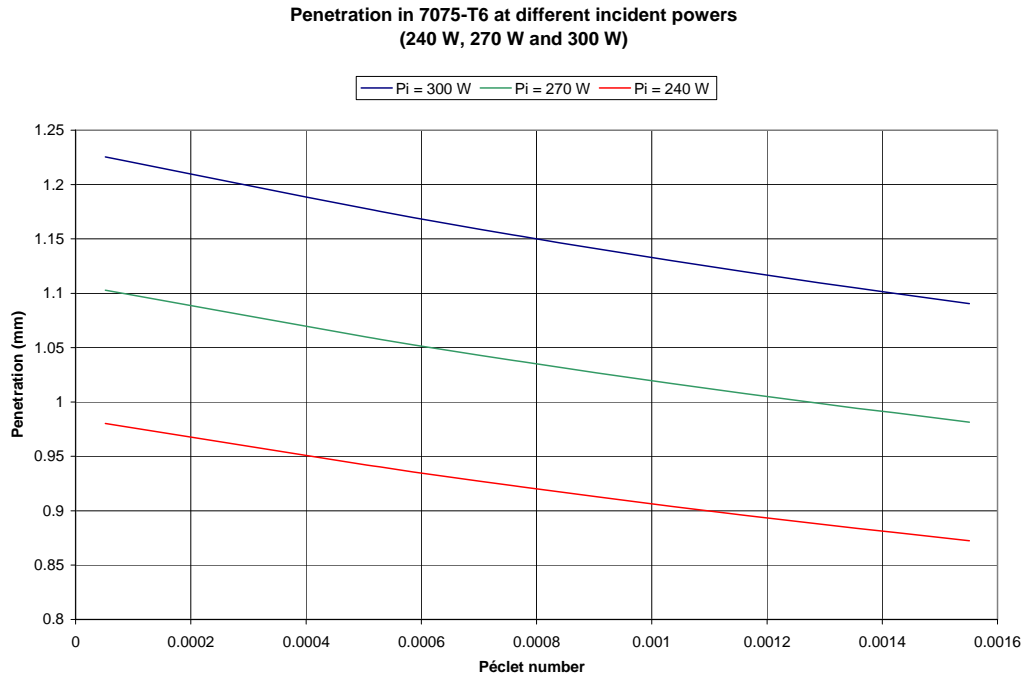


**Figure 8.2: Variation of Penetration with Change in Péclet Number**

### 8.3.1 Model Validation: High Speed Welding of SUS 304 Steel Data

In order to verify the validity of the results of this model, it is essential to be able to compare the prediction of the model with some actual experimental results. Since this model is not material specific, it was possible to use some readily available experimental results of SUS 304 (stainless steel) and show that this model is a reasonable approximation. Several SUS 304 specimens, 300 microns thick, were welded at relatively high speeds (200—1000 mm/s), and the penetration was determined from the microscope-magnified pictures that were taken (Miyamoto, *et al.*, 2003). In order to determine the operating Péclet number, apart from the welding speed and the thermal diffusivity, the keyhole radius is also required. Determining the keyhole radius is not trivial. There exists a method (Lankalapalli, Tu, *et al.*, 1996), however, to estimate the

Péclet number from the weld width. The idea is that a contour plot (Figure 8.3) can be generated for specific Péclet numbers using equation 4.8 (see Appendix 12.5 for MATLAB code), and by measuring the width of the curve corresponding to the melting temperature range, the normalized weld width ( $w/a$ ) and Péclet number can be correlated. The normalized weld width is obtained by taking twice the maximum y value (due to symmetry) of the melting temperature isotherm curve. Therefore, an equation can be calculated numerically which can be used to determine the Péclet number at the surface of the specimen, for a corresponding weld width. This technique was used to approximate the Péclet number for each of the SUS 304 experimental results (see Appendix 12.5 for MATLAB model). Figure 8.4 shows the model prediction compared to the actual results. From the chart it is apparent that the model is relatively accurate. It seems that the theoretical curves are “shifted” upwards slightly. One possible explanation for this could be that the model does not account for any of the power distribution components in Equation 8.1, other than  $P_{weld}$  and  $P_{cond}$  (it assumes 100% power absorption by the keyhole walls).

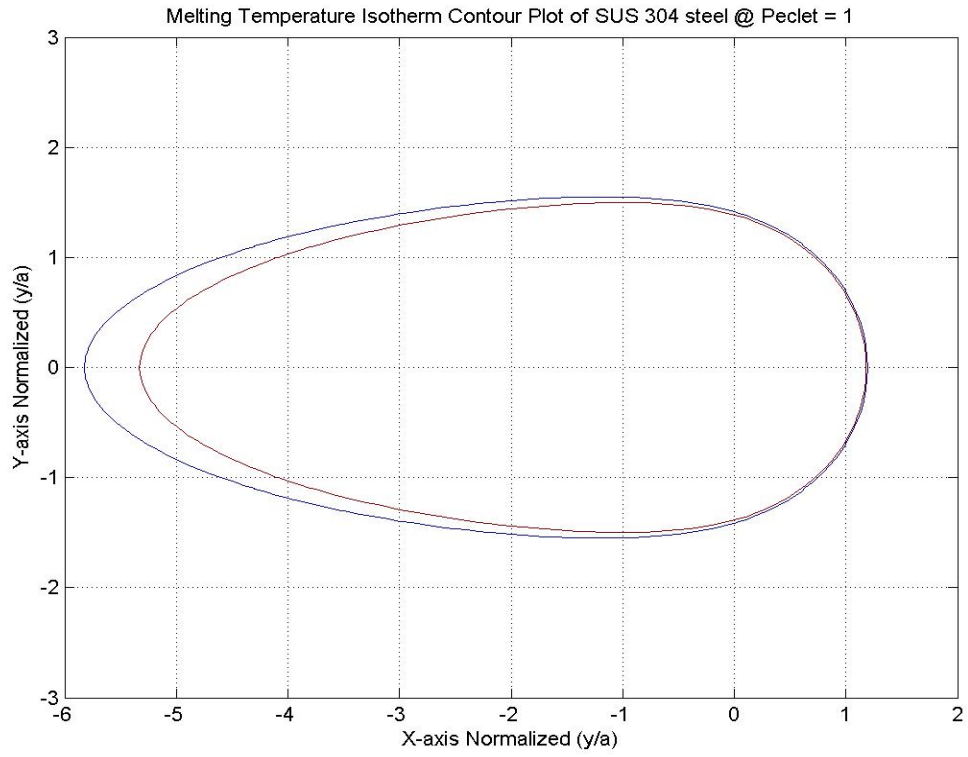


**Figure 8.3: Melting Point Isotherms of SUS 304 Steel @ Peclet = 1**

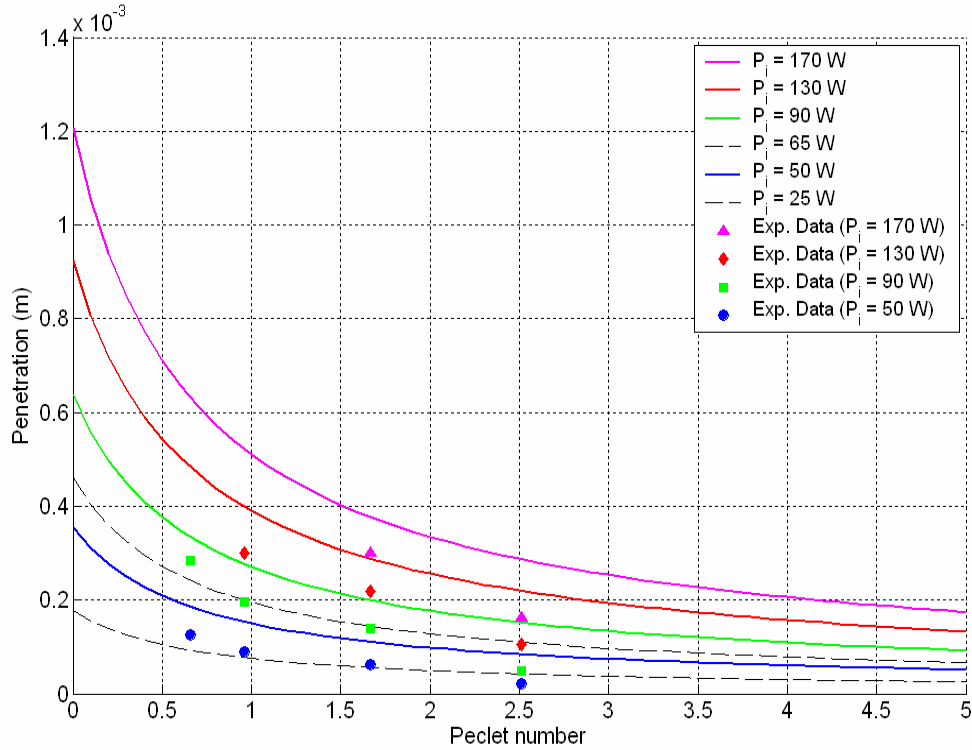


**Figure 8.4: Theoretical vs. Experimental Penetration in SUS 304**

### 8.3.2 Data Comparison of Low Speed Welding of AA 7075-T6

Now that the model has been validated, it can be used as an upper bound (ideal case) prediction for the case of low speed welding of AA 7075-T6. The solid red line in Figure 8.5 shows the prediction for the case of 100% of incident power. As explained in section 8.2 and observed in the model validation, there are power loss components in Equation 8.1 that are not accounted for in the model. However, other lines can be plotted that fit the data, which correspond to the actual power absorbed by the workpiece. In Figure 8.5, we see that for the speeds of 2, 4 and 10 mm/s the average power absorbed by the workpiece ( $P_{weld} + P_{cond}$ ) was approximately 90 % of the input power (315 W). However,

the point corresponding to 1 mm/s shows a significant decrease in penetration, with its absorbed power being only 68% of the input power. Also, by observing the cross-sections of the welds at three different processing speeds, it can be seen that the 1 mm/s weld is significantly different from the other two. The 1 mm/s weld shows a significant decrease in aspect ratio. In some cross-sections, large blowholes and porosities were present. The other two welds show more of a conical shaped cross-section, a higher aspect ratio and the absence of any major defects.

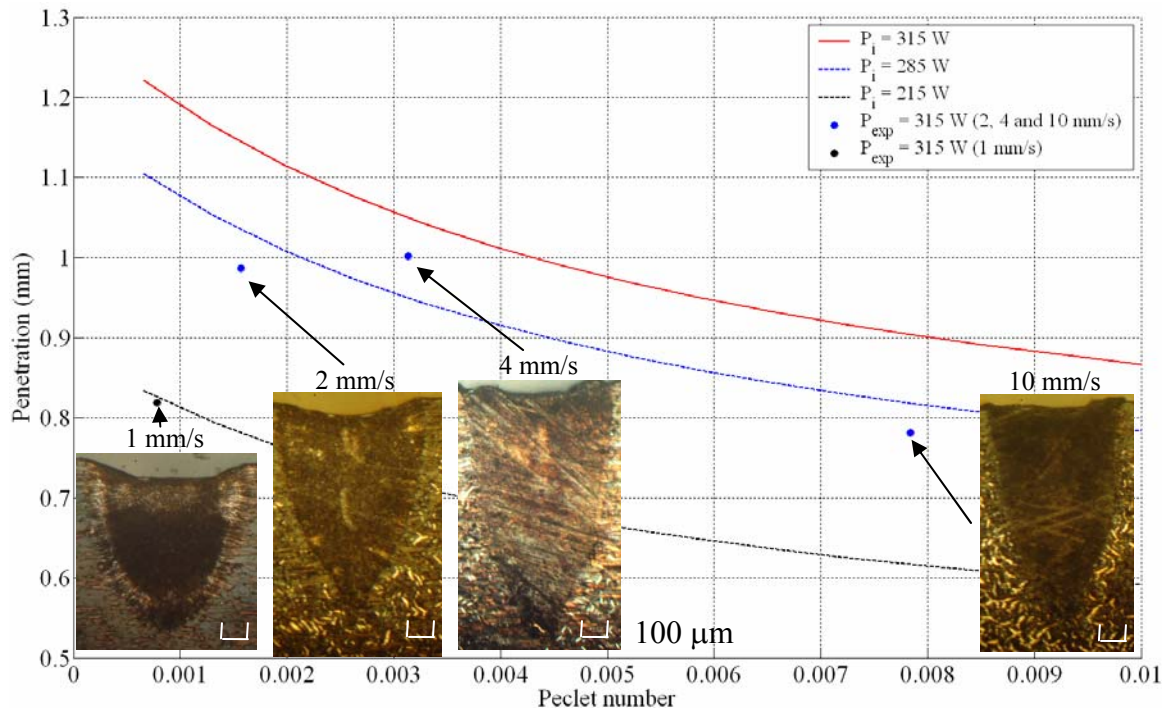


**Figure 8.5: Data Comparison at Low Speed Welding of AA 7075-T6**

This observation leads to the suspicion that at extremely low speeds the process breaks down and the laser energy is not coupled as efficiently. If this is the case, the model no longer applies to speeds below 2 mm/s.

### *8.3.3 Process Observations*

The observations that have been made so far are that the low speed welding penetration results all follow the predicted trend corresponding to a certain amount of absorbed power, until the speed drops below approximately 2 mm/s. At 1 mm/s the welds were shallower and contained major defects, as opposed to the deeper welds, which had a nice conical shape, corresponding to the assumption in the model, with no major defects present.

The study of factors preventing deep penetration at low speeds will help with the understanding of fundamental issues to improve laser welding at these speeds.

### *8.4 Effect of Various Focusing Positions on Low Speed Welding*

One of the ways to characterize the low speed laser welding process is to investigate the effects of different focusing positions. Figure 8.6 shows the change in weld penetration as the focusing position changes (positive indicating the beam is focused into the workpiece).

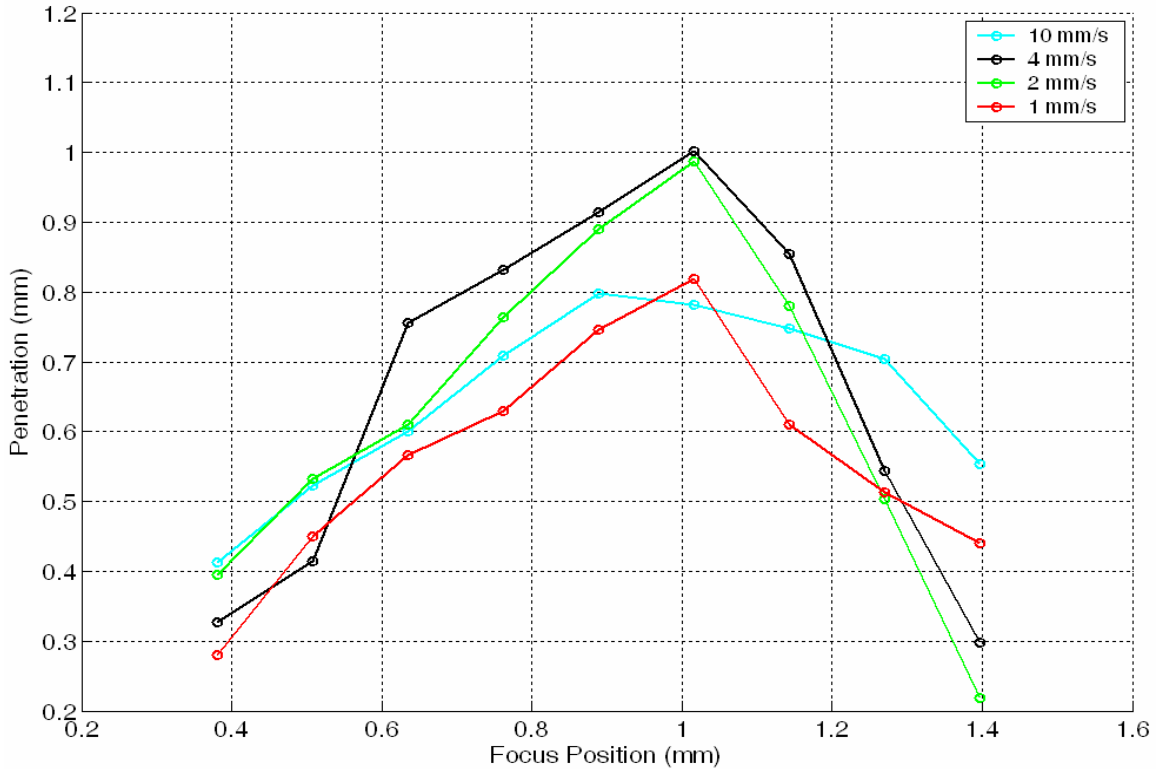


**Figure 8.6: Effects of Variation of Focusing Position on Penetration for Different Welding Speeds**

It seems, the general trend is that the best focus position corresponds with the maximum weld depth. This goes along with the recommendation for most welding processes, which is that the focus should be positioned at the desired weld depth (Steen, 2003). Another observation that can be made is that, as the beam is focused past the maximum depth location, the penetration drops at a much higher rate, with the exception of the 10 mm/s condition. This is an indication that the slower speeds are much more sensitive to focusing changes, which means that higher focusing is required to produce adequate and repeatable weld penetrations.

Specifically, for the 10 mm/s processing speed, the maximum weld penetration is approximately 0.8 mm and this occurs when the focus is approximately 0.9 mm into the

workpiece. For the 2 and 4 mm/s speeds the weld penetration is deepest (~ 1 mm) when the beam is focused approximately 1 mm into the workpiece. The difference in weld penetration (~ 0.8 mm) between these two speeds is not much, with the 4 mm/s weld being slightly deeper. However, the 1 mm/s welds show a significant drop in penetration. The initial suspicion is that the beam might be absorbed by a stronger vapor/plasma plume, and that this could be a possible explanation why this condition was so far off the model's prediction. In order to help explain what is going on with the 1 mm/s welds and why there is such a dramatic drop in penetration, the data needs to be examined in a different way that takes into account more parameters than just focusing depth.

### ***8.5 Energy Based Process Characterization***

Since weld characteristics are influenced by several different laser welding parameters (power, beam focusing, velocity, etc.), it is important to examine their variation with respect to a metric that takes all of them into account. One such metric is keyhole fluence per weld length (KF) which has been slightly modified from a previous publication (Paleocrassas and Tu, 2007) and is redefined as follows:

$$\text{KF} = \frac{P_i}{A_b} \cdot \frac{l_w}{v} \cdot \frac{1}{l_w} = \frac{P_i}{A_b \cdot v} \quad (8.9)$$

where  $P_i$  is total incident power,  $A_b$  is the outer surface area of the immersed laser beam (as calculated from the beam profile approximation, also shown in Figure 8.7),  $l_w$  is the length of the weld and  $v$  is the processing velocity. This metric represents the total irradiated energy density per weld length.

As mentioned before, due to different types of power losses during welding, the total irradiated energy density per weld length (KF) from the laser is not going to be completely absorbed by the material. Therefore it is of interest to determine the “weld efficiency” by looking at the total energy used to create the weld and how “well” it is used; for example, the same amount of absorbed weld energy could translate into a shallow and wide weld, or a deep and narrow weld. Therefore, this energy is defined as effective weld energy (EWE) per weld length and is calculated by equation 8.10.

$$EWE = \frac{m_{weld} \cdot \zeta}{\pi \cdot r_{profile}^2} = \frac{\rho \cdot V_{weld} \cdot \zeta}{\pi \cdot r_{profile}^2} = \frac{\rho \cdot A_{weld} \cdot \zeta}{\pi \cdot r_{profile}^2} \quad (8.10)$$

where  $m_{weld}$ ,  $V_{weld}$ ,  $A_{weld}$ , and  $r_{profile}$  (Figure 8.7) are the mass, volume and radius of the top profile (or half of the weld width) of the weld, respectively,  $\rho$  is the density and  $\zeta$  is the specific energy of AA 7075-T6 and is approximated by equation 4.11.

$$\zeta = C_p \cdot \Delta T + \text{Latent Heat of Fusion} \quad (4.11)$$

where  $C_p$  is the specific heat capacity and  $\Delta T$  is the temperature change between ambient temperature and the melting point.

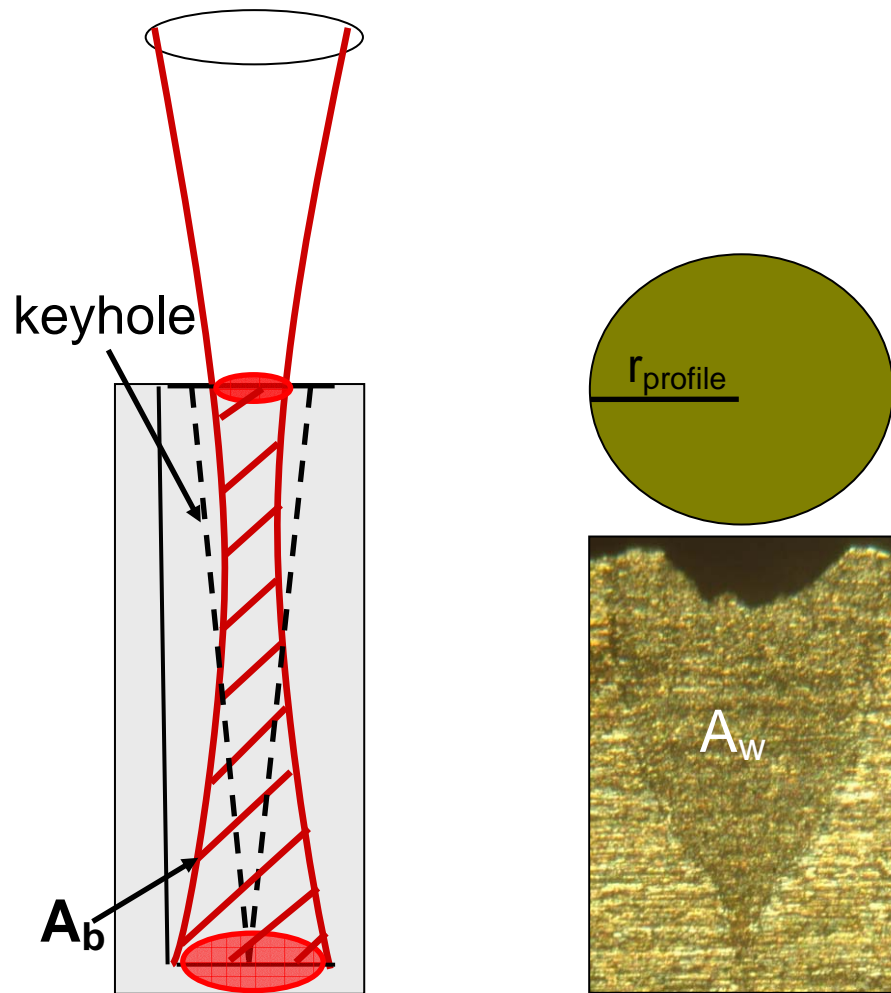


Figure 8.7: Schematics showing the submerged beam surface area ( $A_b$ ), the weld's cross-sectional area ( $A_w$ ) and the profile radius ( $r_{\text{profile}}$ )

### 8.5.1 Effective Weld Energy vs. Keyhole Fluence

Figure 8.8 was generated by applying the above energy based process characterization to the experimental data. The EWE of each data point is plotted with respect to the input KF. There are four sets of data and each set is connected by a different colored line, corresponding to a different processing speed. The 1, 2, 4 and 10 mm/s data are shown in

red, green, black and cyan, respectively. Each data point in each set corresponds to a weld created with a different focusing position. The number next to each data point represents how deep the beam is focused into the workpiece in thousands of an inch. The first observation that can be made is that for each processing speed, the point that has the highest EWE is the one where the beam was focused approximately 1 mm (.040 in.) into the workpiece, which indicates that it is the focusing condition that produces the best energy coupling. This is the case because the majority of the vapor pressure used to maintain a certain depth is created at the bottom of the keyhole. Therefore, placing the focus at the desired weld depth ensures that the maximum power density will be at the bottom of the keyhole, creating the majority of the metal vapor. However, focusing too deep can have an adverse effect on EWE because a minimum power density at the surface is required to create and maintain vaporization of the metal. This explains why the EWE decreases when the laser beam is focused too deep.

By examining the processing speed trend, it was observed that as the speed decreases, the EWE increases, until the speed drops below 2 mm/s. It can therefore be seen that the process is not only dependent on the amount of KF, but also in the manner it is deposited into the workpiece. This leads to the examination of the efficiency of the process.

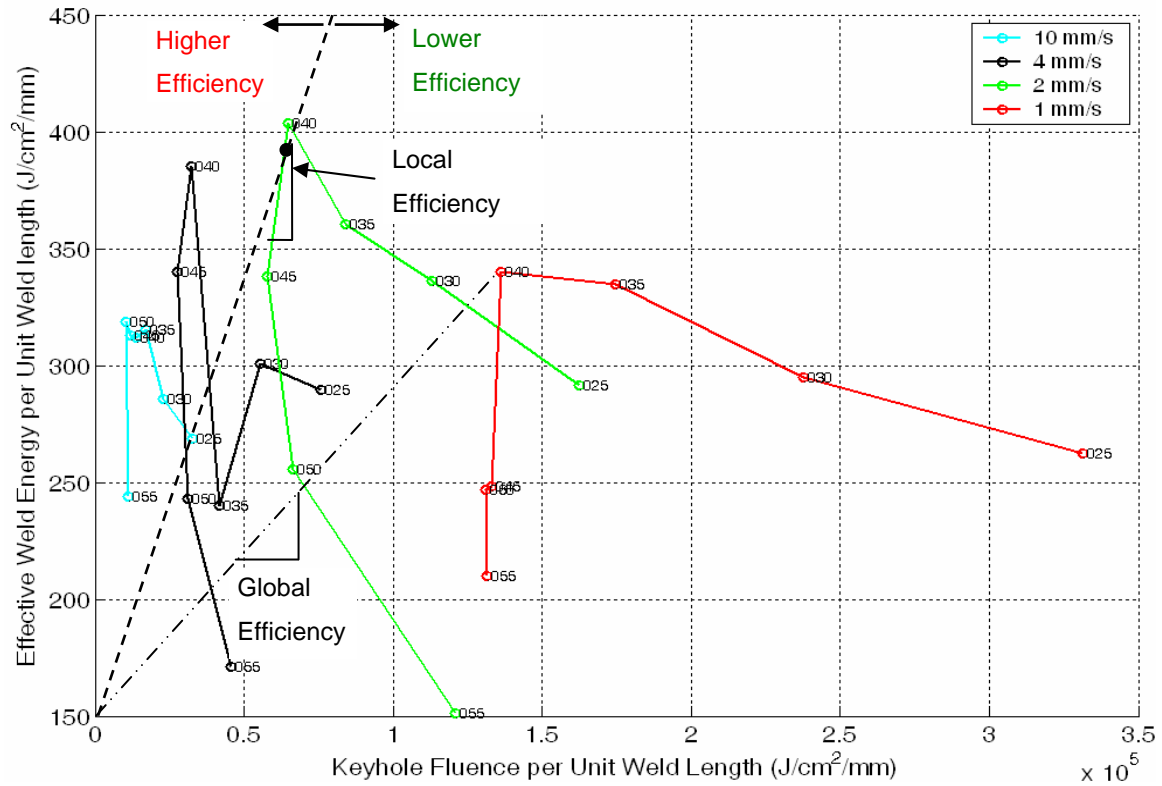


**Figure 8.8: Variation of Effective Weld Energy with respect to Keyhole Fluence**

### 8.5.1.1 “Global Efficiency”

One of the primary concerns in any process involving energy exchange is how efficient it is; in this case, that is, how much of the irradiated energy density per weld length was translated into a desirable, high aspect ratio weld. This is where we can define the “global efficiency” of the process. It is simply the ratio between EWE and KF, as stated in Equation 8.12.

$$\text{Global Efficiency} = \frac{EWE}{KF} \quad (8.12)$$

With this metric, we can determine the efficiency at each speed and at each focusing position. If we look at the actual percentages, we will see that the highest efficiency does not exceed 3 percent of the total KF. This might seem extremely low at first, but it is important to remember that this number corresponds only to the energy used to create the weld itself. During the process, apart from the power losses listed in Equation 8.1, a big portion of the absorbed power is even conducted away. Therefore the relative change in global efficiency is of more interest than the actual number itself. Looking at the four speeds we observe that the global efficiency decreases slightly from the 10 mm/s data to the 4 mm/s and then slightly lower to 2 mm/s, but drops significantly at the 1 mm/s data. This is another indication that even though there is an increase in KF, the energy is not used as effectively to create a deep and narrow weld. This phenomenon, i.e. the process breakdown of laser welding at extremely low speeds, requires further investigation to explain the reasons behind this drastic change.

#### 8.5.1.2 “Local Efficiency”

Another metric we can define to measure the efficiency between different focusing points for a specific processing speed is the “local efficiency.” The slopes of these lines can be defined as a “local efficiency” which signifies how efficient the process is, as the focusing changes and the KF increases. In other words it is the ratio of the change in EWE and the change in KF for a particular processing speed (Equation 8.13).

$$\text{Local Efficiency} = \frac{dEWE}{dKF} \quad (8.13)$$

It is apparent that the local efficiency is only positive between the weld with the best focusing position and the one that is focused slightly deeper. Again, this is evidence that

increasing the KF is not enough to create a good weld, it has to be deposited correctly. It seems that this happens because, when the beam is focused too deep, the incident power density at the surface of the workpiece is not sufficient to create enough vaporization to sustain a keyhole. The process, therefore, switches to conduction welding mode, where weld is created solely from melting, resulting in a shallow and wide weld. Conversely, if the focus is too close to the surface of the workpiece, the process is again inefficient because the power density at the bottom of the keyhole is too low and can not sustain the vaporization required for a deeper keyhole.

### ***8.6 Investigation of Poor Welding Efficiency at Low Speeds***

The key question remains, however, why the lower speed welds have such poor efficiency. Looking back at Equation 8.1 and Figure 8.5, it is apparent that the absorbed power has reduced significantly (from 285 to 215 W) and by conservation, one or more of the power loss components has increased. A well known factor to cause problems with welding is the further ionization of the vapor/plasma inside the keyhole as well as above the workpiece, to the point where it starts absorbing the laser beam. While this is usually a problem with CO<sub>2</sub> welding due to the wavelength being ten times longer than the wavelength of Nd:YAG and fiber lasers, it is still worthwhile to investigate it, because of the much higher power densities achieved in our experiments. In order to determine if there is an increase in ionization, the vapor/plasma plume was observed using a high speed camera, a silicon photodiode and a spectrometer.

### 8.6.1 High Speed Camera

High speed camera time-evolution stills for different welding speeds are shown in Figure 8.8. The stills were taken within approximately 20 ms from each other. They were taken in order to see whether the size of the plume grows as the welding speed decreases.

Typically, laser welding processes that have absorbing plasma, have plumes that grow in size as the plume keeps absorbing the laser beam (Tu, et al., 2003). From Figure 8.8, we can not see any conclusive differences in the plumes of the different speeds. This is an indication that the vapor/plasma plume remains relatively transparent to the laser beam, and is not growing as the processing speed decreases. However, the plumes in this case were quite small to begin with, which makes it hard to determine changes in size. Any other conclusions about the intensity of these plumes cannot be made, since the pictures are all overexposed.

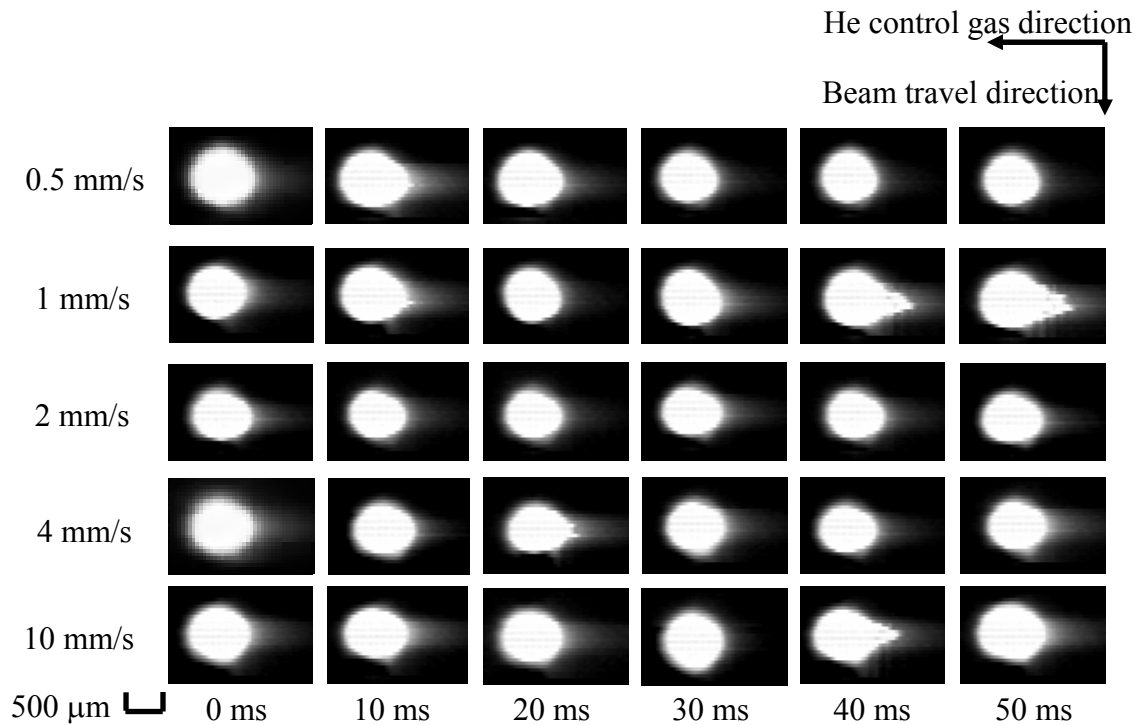


Figure 8.8: High speed camera stills; Rows from top to bottom: 0.5, 1, 2, 4 and 10 mm/s

For this reason, as well as to obtain more information on what is happening at the lowest speeds, photodiode measurements were taken to compare the relative intensities of the irradiating plumes.

### *8.6.2 Vapor/Plasma Plume Relative Intensity Measurements*

Figure 8.9 shows the steady-state measurements of the three welding conditions at different focusing positions. The green circles correspond to the maximum EWE condition and the green stars correspond to the maximum penetration condition. If we compare the three speeds at their best focusing position (max EWE and penetration), we observe that the 0.5 mm/s signals are decreasing in average intensity, rather than increasing due to the growth of the vapor/plasma plume. As a matter of fact it seems that the 0.5 mm/s generates a calmer signal than at speeds that have generated deeper and higher aspect ratio welds. This leads to the suspicion that as the speed decreases, the size and temperature of the molten pool increase and therefore it absorbs the laser radiation without creating as much vapor and therefore a signal that is not as strong or violent. Additional evidence that supports this is the low EWE, compared to the higher speed welds, which means that the weld is shallow and wide (low aspect ratio), resembling conduction rather than keyhole welding.

At higher speeds, the photodiode signal is stronger and more violent, spiking at very high frequencies. It is possible that this occurs every time new material is vaporized. When the speed is higher, the melt front (molten metal between the front of the keyhole and the solid metal) is very thin and therefore does not have the capability of transferring the heat fast enough. Therefore, the energy that is absorbed causes a phase change and therefore increased vaporization. When the speed is decreased, the molten pool surrounding the keyhole increases significantly, causing a change in the heat transfer of the process. Due

to the increase in melt volume and temperature, the heat can be conducted much more effectively through conduction as well as convection. Therefore, much less vaporization occurs which explains the reduced and calmer signal.

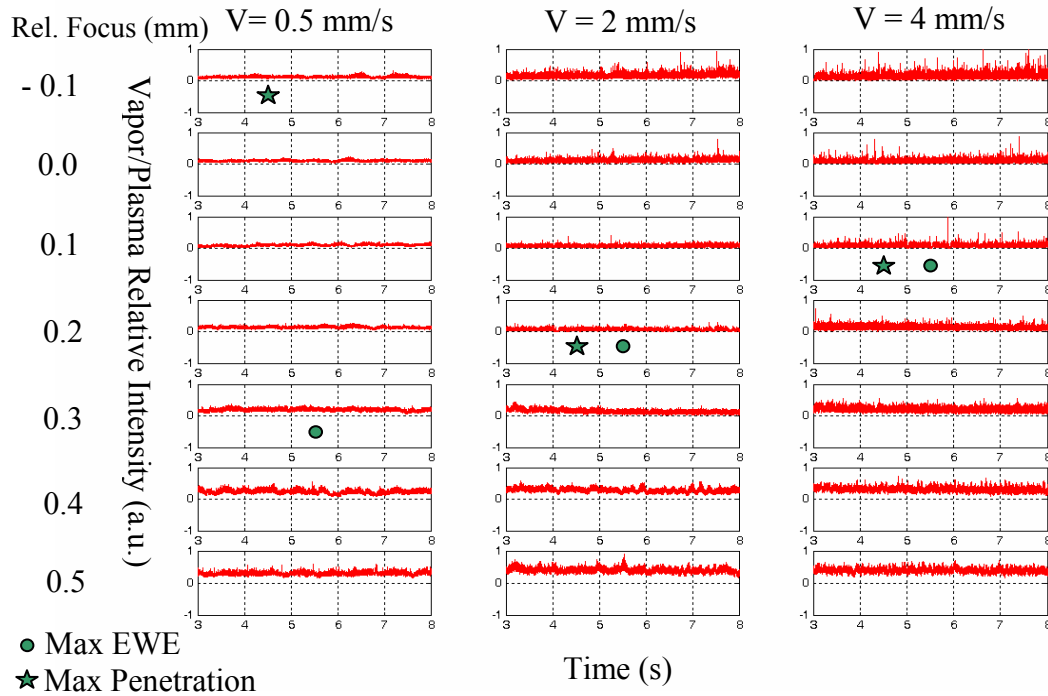


**Figure 8.9: Vapor/Plasma Plume Intensity Measurements**

### 8.6.3 Relationship between Penetration Depth and Vapor/Plasma plume intensity

Figure 8.10 shows a closer look at the relationship between penetration and vapor/plasma plume intensity. The curves corresponding to 2 and 4 mm/s show a similar trend; as average intensity increases, the penetration decreases. This trend is linear, which can prove to be very useful if a closed loop control system designed to maximize weld penetration were to be implemented.

However, looking at the 0.5 mm/s speed data, it is obvious that there is a significant penetration drop corresponding to the same average intensity. The fact that the signal is not as high as expected, supports the aforementioned theory, that there is not as much vaporization occurring because the larger and hotter molten pool is absorbing the laser beam more effectively.

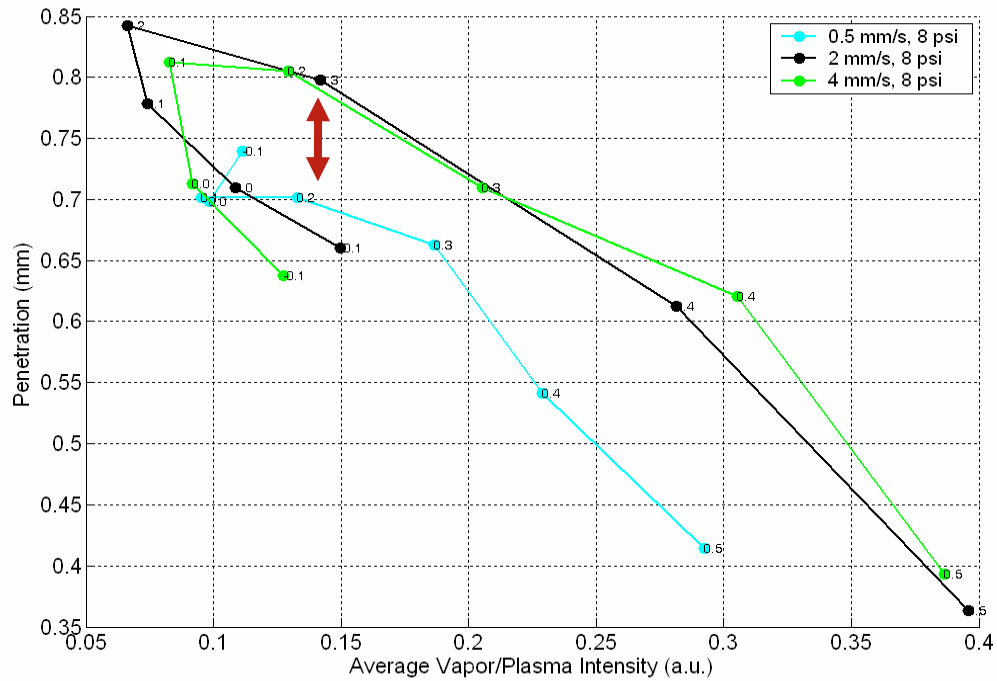


**Figure 8.10: Relationship between Penetration and Average Vapor/Plasma Intensity**

#### 8.6.4 Laser Beam Reflectivity Relative Intensity Measurements

Based on equation 8.1, the reflectivity component,  $P_{ref}$ , was a power loss source that could potentially increase or decrease as the processing speed was decreased. By investigating this power loss component it could be determined if the reflectivity from the

welding process had a significant change when the processing speed was reduced to 1 mm/s.

Figure 8.11, shows the reflected laser beam measured as a relative photodiode signal. The top plot shows the data recorded during the 10 mm/s weld, the second plot from the top shows the data from the 4 mm/s weld, the third plot from the top shows the 2 mm/s weld data and the bottom plot shows the 1 mm/s data. In every plot there is a 5 second duration in the beginning of the process, where there is a large, sudden increase in intensity which gradually dies off to almost a zero state. This is common for all cases because it corresponds to the part where the laser beam is irradiated at the stationary target for approximately 5 seconds, to initiate a keyhole. After 5 seconds have passed, the workpiece is then translated at the appropriate speed. The first 5 seconds of each signal are therefore pretty similar to each other. The value of this result is that it shows there are no significant changes occurring in between experiments, such as increased absorptivity due to pre-heating of the workpiece. Also, it shows that as the laser is first irradiated on the workpiece, there is a large amount of it reflected away, but as the keyhole is created, the reflectivity quickly decreases. Eventually, there is no signal reflected, which is an indication of the presence of a keyhole, which absorbs the beam completely through Fresnel absorption.

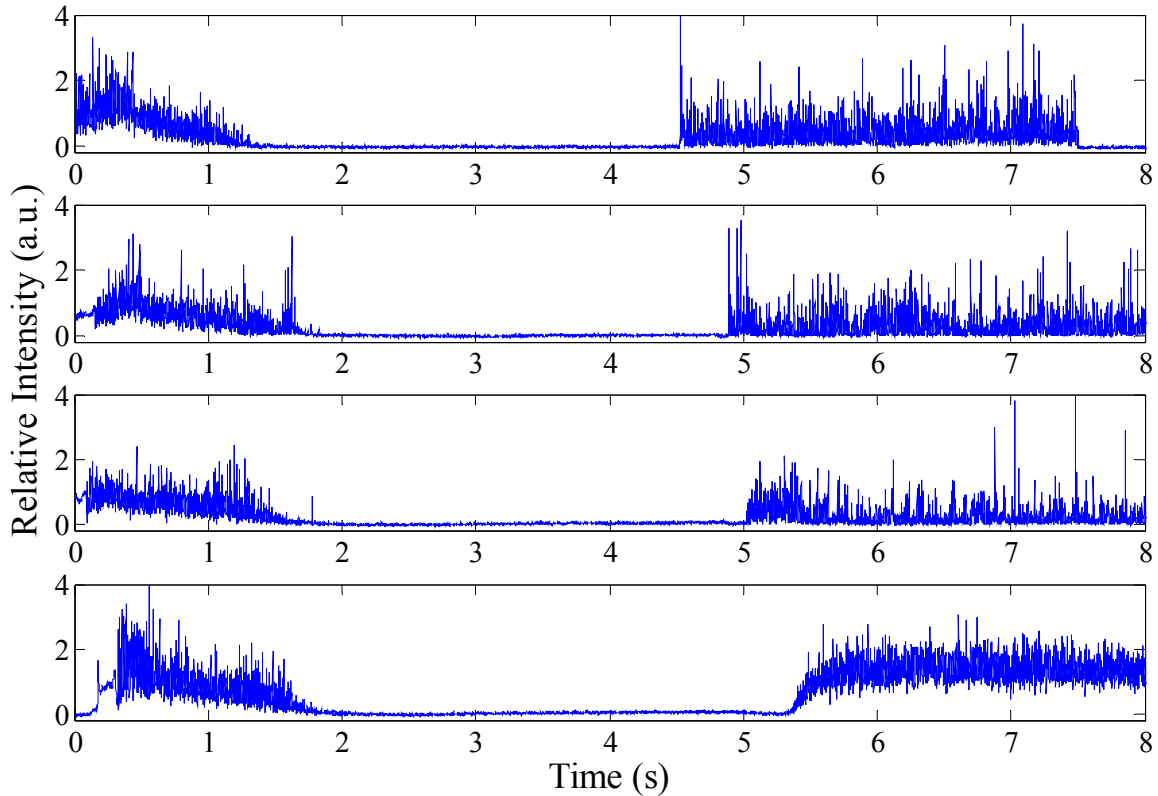


**Figure 8.11: Laser beam reflectivity relative intensity; From top to bottom: 10, 4, 2 and 1 mm/s welding conditions respectively**

When the workpiece begins to move, the reflected signal appears, again, as a series of high frequency spikes, but with a low average intensity, between 0.25 and 0.4 (a.u.). This is pretty common for processing speeds 10, 4 and 2 mm/s. The 1 mm/s processing speed shows a significantly different type of signal, where the spikes are not as strong, but the average intensity of its signal being significantly larger than the other processing conditions' signals, namely approximately 1.4 (a.u.).

The spikes in the signals can be attributed to the fact that when the laser beam moves over the solid front, the reflectivity suddenly increases; as soon as that happens, the

keyhole is created and it absorbs the beam completely, which causes a decrease in measured intensity. This pattern repeats at a frequency of approximately 30 Hz.

On the other hand, when the processing speed is 1 mm/s, the beam does not necessarily move over a solid front, since the molten pool is so large. This has, as an effect, a reduction in the strength of the spikes, since the molten metal has a higher absorptivity than solid. The increase in average intensity can be explained by the fact that the keyhole is much shallower and wider. Therefore, much more of the laser beam is reflected back out, due to the inability of the shallow keyhole to “trap” the laser beam through multiple reflections.

It can therefore be concluded that the power loss from reflectivity, increases significantly when the speed is lowered down to 1 mm/s. However, this does not necessarily mean that this increase in reflectivity is the cause of the reduction of the EWE and aspect ratio of the welds. It seems more likely that this is an added effect from the significant increase in volume of the molten pool.

#### *8.6.5 Spectroscopic Characterization of Vapor/Plasma Plume Produced during Low Speed Laser Welding.*

So far, high speed photography and photodiode measurements have shown that strong beam absorption by the vapor/plasma plume is likely not the reason for the inefficiency at the low speed welding condition. However, it is still worth while to take a look at the produced spectra to draw this conclusion with a higher certainty. Figure 8.12 shows the spectrum produced when the laser beam produced consecutive microsecond pulses on a AA 7075-T6 target, moving at an appropriate speed so as the laser pulses would hit a flat surface each time. The power of these pulses was approximately 1,500 W. This is a

unique characteristic of our fiber laser, where a “spike” in power is produced for approximately 1  $\mu$ s, before it settles to the steady state 315 W power. The reason this was done was because for aluminum welding, the produced signal was not strong enough to register any spectral lines, which is another indication of the weakness of the vapor/plasma. After examining Figure 8.12 more carefully, it was determined that produced spectra at the spectrometer’s bandwidth could not be used for spectroscopic analysis, because the three largest Al I spectral lines (383.5, 394.5 and 396.2 nm) were strongly self-absorbed and could not be identified with reasonable confidence. Furthermore, there were four additional Cr I spectral lines in the 420-430 nm range, but their relative intensities were too low for spectroscopic analysis.

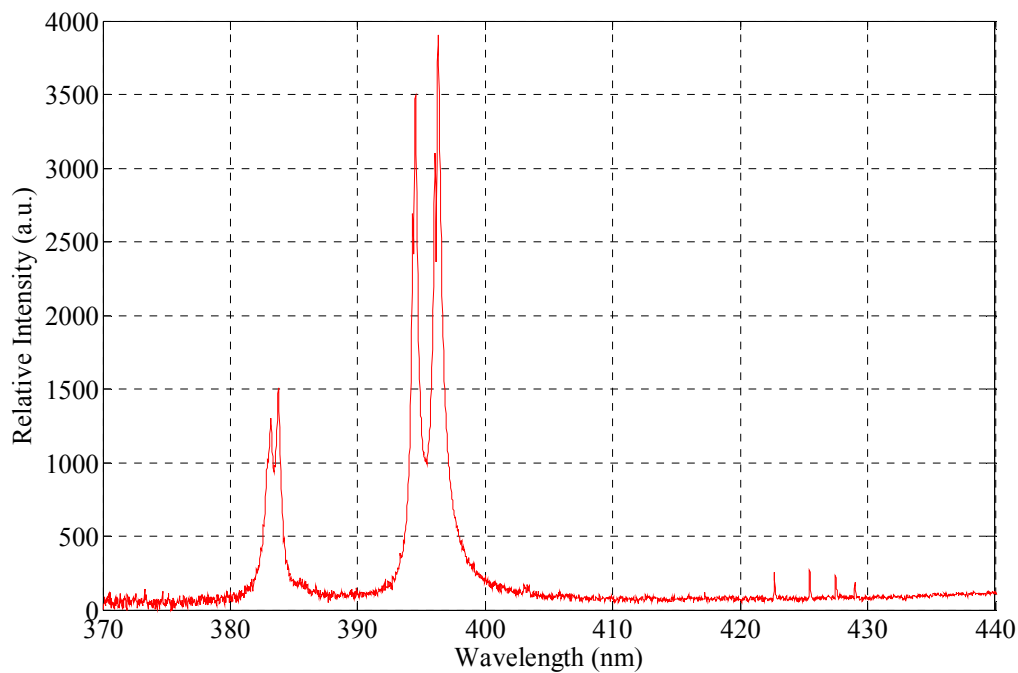


**Figure 8.12: Aluminum Vapor/plasma spectrum for 1  $\mu$ s pulsing, 100 % power (~ 1,500 W)**

Instead, spectroscopic analysis was performed in order to characterize the vapor/plasma plume produced during different laser processing conditions (drilling and welding) of stainless steel (SUS 316), since aluminum plasmas typically produce similar absorption coefficients.

The amount of laser beam absorption is determined by the level of ionization of the vapor/plasma and the laser wavelength. For Nd:YAG lasers, the vapor/plasma is usually optically thin, which means that absorption is practically negligible. However, due to the increased power densities that a fiber laser is capable of, it is possible that absorption is not negligible.

The laser beam can be absorbed through different mechanisms with the most dominant one being Inverse Bremsstrahlung (IB) absorption, which involves absorption of a photon by a free electron (Ready, 1971). The IB absorption coefficient can be approximated as the electron-ion absorption coefficient, since the absorption coefficient for electron-neutral atom coefficient can be considered negligible (Poueyo-Verwaerde et al., 1993):

$$\alpha_{IB} \approx \alpha_{e-i} \quad (8.14)$$

where:

$$\alpha_{e-i} = \left(\frac{4}{3}\right) \cdot \left(\frac{2 \cdot \pi}{3 \cdot k \cdot T_e}\right)^{1/2} \cdot \left(\frac{n_e \cdot n_i \cdot Z^2 \cdot e^6}{h \cdot c \cdot m_e^{3/2} \cdot \nu^3}\right) \cdot \left[1 - \exp\left(-\frac{h \cdot \nu}{k \cdot T_e}\right)\right] \quad (8.15)$$

where  $k$  is the Boltzmann constant,  $T_e$  is the electron temperature,  $n_e$  and  $n_i$  are the electron and ion densities in the vapor/plasma,  $Z$  and  $e$  are the average and electronic charges,  $h$  is the Planck constant,  $c$  is the speed of light,  $m_e$  is the mass of an electron and  $\nu$  is the laser frequency.

From inspection of equation (8.15), it is clear that the electron temperature and density of the vapor/plasma need to be known. There are several ways to measure electron temperature and density.

#### 8.6.5.1 Electron Temperature ( $T_e$ )

The most popular method to measure the electron temperature is that of the Boltzmann plot, assuming local thermodynamic equilibrium (LTE) conditions. It is an extension of the “two-line radiance ratio method,” where the integrated relative intensities are used to calculate temperature. The LTE condition is given as (Griem, 1964):

$$n_e \left( cm^{-3} \right) \geq 1.6 \cdot 10^{12} \cdot T_e^{1/2} \cdot (\Delta E)^3 \quad (8.16)$$

where  $\Delta E$  is the largest upper energy level gap (in eV) of the lines of interest.

When self-absorption is negligible (less than 1 %), the integrated radiance of an atomic emission line is:

$$I_{nm} = \frac{c}{4 \cdot \pi} \cdot l \cdot A_{nm} \cdot h \cdot \nu_{nm} \cdot \rho_0 \cdot \frac{g_n}{Q} \cdot \exp\left(-\frac{E_n}{k \cdot T_e}\right) \quad (8.17)$$

where  $n$  and  $m$  are subscripts referring to the upper and lower energy states respectively,  $A_{nm}$  is Einstein’s coefficient of spontaneous emission (transition probability),  $h$  is Planck’s constant,  $\nu_{nm}$  is the wavenumber of the line,  $\rho_0$  is the number density of atoms,  $Q$  is the partition function,  $g_n$  is the statistical weight (degeneracy) of

the upper state of the transition  $n \rightarrow m$  and  $E_n$  is the energy of the upper state (Tourin, 1966).

If the transition probability, statistical weight of the upper state, energy of the upper state and wavelength of each of two lines are known it follows from equation (8.18) that:

$$\frac{I_1}{I_2} = \frac{g_1 \cdot A_1 \cdot \lambda_1}{g_2 \cdot A_2 \cdot \lambda_2} \cdot \exp\left(\frac{(E_2 - E_1)}{k \cdot T_e}\right) \quad (8.18)$$

where the left side of the equation corresponds to the relative intensities of two spectral lines. Furthermore, by taking the logarithm of both sides of equation (8.18) we get:

$$\ln\left(\frac{I_1}{I_2}\right) = \ln\left(\frac{g_1 \cdot A_1 \cdot \lambda_1}{g_2 \cdot A_2 \cdot \lambda_2}\right) - \frac{(E_1 - E_2)}{k \cdot T_e} \quad (8.19)$$

and therefore the only unknown is the temperature (Tourin, 1966).

This method can be extended to many-lines and is called the Boltzmann plot. With the Boltzmann plot, each spectral line is plotted as a point in the following equation, which is derived by algebraic manipulation of equation (8.17):

$$\ln\left(\frac{I_{nm} \cdot \lambda_{nm}}{g_n \cdot A_{nm}}\right) = C - \frac{E_n}{k \cdot T_e} \quad (8.20)$$

By close inspection, it can be seen that equation (8.20) is that of a line where,  $E_n$  is the dependant variable,  $C$  is the y-intercept (and of little importance for this analysis), and the left hand side is the independant variable. After plotting these points, a linear fit can

be applied and the inverse of the line's slope will be proportional to the temperature of the vapor/plasma. This method is considered to be more accurate than the "two-line radiance ratio method," since more atomic spectral lines are being taken into account. That being said, the lines to be used have to be selected carefully, since self-absorption, low accuracy of the Einstein's coefficients and closely spaced upper energy levels can significantly affect the overall accuracy of this method.

### 8.6.5.2 Electron Density ( $n_e$ )

There are several methods that can be used to calculate electron density. One of the most commonly used methods, involves the use of the Saha ionization equation (Sokolowski et al., 1988):

$$n_e = c_1 \cdot T_e^{3/2} \cdot \frac{A_{nm}^+ \cdot g_n^+ \cdot \lambda^0 \cdot I_{nm}^0}{A_{nm}^0 \cdot g_n^0 \cdot \lambda^+ \cdot I_{nm}^+} \cdot \exp\left(-\frac{V + E_n^+ - E_n^0}{k \cdot T_e}\right) \quad (8.21)$$

where  $c_1 = 2.898 \cdot 10^{16}$  and is a constant determined by fitting equation (8.21) to a normalized  $n_e - T_e$  chart (i.e.  $I_{nm}^0 / I_{nm}^+ = 1$ ),  $V$  is the ionization energy of iron (Fe), and the superscripts '+' and '0' indicate the ionized (first ionization level) and neutral atom respectively.

However, in order to be able to use this method, one must be able to accurately measure the relative intensities of neutral and ionized spectral lines. If this is not possible, a method has been used, based on a study in which the Stark broadening of atomic spectral line Fe I (538.34 nm) has been found to be proportional to the electron density (Freudenstein and Cooper, 1979).

Specifically:

$$C_s = \frac{w_e}{n_e} = (0.0097 \pm 0.0004) \cdot 10^{-16} \text{ nm} \cdot \text{cm}^3 \quad (8.22)$$

where  $C_s$  is the Stark electron broadening constant and  $w_e$  is the half-width at half max (HWHM) intensity of Fe I (538.34 nm).

In case the particular line is out of the spectrometer's bandwidth, the results of a study by (Bengoechea et al., 2006) can be used to calculate the same constant,  $C_s$ , for the atomic spectral line Fe I (381.58 nm).

The idea is that, assuming homogeneity throughout the plume, the electron density,  $n_e$ , should be equal, regardless of what line is used to calculate it:

$$n_e(381.58) = n_e(538.34) \quad (8.23)$$

Therefore:

$$\frac{w_e(381.58)}{C_s(381.58)} = \frac{w_e(538.34)}{C_s(538.34)} \quad (8.24)$$

Knowing the ratio of HWHM of these two lines and  $C_s$  of the 538.34 line, the Stark electron broadening constant of Fe I (381.58) can be calculated:

$$C_s(381.58) = C_s(538.34) \cdot \frac{w_e(381.58)}{w_e(538.34)} \quad (8.25)$$

and then calculate the electron density by using the newly acquired coefficient for the 381.58 line.

However, due to the spatial inhomogeneity in laser-induced plasmas there are some errors in the determination of Stark electron widths.

So Equation (8.25) was modified to the following:

$$error = \left( 1 - \frac{R_m}{R_t} \right) \times 100 \quad (8.26)$$

where

$$R_m = \frac{w_e(381.58)}{w_e(538.34)} \text{ and } R_t = \frac{C_s(381.58)}{C_s(538.34)} \quad (8.27)$$

Using a model that was developed to account for errors in Stark electron broadening a graph was generated that showed that the error varies between 1% and 7% depending on the upper energy level of the line.

Finally, by plotting data of the HWHM of both lines (with respect to each other) for different pulse temporal windows, it was found that the data fitted a straight line pretty

well ( $R^2 = 0.9954$ ). The slope of that line gives  $R_m = \frac{w_e(381.58)}{w_e(538.34)} = 0.057 \pm 0.002$  and

therefore the only unknown is  $C_s$  for the 381.58 nm line. The electron density can then be calculated by measuring the HWHM of Fe I (381.58 nm) and using the respective Stark electron broadening constant.

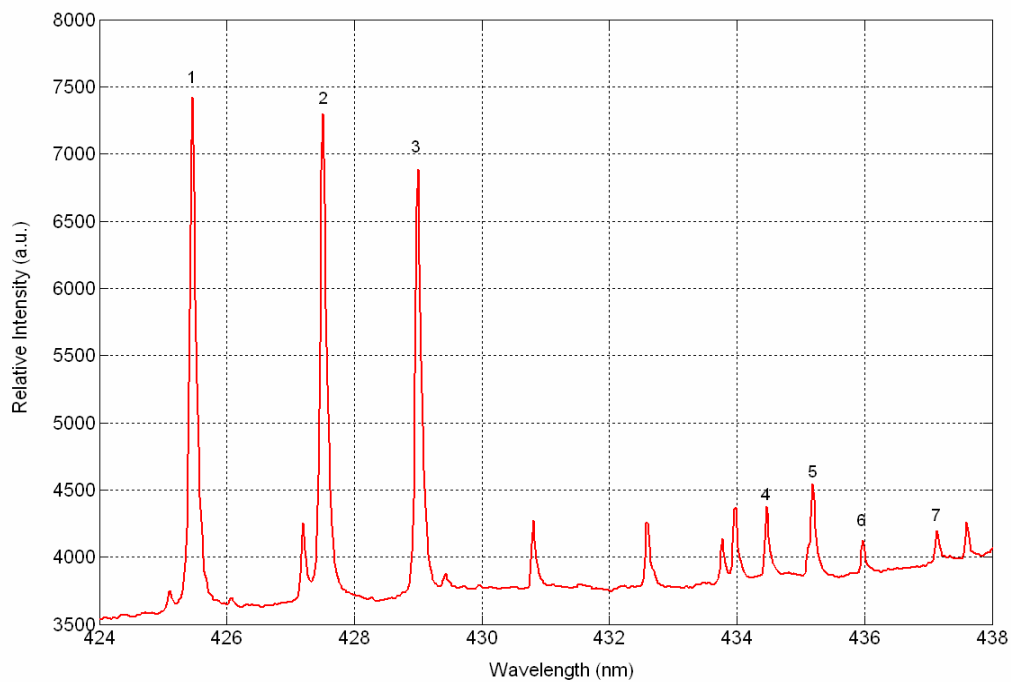
#### 8.6.5.3 Electron Temperature Estimation

Boltzmann plots were generated using both chromium and iron neutral atom transition lines in order to check for consistency. The lines that were used are listed in Table (8.1). Along with the wavelengths of the lines, table (8.1) lists their transition probabilities ( $A_{nm}$ ) and their respective accuracies, their degeneracies ( $g_n$ ) and their upper energy levels ( $E_n$ ) (NIST Atomic Spectra Database):

Table 8.1: Cr I and Fe I Atomic Spectral Line Data

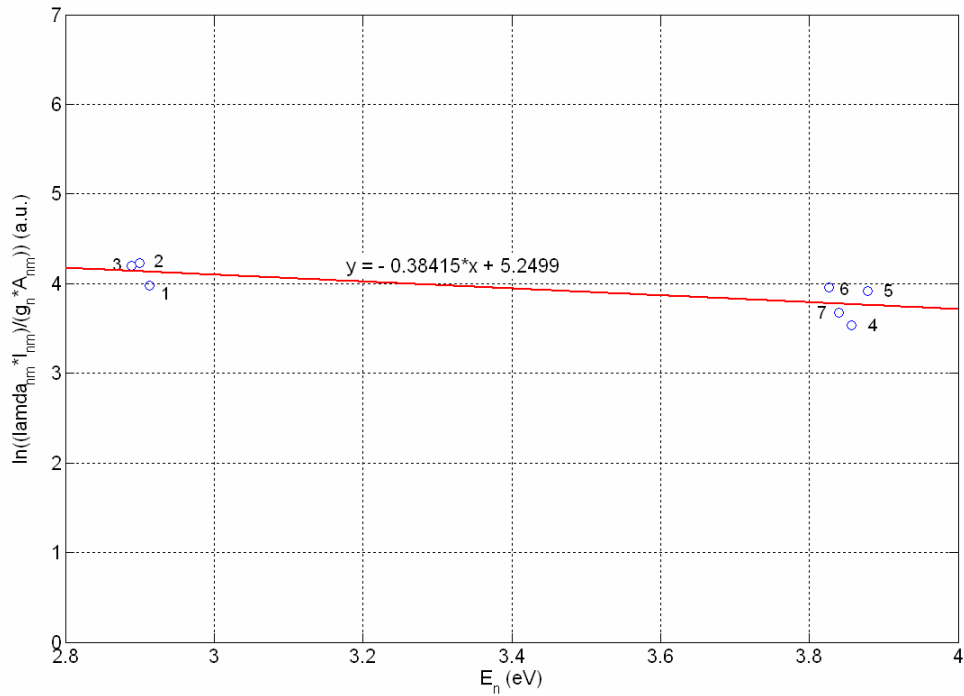
No.	Line Type	$\lambda_{nm}$ (nm)	$A_{nm}$ ( $10^8 s^{-1}$ )	Accuracy (%)	$g_n$	$E_n$ (eV)
1	Cr I	425.4332	0.3150	$\leq 10$	9	2.9134850
2	Cr I	427.4796	0.3070	$\leq 10$	7	2.8995380
3	Cr I	428.9716	0.3160	$\leq 10$	5	2.8894530
4	Cr I	434.4496	0.1100	$\leq 25$	9	3.8566980
5	Cr I	435.1755	0.1200	$\leq 25$	11	3.8782690
6	Cr I	435.9617	0.0540	$\leq 25$	5	3.8260060
7	Cr I	437.1264	0.0410	$\leq 25$	7	3.8392270
8	Fe I	371.9935	0.1620	$\leq 7$	11	3.3320192
9	Fe I	381.5840	1.3000	$\leq 18$	7	4.7331399
10	Fe I	382.0425	0.6680	$\leq 7$	9	4.1033730
11	Fe I	385.9911	0.0970	$\leq 7$	9	3.2111889
12	Fe I	404.5813	0.8630	$\leq 7$	9	4.5485043
13	Fe I	407.1737	0.7650	$\leq 7$	5	4.6520303
14	Fe I	427.1759	0.2280	$\leq 7$	11	4.3864622
15	Fe I	438.3544	0.5000	$\leq 7$	11	4.3124697
16	Fe I	440.4750	0.2750	$\leq 7$	9	4.3713502

Figure (8.13) shows the spectrum of the vapor/plasma for one of the processing conditions (pulsing, 100 % power) which includes the chromium lines used to generate the Boltzmann plots. The lines are identified according to the number scheme listed in table (8.1).



**Figure 8.13: Vapor/plasma spectrum for 1  $\mu$ s pulsing, 100 % power (~ 1,500 W)**

Since the lines experience a certain degree of broadening, the lines were fitted to Lorentzian profiles and then integrated to obtain the relative intensities. Using these relative intensities, Boltzmann plots were generated for each condition. The corresponding Boltzmann plot to the spectrum in Figure (8.13) is shown in Figure (8.14).



**Figure 8.14: Boltzmann plot for 1  $\mu$ s pulsing, 100 % power (~1,500 W)**

Using the same process, Boltzmann plots were generated for each processing condition, using both chromium and iron lines. Table (8.2) summarizes the temperature results.

Table 8.2: Electron temperatures calculated from Boltzmann plots using two sets of lines

	Using Cr I lines	Using Fe I lines
<b>1 <math>\mu</math>s pulsing, 1,500 W</b>	30,208 °K	13,342 °K
<b>1 <math>\mu</math>s pulsing, 1,050 W</b>	29,482 °K	16,456 °K
<b>1 mm/s welding, 300 W</b>	8,290 °K	8,303 °K

It is obvious there is a discrepancy between the chromium and iron lines. This is likely due to the fact that the iron lines exhibit strong self-absorption at temperatures higher

than 10,000 °K. If self-absorption is larger than ~ 1%, then the vapor/plasma is considered to be optically thick and the temperature results will be skewed. The chromium lines can be trusted because of the much lower chromium content in stainless steel. At low temperatures, however, we can see that self-absorption is not an issue, since the two temperatures (measured with different line types) are in agreement.

#### *8.6.5.4 Electron Density Estimation*

Since it was determined that the iron lines experience self-absorption at high temperatures, the electron densities can only be roughly estimated at the high power conditions. Still, they are worth calculating, in order to get an idea of how much of the laser beam is being absorbed by the vapor/plasma.

The Stark widths were obtained by fitting the Fe I (381.58) lines with Lorentzian profiles and obtaining the HWHM values. Since the error due to inhomogeneity of the vapor/plasma depends on the upper energy level of the spectral line, it was determined that the corresponding error for the Fe I (381.58) line is approximately 3 % (Bengoechea et al., 2006).

Using Equations (8.23-8.27) the estimations for the electron densities were calculated, and are listed in Table (8.3).

Table 8.3: Electron densities for various processing conditions based on Stark electron broadening of Fe I (381.58)

	$n_e$ (cm <sup>-3</sup> )
<b>1 <math>\mu</math>s pulsing, 1,500 W</b>	17.2·10 <sup>17</sup>
<b>1 <math>\mu</math>s pulsing, 1,050 W</b>	15.5·10 <sup>17</sup>
<b>1 mm/s welding, 300 W</b>	10.5·10 <sup>17</sup>

#### 8.6.5.5 Absorption Coefficient Estimation

Since the electron temperatures and densities have been estimated, it is possible to come up with an estimation for the absorption coefficients. Table (8.4) shows the absorption coefficients calculated based on Equation (8.15).

Table 8.4: Absorption coefficients for various processing conditions

	$\alpha$ (cm <sup>-1</sup> )
<b>1 <math>\mu</math>s pulsing, 1,500 W</b>	0.1042
<b>1 <math>\mu</math>s pulsing, 1,050 W</b>	0.0873
<b>1 mm/s welding, 300 W</b>	0.1658

From inspection of Table (8.4) it is clear that the absorption coefficients are smaller than what's typically seen with CO<sub>2</sub> lasers ( $\alpha \approx 0.35$  cm<sup>-1</sup>,  $T_e \approx 7,000$  °K,  $n_e \approx 10^{17}$  cm<sup>-3</sup>) (Poueyo-Verwaerde et al., 1993), lasers ( $\alpha \approx 0.57$  cm<sup>-1</sup>,  $T_e \approx 8,500$  °K,  $n_e \approx 1.5 \cdot 10^{17}$  cm<sup>-3</sup>) (Tu et al., 1993).

It is important to note here, that the welding condition produced a larger absorption coefficient than the pulsing conditions. This is probably due to the fact that self-absorption at higher temperatures caused a reduced Stark width measurement, and the

electron densities were underestimated. For example, a miscalculation of electron density of approximately 25 percent (increase) can result in a change in the absorption coefficient from 0.1042 to 0.1880 (approximately 50 percent increase).

The main conclusion to be drawn from these calculations is that the absorption coefficients calculated here are not as high as seen with CO<sub>2</sub> welding and therefore, they are expected to be similar for AA 7075-T6.

#### *8.6.5.6 Aluminum Plasma Temperature based on Measured Spectrum*

Even though only three Cr I lines could be detected in the aluminum pulsing spectroscopic experiment, it was deemed worthwhile to come up with an electron temperature estimation using the aforementioned Boltzmann plot method. The Cr I spectral lines that were used were of the same wavelength as in the steel vapor/plasma analysis (1, 2 and 3 from Table 8.1).

These lines are shown in Figure 8.15, which is a zoomed in version of Figure 8.12.

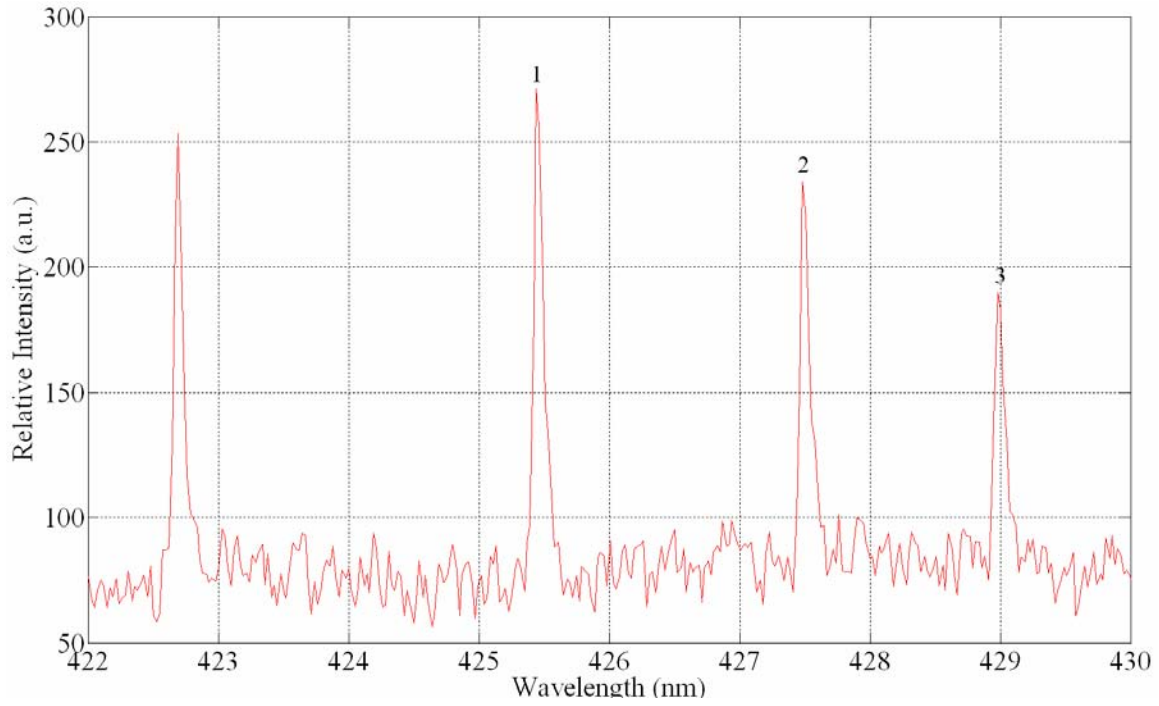


**Figure 8.15: Zoomed in aluminum vapor/plasma spectrum for 1  $\mu$ s pulsing, 100 % power (~ 1,500 W)**

The resulting Boltzmann plot from these three lines is shown in Figure 8.16.

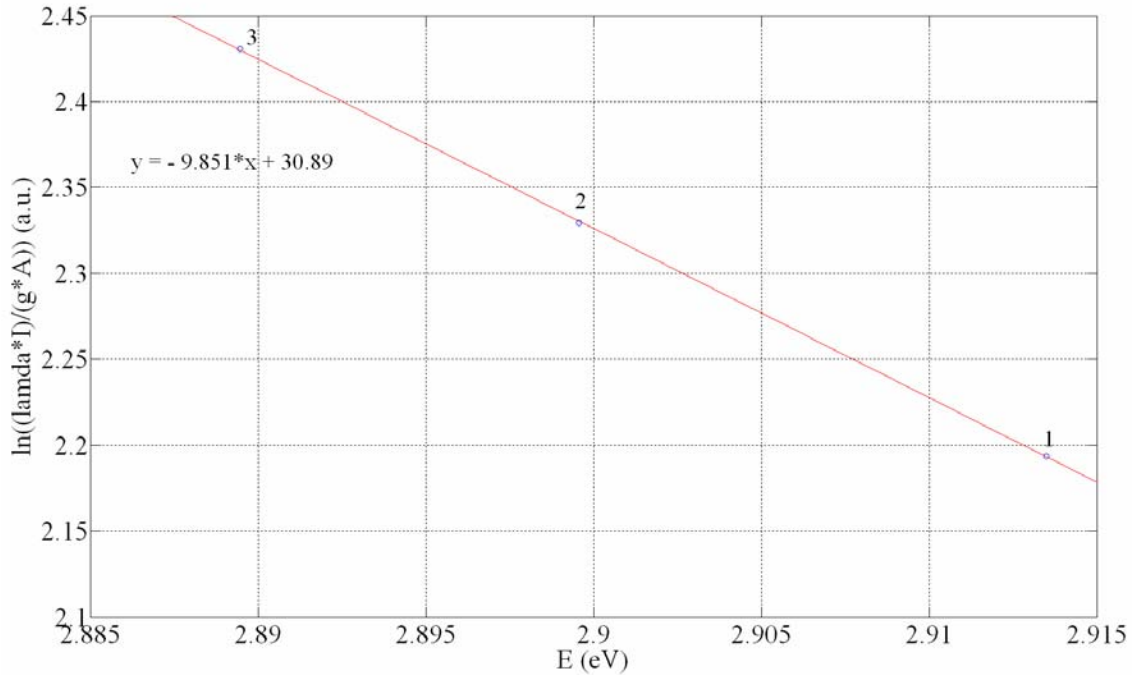


**Figure 8.16: Boltzmann plot for aluminum vapor/plasma spectrum for 1  $\mu$ s pulsing, 100 % power (~ 1,500 W)**

Based on the slope of the fitted line, the resulting temperature estimation is approximately 1,178 degrees Kelvin. This value is well below the vaporization temperature of aluminum, which indicates that the calculation is not entirely accurate. This is probably because the upper energy levels are very close to each other, which means that there is quite a bit of room for error. Nevertheless, based on this calculation and the fact that the rest of the Cr I lines with higher upper energy levels could not be detected, indicates that the temperature of the vapor/plasma should barely exceed the vaporization temperature.

#### 8.6.5.7 Aluminum Plasma Temperatures in other studies

Another way to verify that the vapor/plasma is optically thin for our welding conditions, is to examine other research studies of Nd:YAG laser welding of aluminum alloys. In this section a selection of studies will be mentioned, in order to get an idea of what typical vapor/plasma characteristics have been observed.

Kim and Matsunawa (1996) used a pulse shapeable YAG laser with irradiations of up to  $1 \text{ MW/cm}^2$  on 5000 series aluminum alloys and determined that the vapor/plasma plume was very weakly ionized, with approximate temperatures around 3280 K (barely above the vaporization temperature of aluminum) and electron densities of approximately  $1.85 \cdot 10^{13} \text{ cm}^{-3}$ . Kim et al. (2004) did a similar study and found similar results for even higher irradiations ( $\sim 32 \text{ MW/cm}^2$ ), namely the vapor/plasma temperature was very close to the boiling point of aluminum.

Another group (Lenk et al., 1996) experimented with a Q-switched Nd:YAG laser, operating at power densities of  $300 \text{ MW/cm}^2$ , determined electron temperatures of approximately 14,000 K and electron densities of  $3 \cdot 10^{16} \text{ cm}^{-3}$ , and concluded that they “are not high enough for significant absorption by inverse bremsstrahlung.” There have been several other studies (Barthélemy et al., 2005, Lu et al., 1998, Knudtson et al., 1987), that have found electron temperatures ranging from 5,000-15,000 K and electron densities up to the order of  $10^{18} \text{ cm}^{-3}$ , all reaching the same conclusion that IB absorption is not significant, and therefore the vapor/plasmas can be considered optically thin.

### 8.7 Pulsed Welding Experiments for the Improvement of Aspect Ratio, Efficiency and Weld Quality

In order to test the hypothesis formed in the second objective, a variety of different pulsing conditions was tested. The second objective stated that “overheating of the molten pool by a laser beam leads to reduced penetration, low efficiency and large porosities; turning off the laser beam until it moves to a solid front, will create welds with higher efficiency and improved aspect ratio while at the same time eliminate any defects.” Since it was of interest to find good welding conditions at a very low speed, all the experiments were performed at the same low speed, which was 0.5 mm/s, and the best focus position (determined from previous welding) of approximately 100  $\mu\text{m}$  into the workpiece. The pulse durations tested were 0.5 ms, 10 ms, 100 ms, 500 ms and 1000 ms. The duty cycle was determined in such a way, so as to make the spot welds have an 80% overlap percentage, which is a typical industry standard (Ready, 2001). Figure 8.17 shows one of the cross-sections for each pulsing condition.

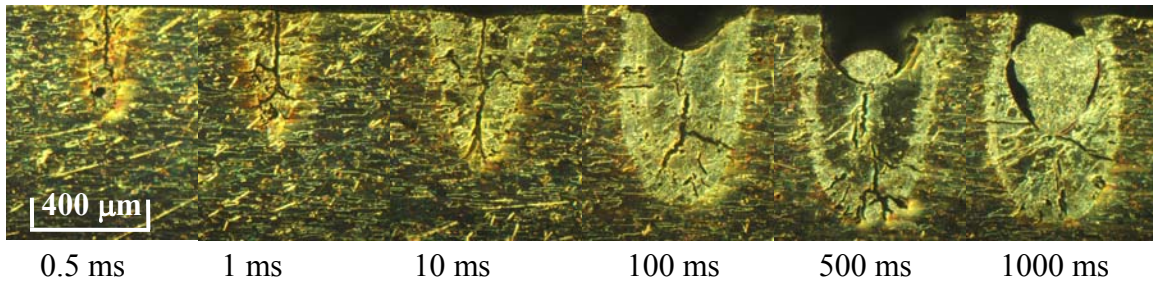


**Figure 8.17: Pulsed Welding Cross-Sections for Pulse Durations ranging from 0.5 – 1000 ms**

The welds with low pulse durations (0.5-100 ms) have a very nice conical shape with minimal underfill, whereas the longer pulse durations (100-1000 ms) resemble the CW weld cross-sections, showing wider and not-so conical cross-sections and an increased amount of underfill, strongly resembling CW welds. In order to get a better idea of

changes in weld width, penetration depth, aspect ratio and efficiency, the data was plotted with respect to the input KF.

### 8.7.1 Weld Width and Penetration Depth vs. Keyhole Fluence

Figure 8.18 shows the plots of the weld widths and penetration depths of the pulsed welds seen in Figure 8.17.

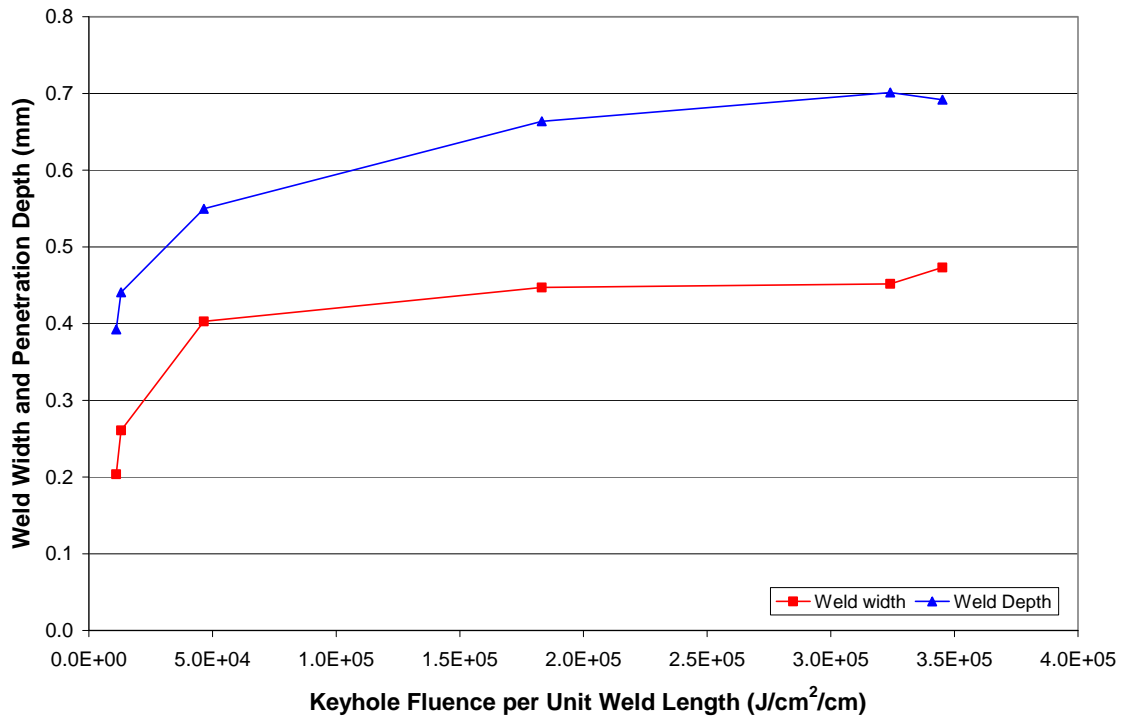


**Figure 8.18: Variation of Weld Width and Penetration Depth with increasing Keyhole Fluence**

The trend shown is that both penetration depth and weld width initially show sharp increases as more KF is input. This intuitively makes sense because there is more available power that can be used to create wider and deeper welds. However, the slopes

of the curves level off significantly, showing that eventually the material is able to transfer away the excess energy. This shows that there is a limit to how much energy can be used to create a weld. Finally, the last data points show that while the material is able to conduct away the excess energy, the welds become wider and shallower which signifies that the absorption mechanism is changing from keyhole to conduction welding mode, resembling what is happening with the CW welds at that speed. This makes sense because the high KF pulsed welds have increased duty cycles, which are approaching 100 % (CW).

### *8.7.2 Aspect Ratio vs. Keyhole Fluence*

Another important parameter in laser welding is the aspect ratio because while the penetration depth dictates how thick of a specimen can be welded, it's equally important to minimize the weld width as much as possible in order to keep the HAZ as small as possible. Figure 8.19 shows the aspect ratios of each pulsed welding condition as KF increases.

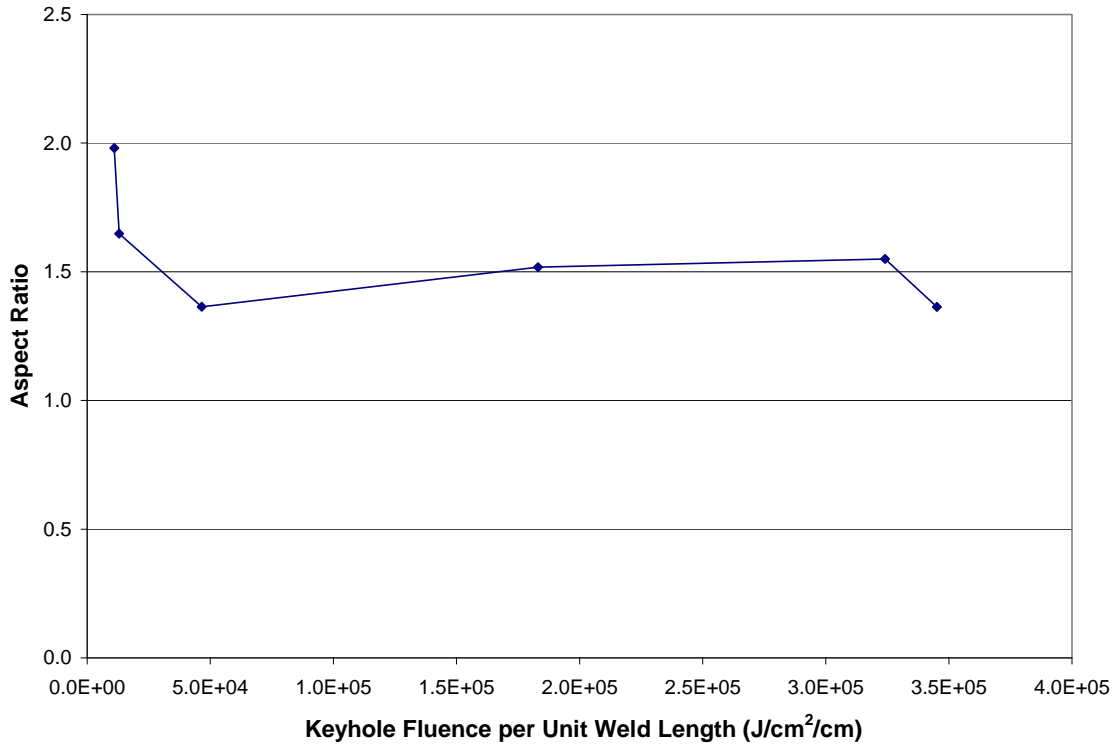


**Figure 8.19: Variation of Aspect Ratio with Increase in Keyhole Fluence**

For the first three welding conditions the aspect ratio shows a significant drop. This is fairly logical because as the penetration reaches its maximum, more energy is absorbed through the side walls resulting in a larger increase in weld width. After the third pulsing condition, however, the aspect ratio “jumps” when the KF increases by approximately 4 times. Initially, this might be puzzling. A possible explanation for this phenomenon might be that the increase in KF caused a significant increase in vapor pressure, thereby increasing the penetration and therefore the aspect ratio, since the penetration of the weld is mainly dictated by the vapor pressure creating a deep slender cavity in the molten pool. From that point on, the weld width started growing again resulting in the drop of the aspect ratio as expected.

### 8.7.3 Relative EWE and “Global Efficiency” vs. Keyhole Fluence

The relative EWE and “Global Efficiency” have been plotted in Figure 8.20. For EWE the density and specific energy were not used in the calculation, since they are the same for all data points, which are going to be compared to each other. Therefore, the EWE and Global Efficiency are relative and have arbitrary units.

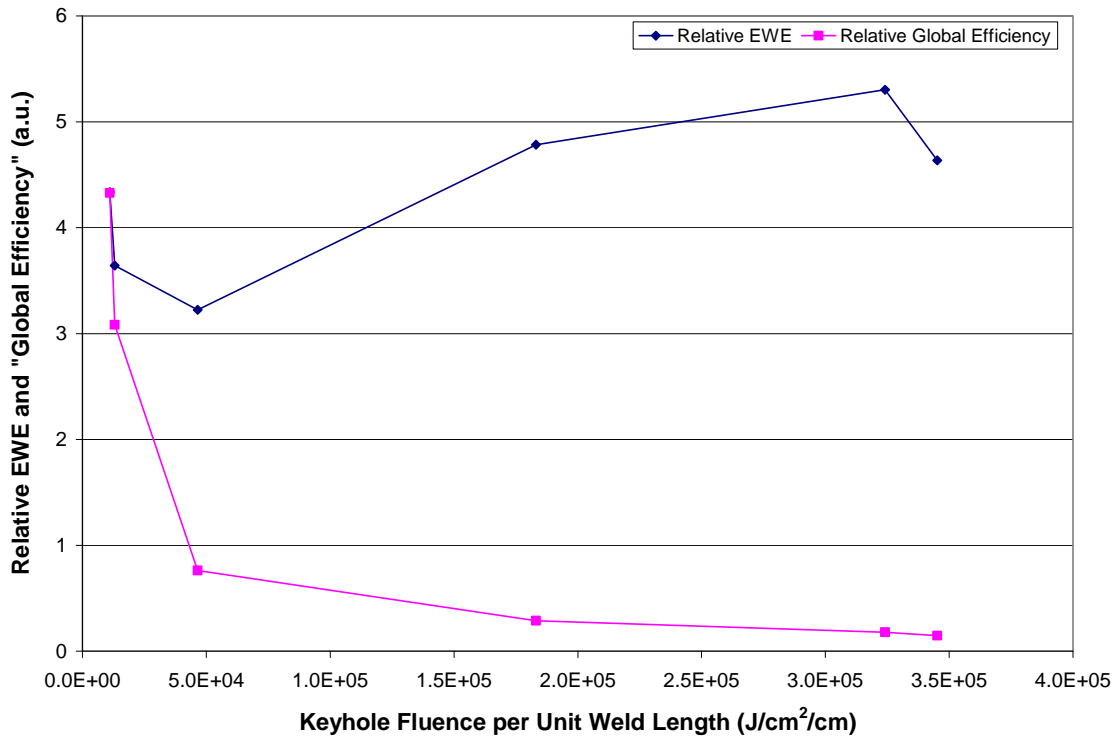


**Figure 8.20: Variation of EWE and “Global Efficiency” with Increase in Keyhole Fluence**

From examining the relative EWE trend, it seems that there is a similarity with the aspect ratio data discussed in the previous sections. Again, there is a drop in relative EWE in the first three pulsing conditions and then it starts increasing up to the last point where the relative EWE drops again slightly.

However, looking at the “global efficiency” trend, it is clear that as the pulse duration (and also duty cycle) increases, approaching the CW condition, the “global efficiency” keeps decaying seemingly exponentially. This confirms the first hypothesis, which states that when pulsing the laser, the efficiency in creating welds will increase. However, the aspect ratio, although it improves to some point, doesn't follow exactly the expected trend. This could be because there are different pulse duration regimes that create significantly different vapor pressure changes, which in turn affect the penetration.

#### *8.7.4 Selecting Best Pulsed Welding Condition*

After examining the pulsed welding data, selecting the best pulsed welding condition is not as simple as choosing the best efficiency weld. The most important criteria for choosing a welding condition is most definitely weld quality. If the weld is full of defects, not much else matters as the weld will have high stress concentration locations and will reduce the joined material's mechanical strength properties and especially resistance to fatigue cracking. The CW welds at 0.5 mm/s cannot serve as a welding solution, due to the fact that it's filled with blowholes and other porosities and has large underfills.

As the pulse duration decreases, the pulsed welds show a significant improvement in underfill and blowholes. However, it is obvious that all of them experienced pretty severe solidification cracking. This is one of the worst defects a weld can have, since a crack already exists and can be propagated to critical lengths under even the slightest fatigue loads. This cracking occurs due to the very high temperature gradients occurring when the laser turns on and off very suddenly. This is a problem that needs to be solved if pulsed welds were to be a viable solution for fusion of fatigue cracks.

Assuming the cracking problem can be solved, certain criteria need to be established for selecting the best pulsing condition. Weld width and penetration depth have to be the first criteria since the thickness of the workpiece will determine the minimum penetration depth and the joint gap will determine the minimum thickness. The weld with the highest “global efficiency” of the remaining welds that met the joint geometry criteria should be selected, to ensure the most efficient process.

#### *8.7.5 Vapor/Plasma Plume Intensity comparison: CW vs. Pulsing*

Since the low pulse duration pulsed welding condition created a significantly different result than the CW welding at low speeds, it was of interest to obtain relative intensity measurements between the 100 ms pulses and the CW conditions.

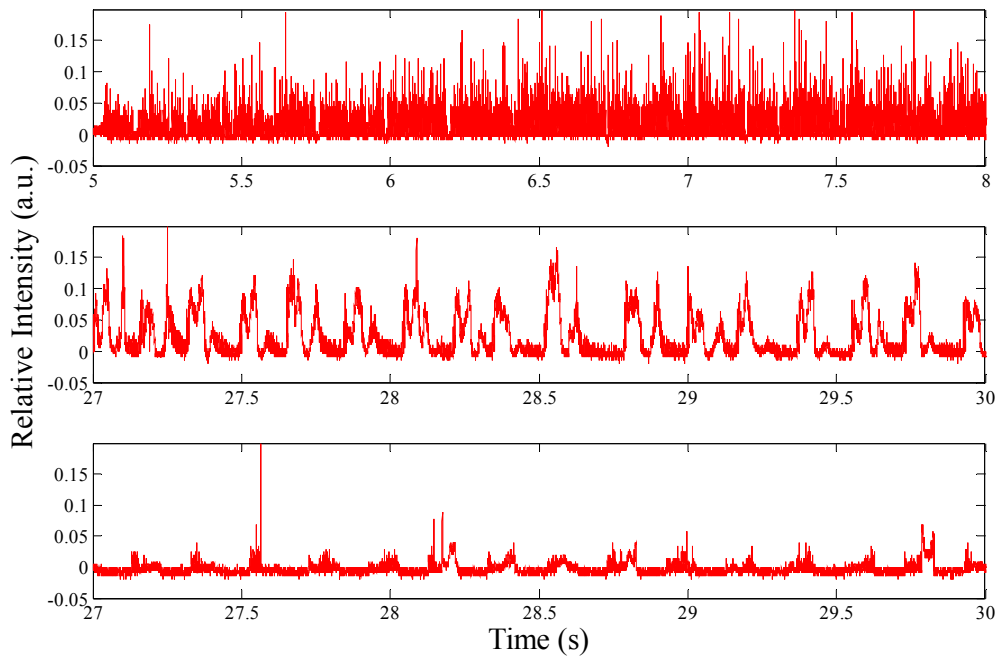


**Figure 8.21: Comparison of CW with pulsed laser welding; From top to bottom: 10 mm/s CW, 1 mm/s CW, 1 mm/s, 200 ms pulsing period, 50% duty cycle (100 ms pulse duration)**

By examining Figure 8.21, it is fairly obvious that there are three very different types of vapor/plasma signals. These signals are 3 second segments taken from the end of 30 mm welds. The top plot shows the 10 mm/s CW condition, the middle one shows the 1 mm/s CW condition and the lower one shows the 1 mm/s pulsed condition, with a 200 ms pulsing period and 50% duty cycle (100 ms pulse duration). The 10 mm/s CW welding has a pretty active signal, “spiking” at a very high frequency. These spikes are attributed to metal vaporization as the laser beam keeps moving over the thin molten front. Since the volume of the molten aluminum at the front of the keyhole is very small, the heat input from the laser cannot be transferred fast enough; as a result, there is a phase change and the material is vaporized. In rare occasions, the signal drops all the way down to zero and then resumes again. This might be attributed to the collapse of certain areas towards the bottom of the keyhole where it is very slender, and any small perturbation

can cause the molten metal walls to connect for a brief amount of time. However, the laser power is immediately absorbed and quickly opens up the keyhole by vaporizing the molten aluminum at that location.

Comparing this signal to the 1 mm/s CW signal, one can immediately tell the major difference. The signal is oscillating at a much lower frequency (between 5-10 Hz), and the signal drops down to zero for a significant period of time. This is a significantly different signal than what was observed in section 8.6.2, where the signal was very calm and had a low average value. The main difference is that the signal in Figure 8.9 was taken at a very early stage of the welding (first 8 seconds), whereas Figure 8.21 shows the signal towards the end of the 30 mm/s weld. The purpose of showing the later stage of the low speed welding signal is to show an additional phenomenon that has been observed. The 1 mm/s welding signal in Figure 8.21 shows periodic spikes occurring at a very low frequency. It is very possible that these major oscillations are due to violent boiling. As the process goes on, if the molten pool keeps absorbing the laser beam, it can easily become overheated and if it starts to boil, major vaporization would occur at a certain low frequency (unlike steady vaporization during keyhole welding). From the boiling a large amount of vapor will also escape, again being accompanied by melt ejection, and this could account for the high spikes in the signal.

Finally, the pulsed welding condition, has a much calmer signal overall. A closer look of the signal is shown in Figure 8.22. The signal oscillates at 5 Hz, but only because the laser is pulsing at that frequency. For the duration that the laser is on, the signal is very low with the exception of when the laser pulse is turned on. A very high spike can be seen at the beginning of the pulse. This can be associated with the adiabatic drilling that occurs at the beginning of the laser pulse (Harp et al., in review). After the keyhole has been formed and stabilized to the maximum depth, the signal reduces significantly. Again, this evidence supports the hypothesis, because by reducing the average power by

half, we can prevent the molten pool from overheating and therefore avoid the violent eruptions. The main drawback to the pulsed welding mode is that there were major solidification cracks observed in the welds, which compromises their structural integrity.

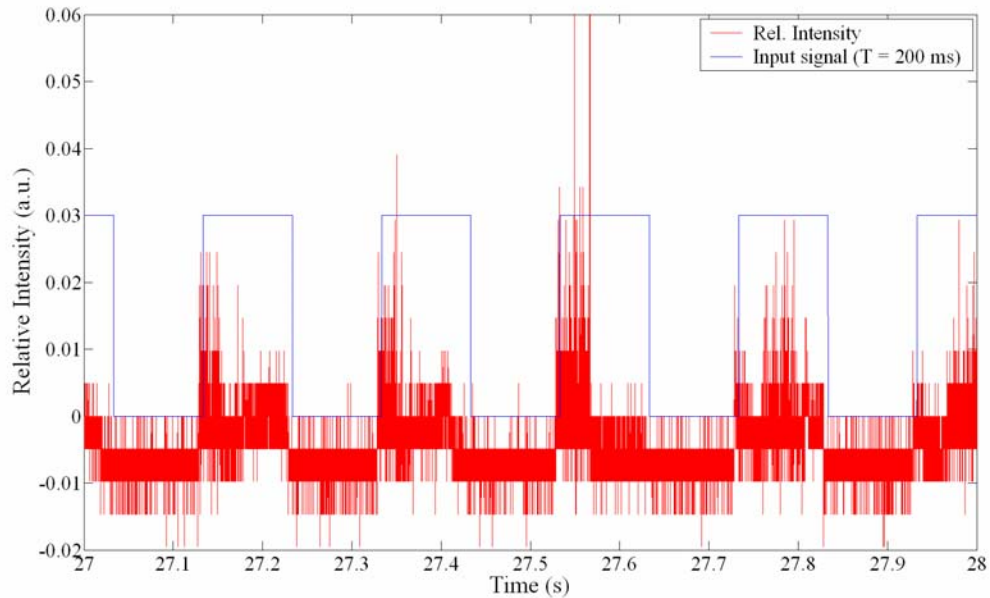


**Figure 8.22: A closer look at the pulsed welding vapor intensity (T = 200 ms)**

Figure 8.23 compares the cross-sections of these three welding conditions. It is pretty apparent that the 10 mm/s CW condition has a nice conical weld cross-section without major defects, the 1 mm/s weld is wider and shallower, containing large blowholes and the 100 ms pulsed weld has a nice conical, high aspect ratio, cross-section, but contains major solidification cracks.

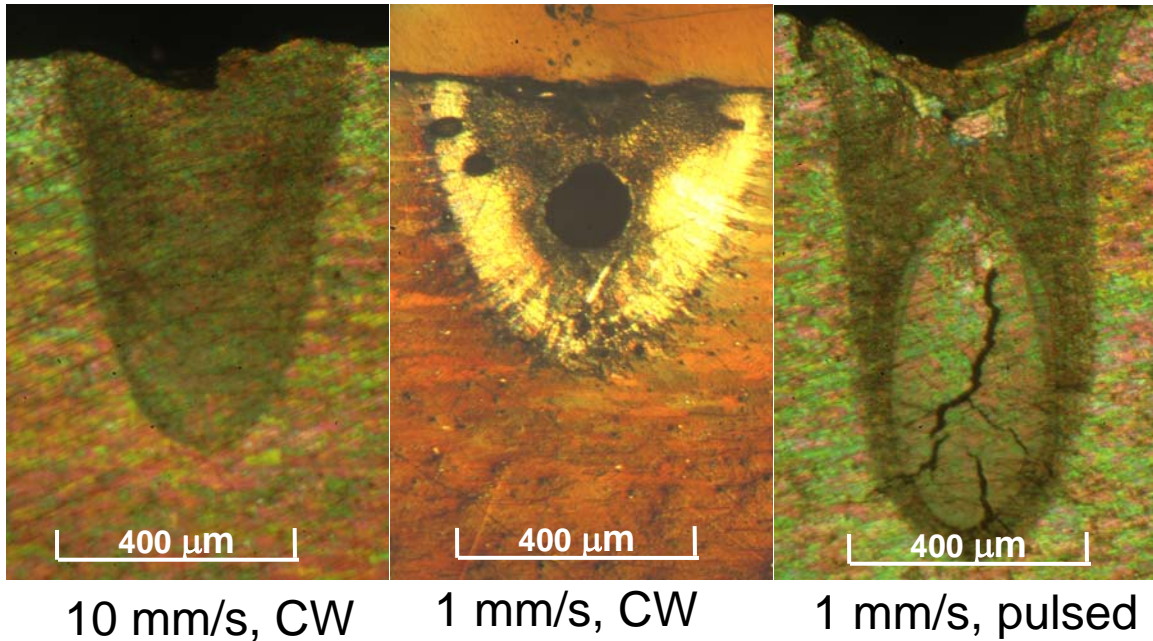


**Figure 8.23: Cross-sections for 10 mm/s CW, 1 mm/s CW and 100 ms pulsed welding conditions**

This is how the third hypothesis was formed. It is of interest to attempt to eliminate the solidification cracks, by still keeping the average power lower than the CW mode, but at the same time, reducing the cooling rate, by never completely shutting off the laser.

### **8.8 *Non-zero Low Power Pulsing Tests as a Potential Solution to Solidification Cracking***

Figure 8.24 shows the pulsing experiments performed with a non-zero low power (percentage of the maximum available power). The idea is to use the high pulsing power to create an efficient, high aspect ratio, good quality weld and reduce to a low power to prevent the overheating of the molten pool, and at the same time reduce the large temperature gradients by maintaining a certain level of heat input.

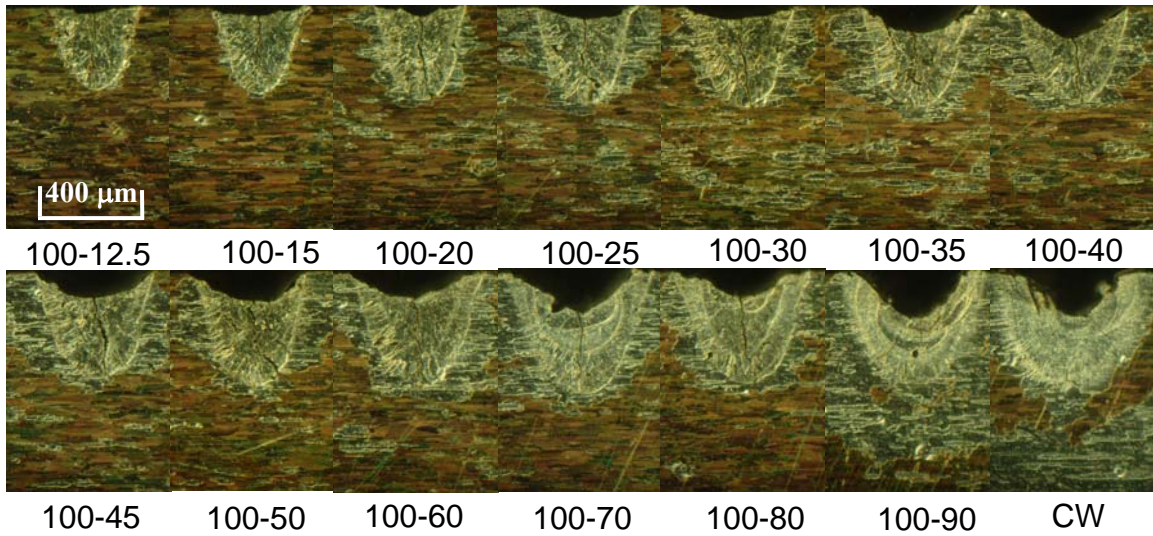


**Figure 8.24: Pulsed Welding Cross-Sections for 10 ms Pulse Duration Welds with Various Low Power Percentages Ranging from 12.5-90 %**

By inspecting the pictures in Figure 8.24, it is pretty clear that the problem was not solved except for the 90% “low” power condition. However, this cross-section closely resembles the CW condition with severe underfill.

Other solutions exist to solve the solidification problem, however, this is a far from trivial problem and beyond the scope of the thesis. Some of the techniques used to prevent solidification cracking include adding filler metal to fill the gap, having a trailing laser beam to reduce the temperature gradient and different laser scanning techniques that slow down the cooling. Further discussion on how to eliminate solidification cracking will be discussed in the Future Work section.

## **8.9 Thin Sheet Full Penetration Laser Welding for Crack Repair**

While pulsed welding seemed to confirm the hypotheses, the solidification cracking in the pulsed welding experiments was far too big of an obstacle to overcome and hence the best CW welding conditions achieved in the process characterization part of this study were preferred to be applied to the thin sheets, in order to try and achieve full penetration welding for crack repair. The best parameters (10 mm/s, ~ 1 mm focused into the surface) yielded a penetration between 800 and 900  $\mu\text{m}$  and the weld had a nice conical shape, absent of major defects, other than a slight amount of underfill. Before attempting to repair fatigue cracks in thin sheets, it was deemed appropriate to create bead-on-plate welds in the thin sheets to ensure that the process parameters would produce similar results.

Unfortunately, at first these parameters produced a very violent process which resembled laser cutting rather than laser welding (Figure 8.25). It was the first indication that the thickness of the workpiece is a significant parameter in laser welding, when its dimension approaches that of the weld penetration depth of the process. From a first observation, it seemed there were two major reasons why the results were so different from results in thicker workpieces: a) the thicker sheets provided a larger heat sink and therefore the thinner workpieces required less power to melt all the way through, and b) in full penetration mode, due to the lowered viscosity of aluminum at elevated temperatures, the surface tension forces on the bottom of the workpiece were not strong enough to counteract gravity and the pressure from the shielding gas (Ready, 2001).

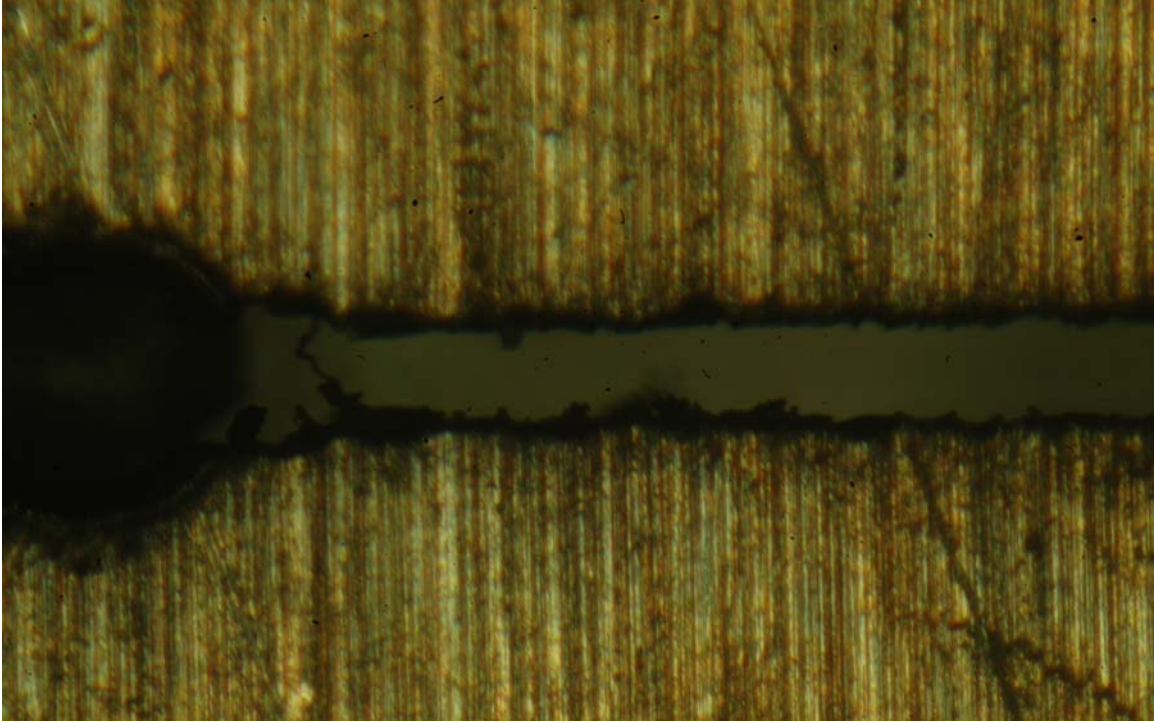


**Figure 8.25: Top view of first attempt of a thin sheet, full penetration, bead-on-plate weld**

### *8.9.1 Process Uncertainty in Full Penetration, Thin Sheet, Bead-on-Plate Laser Welding*

Since it was pretty clear that thin plate, full penetration laser welding was not going to be as simple as transferring the best parameters from partial penetration welding, it was imperative to go through an experimental investigation in order to determine the best parameters.

At first glance the adjustable parameters affecting laser welding are: a) power, b) processing speed, c) focusing, d) shielding gas pressure and e) nozzle position. From previous experience it has been determined that the best way to evaluate the effect of a

particular parameter was to vary it while holding all other parameters constant. Since the transferred welding conditions from partial penetration welding yielded results resembling laser cutting, it made the most sense to first increase the distance between the nozzle and the workpiece in order to decrease the energy with which the nitrogen gas hits the molten pool. This changed the process from resembling laser cutting to welding. This result confirmed the suspicion that the high flow rate of the shielding gas was acting like an assist gas for laser cutting. By raising the nozzle (~ 3 mm from the surface of the workpiece), the pressure applied by the nitrogen gas to the molten pool was reduced significantly, while still maintaining its shielding from the atmosphere.

However, the resulting weld still did not have the desired weld characteristics from beginning to end; namely, consistent width, smooth top and bottom beads and minimal underfill. The weld would start out having the desired consistency and shape and after 20 or 30 millimeters would transition into a violent, unstable process. In this part of the weld the width was extremely inconsistent, the top bead experienced severe underfill and the bottom bead had significant drop out (Figure 8.26).

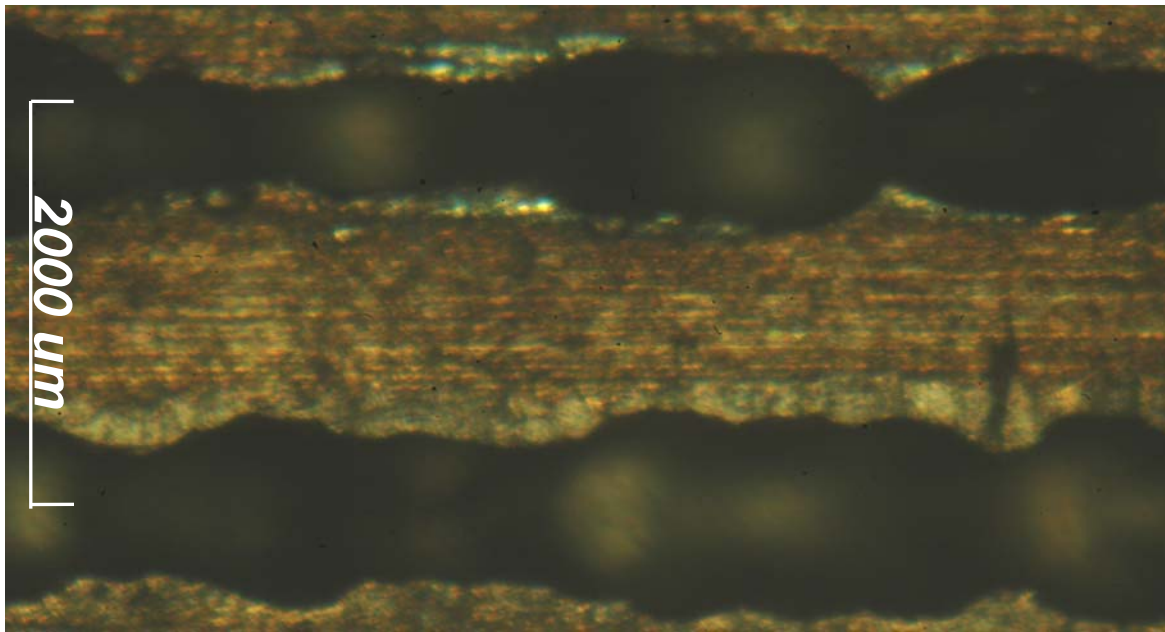


**Figure 8.26: Top view of inconsistent, thin-sheet, full penetration, bead-on-plate welds**

Also, inconsistencies were observed when creating several welds side by side without changing the processing conditions (Figure 8.27).

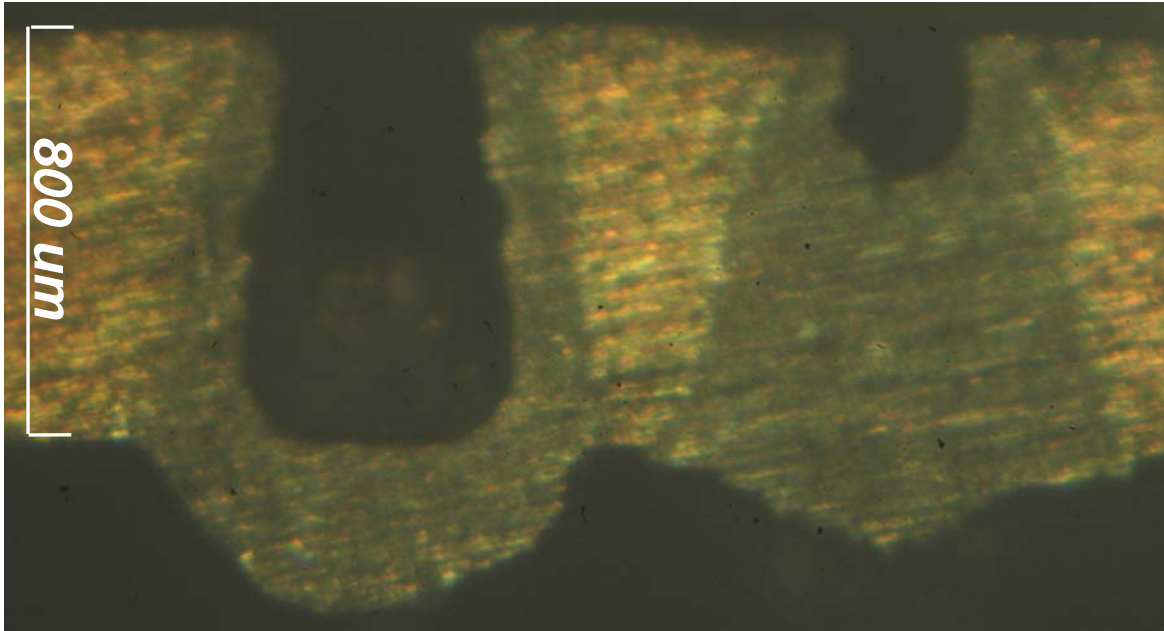


**Figure 8.27: Cross-sectional view of inconsistent, thin sheet, full penetration, bead-on-plate welds**

These results raised the suspicion that there were additional not so obvious parameters affecting the welding results such as the distortion of the workpiece from the machining (shearing) they have been subjected to. This distortion is much more pronounced in thinner workpieces compared to the thicker plates used for partial penetration welding experiments. Also, the distortion during the welding process, due to the thermal stresses, was more pronounced as well. Finally, the thin sheets had thickness differences due to their thickness tolerance (from the material supplier), which can affect the relative height of the workpiece with respect to focus position. The inconsistent results indicated that all these “hidden” parameters were affecting the process, which turned out to be much more sensitive to focusing changes than the partial penetration process. Therefore, the current fixturing method was inadequate (Figure 8.28).



**Figure 8.28: Initial fixturing method for thin sheet, full penetration, bead-on-plate welding**

In order to create consistent and repeatable results a certain degree of precision was required in the flatness of the sheet and the relative height of the top surface of the workpiece. To achieve this level of precision, the fixturing of the workpiece had to be altered. The solution was to “sandwich” the thin sheet between two thicker pieces, each of them having a rectangular slot to allow access to the thin sheet (Figure 8.29). The three pieces were held together by binder clips, ensuring that the middle sheet would be held as flat as possible. Also, .001 inch shims were used between the posts and the bottom fixturing plate to help level the workpiece. Finally, a height gage was used to measure relative height between the workpiece and a reference point, so the focusing could be adjusted accordingly to ensure consistency.



**Figure 8.29: Modified fixturing method for thin sheet, full penetration, bead-on-plate welding**

By ensuring the flatness to be within .0005 inches and adjusting the focusing based on the relative height of the workpiece, the resulting welds turned out to be much more consistent from beginning to end and at the ideal focusing position (~ 1 mm into the workpiece). The weld was created with minimal underfill and drop out and with a consistent width and defect free weld bead (Figures 8.30 and 8.31).

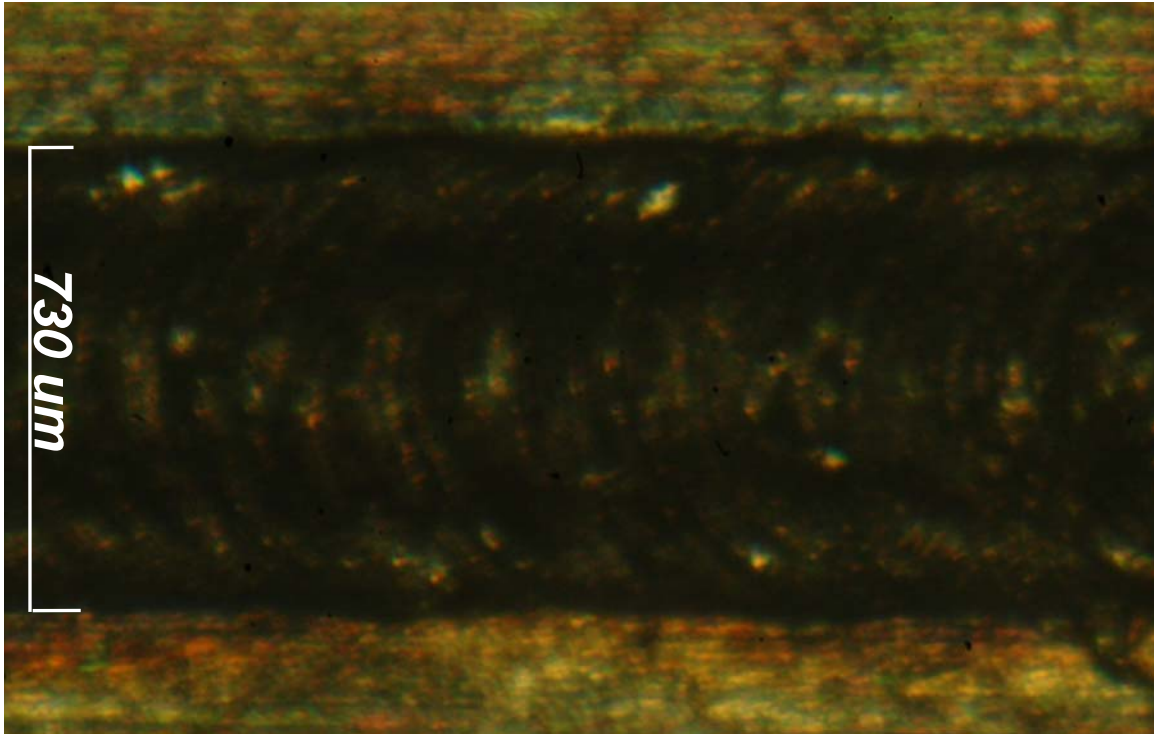


**Figure 8.30: Top view of consistent, thin sheet, full penetration, bead-on-plate weld**

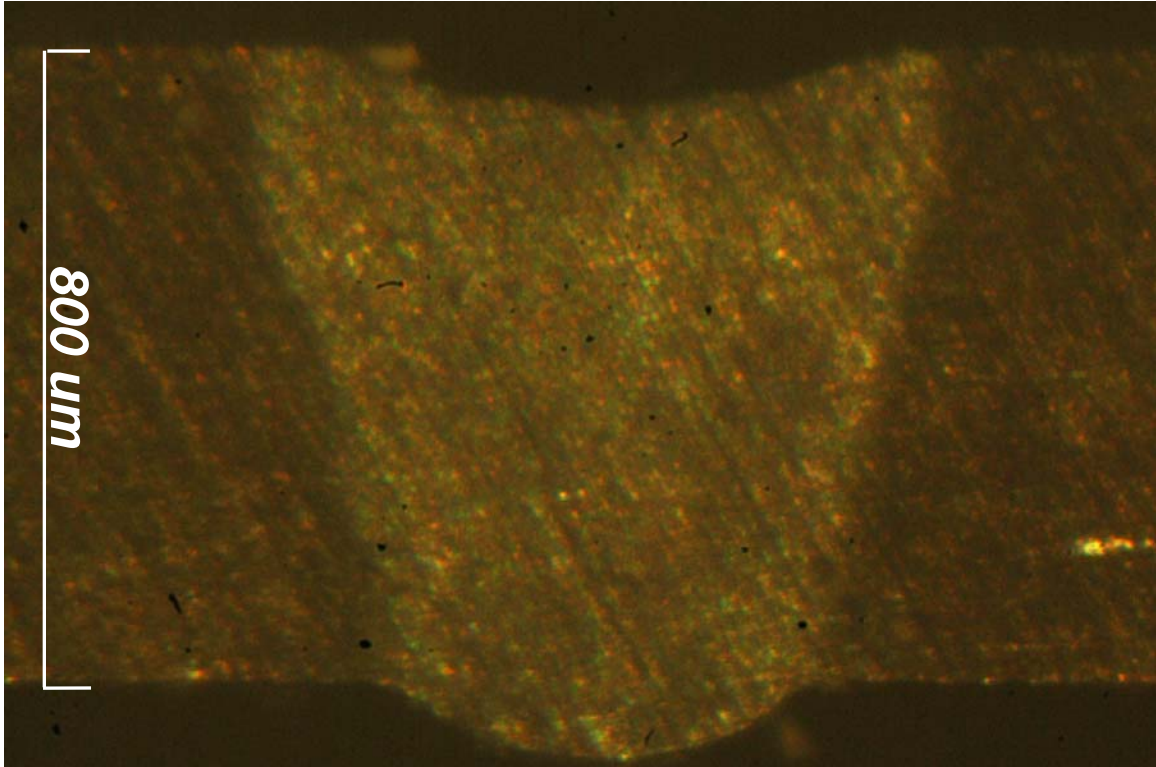


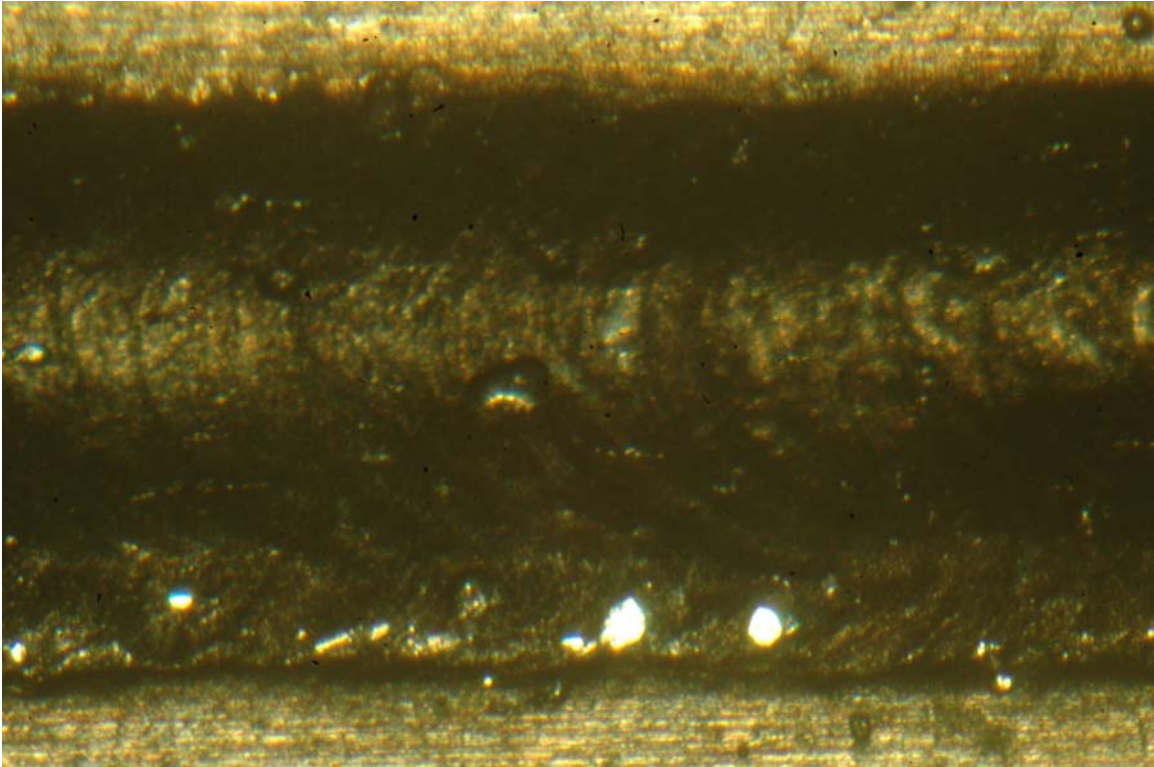
**Figure 8.31: Cross-sectional view of a consistent, thin sheet, full penetration, bead-on-plate weld**

### *8.9.2 Thin Sheet Crack Repair using Low Speed, Full Penetration Laser Welding*

Once successful thin sheet bead-on-plate welding was established, the next step was to apply it to the fatigue cracked plates. A manual crack tracking method was employed, by having the linear motor follow a particular path along the crack programmed using several “waypoints.”

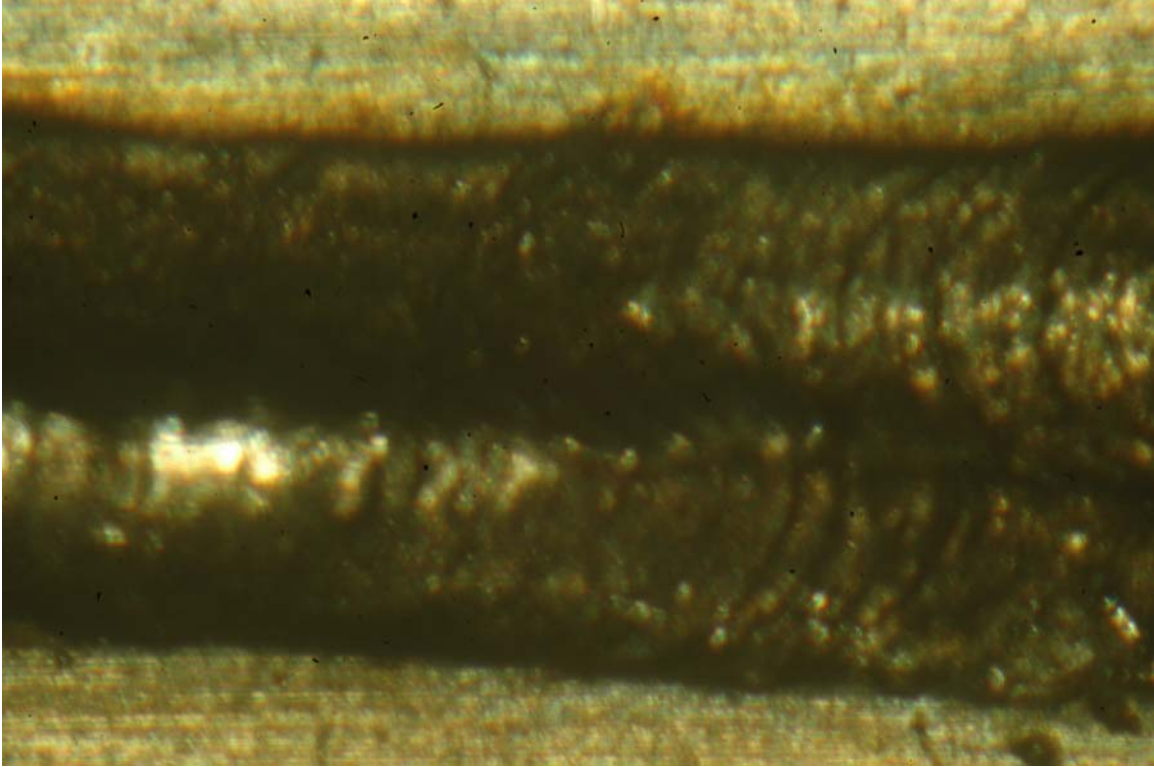
The initial objective was to create single-pass laser welds to achieve adequate crack fusion. Due to the added complexity of welding a joint, several welds did not turn out as consistent as the bead-on-plate welds. A single-pass laser welded crack is shown in

Figure 8.32. The added complexity of a joint (the crack itself) in laser welding, was the cause of a few weld inconsistencies. Therefore, there was a wide range of repaired crack results.



**Figure 8.32: Single-pass laser welded fatigue crack**

Double-pass laser welds were attempted as well, because it was found that for most cases, the single-pass weld widths were not wide enough. This was because the fatigue induced cracks did not propagate perpendicularly through the thickness of the sheets. Most cracks were angled to where they came through the other side of the plate at a significantly different position, therefore creating the necessity of a double-pass weld to ensure the complete fusion of the crack. A double-pass laser welded crack is shown in Figure 8.33.



**Figure 8.33: Double-pass laser welded fatigue crack**

### *8.9.3 Mechanical Testing: Bead-on-Plate Weld Strength and Repaired Crack Strength*

After full penetration welding of thin sheets was considered a success based on qualitative criteria (good consistent weld bead, no major defects, full penetration), the next objective was to characterize them quantitatively. Even though rigorous mechanical testing was out of the scope of this research study, it was worth comparing the weld's ultimate tensile strength (UTS) to that of the base metal, in order to determine approximately how much of the overall strength was lost due to the destruction of the heat treatment temper.

Tensile tests were conducted on base AA 7075-T6, single and double bead-on-plate welds (in the transverse direction of the weld). The results are shown in Figure 8.34.

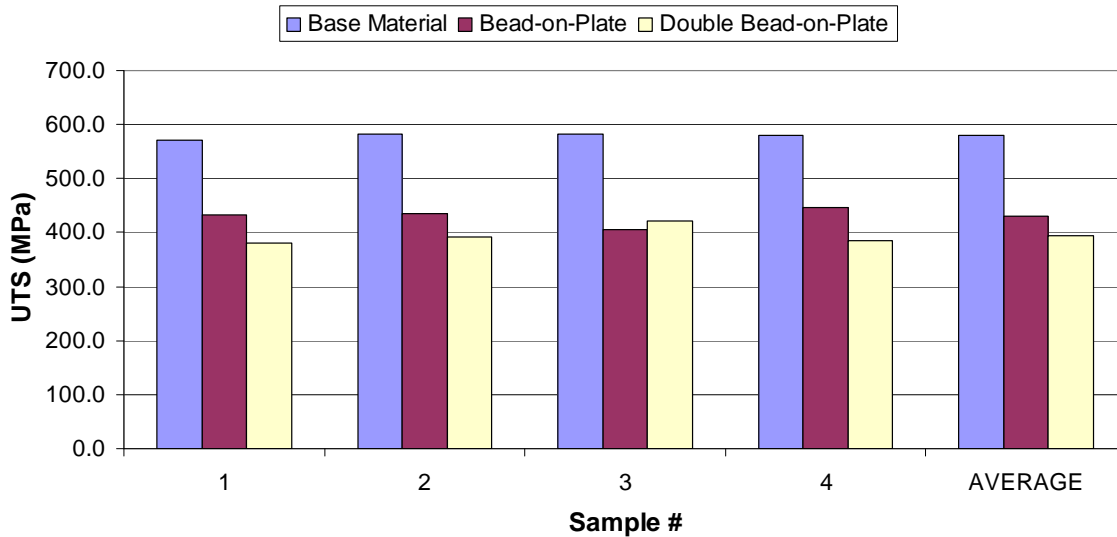


**Figure 8.34: Base AA 7075-T6 compared to single and double pass bead-on-plate welds**

The average UTS of the base AA 7075-T6 was approximately 579.4 MPa, which is within 0.4 MPa of the documented value (Sanford, 2003). The average UTS of the single-pass bead-on-plate weld was approximately 429.9 MPa, which is 74 percent of the base alloy's strength. The results for the double bead-on-plate welds were slightly lower, approximately 394.7 MPa, or 68 percent of the base alloy's strength. These values are extremely encouraging since the UTS for AA 7075-O, which is the pre-heat treatment alloy, is only 220 MPa (Sanford, 2003), which means that the laser did not completely destroy the heat treatment temper.

In addition to tensile strength, the overall strain was measured, in order to get a basic sense of ductility. The average elongation for the base alloy was measured to be approximately 4.9 percent, while the single bead-on-plate was just under 1 percent and

the double bead-on-plate was approximately 0.5 percent. While measuring the overall elongation is not as accurate a method as placing a strain gage on the weld and measuring its strain, it still shows that when a weld is created, there is a significant drop in ductility. Furthermore, when there is a second bead-on-plate pass and some of the material is remelted, the ductility drops even further. This effect has been observed before (Verkat et al., 1997) in laser welding and can be improved slightly with the appropriate addition of filler wire (Yoon and Wallach, 2008).

Finally, the best sections of single and double pass fatigue crack repairs were selected and subjected to tensile tests in order to evaluate the effectiveness of the process on crack repair. The best result was a double pass weld, which fused the crack sufficiently to achieve UTS of approximately 75 percent of the base alloy. Also, its elongation was approximately 0.4 percent. The single pass crack repairs were not as effective because the weld thickness was not large enough to cover the angling of the cracks. The best UTS was approximately 38 percent of the base alloy. This means that there was a significant section of the crack that was never fused.

The results from this section are extremely encouraging because they show that full penetration, low speed laser welding could possibly be used effectively as part of a solution to prolong the fatigue life of a cracked aluminum alloy part. The strength of the heat-treatable alloy can be recovered up to approximately 75 percent, while eliminating any high stress concentration areas caused by the crack front. The remaining strength can be recovered by applying a composite patch on top of the welded section.

## 9 SUMMARY

There were four major research objectives associated with this project. The main objective was to characterize the process of low speed fiber laser welding of AA 7075-T6. For each speed, penetration depth increased as the beam was focused further into the workpiece, until it reached 1 mm. Also, as the processing speed decreased, penetration depth increased, as expected, down to a certain threshold, 1 mm/s, where it deviated from the theoretical prediction. At the same time the process efficiency, i.e. how well the input energy translates to a desirable weld, gradually decreased.

The first hypothesis was formed based on observations from online vapor intensity measurements, as well as data obtained from post processing (cross-sectioning), which suggested that during low speed laser welding, the temperature of the molten pool increased and therefore absorbed the laser beam more efficiently. This reduced the effectiveness of the Fresnel absorption because the reflected laser beam components were significantly reduced. This means that the bottom of the keyhole did not have enough power density to create enough vaporization and therefore pressure to maintain a deep keyhole. At the same time the molten pool would overheat and sometimes cause violent boiling, which caused large blowholes in the center of the weld. Another observed effect was that at lower speeds, the reflectivity of the laser beam increased as compared to higher speed welds. This happened because the keyhole was wider and shallower and could not trap the laser beam as efficiently, causing a good portion of it to reflect back out.

The hypothesis of the second objective was tested by creating pulsed welds at the same low processing speed (1 mm/s), which reduced the average power by half. This prevented the molten pool from overheating and the resulting cross-sections showed that

the penetration was significantly deeper and free from the large blowholes. The difference in the process was also evident in the photodiode measurements, where the signal is much calmer and of much lower intensity.

However, there was a different problem that arose with pulsed welding, namely, the presence of solidification cracks. Usually, this type of crack occurs when the cooling rate is very high and the contraction stresses from the solidified part of the melt pool are too high for the weld bead to resist. The third research objective was to try to reduce the cooling rate of the molten pool by reducing the power to a lower value, rather than shutting it off completely. Several tests were conducted with different low power values ranging from 12.5 percent to 90 percent. The cross-sections of these welds showed that the solidification cracking problem was not solved using this method, except in the 90 percent condition. However, these welds exhibited some of the problems associated with CW welding and was not deemed a viable solution.

The final objective of this research was to find out if low speed fiber laser welding could be used to create full penetration welds that could be applied to fatigue crack repair. Since the pulsed welds were deemed unreliable due to the solidification cracks, the 10 mm/s, CW condition was selected due to its comparable penetration depth to the thickness of the cracked samples (0.8 mm). Full penetration welding presented additional complexities, such as increased sensitivity to focus position, which had to be overcome with increased precision in the setup, to ensure process repeatability and consistency. After this happened, successful full penetration bead-on-plate welds were created and their UTS proved to be approximately 75 percent of the base material. This result is extremely encouraging because it means that the welds have not completely lost the added strength that the heat treatment temper adds. Ductility, however, did decrease significantly, which is a characteristic of welded joints. The full penetration welding was applied to fatigue cracks by a simple “waypoint” tracking method. The added joint

complexity of the crack created some inconsistencies in the welds, but the small sections that were welded successfully proved to have similar strength to the average bead-on-plate welds. Since the cracks did not propagate perpendicularly through the thickness of the workpiece, it was necessary to increase the weld width by overlapping another weld pass.

## 10 FUTURE WORK

This research has revealed several possible fronts for future research. This includes further investigation into low speed laser welding, pulsed welding and application of low speed laser welding to crack repair.

In this research we have characterized the process change that happens when the laser welding processing speed drops too low. Evidence from online observations as well as post processing results from both CW and pulsed welds suggests that the molten pool's efficiency increases as the molten pool's temperature increases, which leads to reduced Fresnel absorption, less penetration and eventually boiling of the molten pool. The next research step can be to use a high speed camera to observe the movement of the molten pool (using certain illumination techniques) and correlate it to the measured signals from the photodiode. In addition, the molten pool temperature could be monitored using IR temperature sensors (pyrometers). After this analysis, photodiode signal characteristics could be qualitatively identified, and the next step could possibly be a closed loop power control scheme that depends on the molten pool temperature and the photodiode signal characteristics. This could provide a means to control the temperature of the molten pool, to where it enhances Fresnel absorption.

Another possible research study could be focused on solving the solidification cracking problem during pulsed welding. A technique that could possibly help reduce the cooling rates of the molten pool and hence eliminate solidification cracks is pulse shaping, where the power could gradually be turned down with slopes of different gradients, so as the molten pool solidifies more uniformly. Another method that could work would be to use a trailing laser beam that is set at a lower power and could ensure that the molten pool temperature would not cool down too rapidly. Finally, adding filler metal could also help

reduce the cracking by allowing the excess metal to fill the gaps where the cracks usually form.

Finally it is of interest to improve the full penetration welding application to fatigue cracks. A crack tracking method could be employed to where the laser beam follows the crack precisely and therefore fuses it more effectively. Once this is done, the mechanical properties (transverse and longitudinal tensile tests, weld hardness, ductility, etc.) of the weld could be studied more extensively, including experiments investigating the fatigue life of the repairs. The final step would be to determine how effective the fused crack repair technique would be in combination with the application of a composite patch.

## 11 REFERENCES

Allen, C. M., Verhaeghe, G., Hilton, P. A., Heason, C.P., Prangnell, P.B., 2006. "Laser and hybrid laser-MIG welding of 6.35 and 12.7mm thick aluminium aerospace alloy," *Materials Science Forum*. 519-521, (2), pp.1139-1144.

Barthélemy, O., Margot, J., Chaker, M., Sabsabi, M, Vidal, F., Johnston, T.W., Laville, S., Le Drogoff, B., 2005, "Influence of the laser parameters on the space and time characteristics of an aluminum laser-induced plasma," *Spectrochimica Acta Part B*, 60, pp. 905-914.

Bengoechea, J., Aguilera, J.A., Aragón, C., 2006. "Application of laser-induced plasma spectroscopy to the measurement of Stark broadening parameters," *Spectrochimica Acta Part B* 61. pp. 69-80.

Brown, R. T., 2008. "Keyhole welding studies with a moderate-power, high brightness fiber laser," *Journal of Laser Applications*, 20 (4), pp 201-208.

Cao, X., Wallace, W., Immarigeon, J.-P., and Poon, C., 2003, "Research in Laser Welding of Wrought Aluminum Alloys. I. Laser Welding Processes," *Materials and Manufacturing Processes*, 18(1), pp. 1-22.

Cao, X., Wallace, W., Immarigeon, J.-P., and Poon, C., 2003, "Research in Laser Welding of Wrought Aluminum Alloys. II. Metallurgical Microstructures, Defects, and Mechanical Properties," *Materials and Manufacturing Processes*, 18 (1), pp. 23-49.

Carslaw, H. S., Jaeger, J. C., 1962, Conduction of Heat in Solids, 2<sup>nd</sup> edition, Oxford: Clarendon, pp. 390.

Cieslak, M. J., 1992, "Phase Transformations in Weldments: New materials and New Perspectives," 3<sup>rd</sup> Int. Conf. on Trends in Welding Research, Gatlingburg, TN, pp. 229.

Dausinger, F., Rapp, J., Beck, M., Faisst, Hack, R., Hugel, H., 1996, "Welding of Aluminum: A Challenging Opportunity for Laser Technology," *Journal of Laser Applications*, Vol. 8, 285-290.

Dausinger, F., Rapp, J., Hohenberger, B., Hugel, H, 1997, "Laser Beam Welding Of Aluminum Alloys: State Of The Art And Recent Developments," *Proc. Int. Body Engineering Conf. IBEC '97: Advanced Technologies & Processes*, Vol. 33, pp. 38-46.

Dawes, C., 1992, Laser Welding, 1<sup>st</sup> edition, McGraw-Hill, Inc., pp. 74-76.

Duley, W. W., 1999, Laser Welding, 1<sup>st</sup> edition, John Wiley & Sons, Inc., pp. 4-65.

Freudenstein, S., Cooper, J., 1979. "Stark Broadening of Fe I 5383 Å," *Astron. Astrophys.* 71. pp. 283-288.

Gaumann, M., Kurz, W., 1998, "Why is it so difficult to produce an equiaxed microstructure during welding," *Math. Model. Weld. Phenom.* 4 (695), pp. 125-136.

Griem, H.R., 1964. Plasma Spectroscopy, 1<sup>st</sup> edition. pp. xx-xx. McGraw-Hill, New York.

Guitierrez, L. A., Neye, G., Zschech, E., 1996, "Microstructure, Hardness Profile and Tensile Strength in Welds of AA6013 T6 Extrusions," *Welding Journal*, 75 (4), pp. 115S-121S.

Harp, W.R., Paleocrassas, A.G., Noguchi, S., Tu, J.F. and Ohmura, E, "On the Mechanisms of Laser-Material Interaction in Microsecond Laser Ablation," (in review)

Hirose, A., Kobayashi, K., Yamaoka, H., Kurosawa, N., 1999, "Evaluation of properties in laser welds of A6061-T6 aluminium alloy," *Journal of Light Metal Welding & Construction*, 37 (9), pp. 1-9.

Ion, J. C., 2000, "Laser beam welding of wrought aluminium alloys," *Sci. Technol. Weld. Joining*, 5 (5), pp. 265-276.

Ion, J.C., Jokinen, T., Salminen, A., Kujanpaa, V., 2001, "Laser beam welding using filler wire," *Ind. Laser Solutions Manuf.*, 16 (2), pp. 16-18.

Katayama, S., Mizutani, M., 2002, "Laser Weldability of Aluminum Alloys," *Trans. JWRI*, 31 (2), pp. 147-155.

Katayama, S., Mizutani, M., Matsunawa, A., 2003, "Development of Porosity Prevention Procedures during Laser Welding," *Proc. of SPIE*, Vol. 4831: 281-288.

Katayama, S., Nagayama, H., Mizutani, M., Kawahito, Y., 2008. "Fiber laser welding of aluminum alloy," *Keikinzoiku Yosetsu/J. of Light Metal Welding and Construction*, 46 (10). pp. 34-43.

Kim, J.D. and Matsunawa, A., 1996, "Plasma Analysis in Laser Welding of Aluminum Alloys," International Institute of Welding, pp. 1-9.

Kim, J.D., Oh, J.S., Lee, M.H., Kim, Y.S., 2004, "Spectroscopic Analysis of Plasma Induced in Laser Welding of Aluminum Alloys," Material Science Forum, 449-452, pp. 429-432.

Knudtson, J.T., Green, W.B., Sutton, D.G., 1987, "The UV-visible spectroscopy of laser-produced aluminum plasmas," J. Appl. Phys. 61 (10), pp. 4471-4780.

Kou, S., 2003, Welding metallurgy, 2<sup>nd</sup> edition, Hoboken, N.J., Wiley-Interscience, pp.1-197.

Kutsuna, M., Yan, Q. U., 1998, "Study on porosity formation in laser welds of aluminium alloys (Report 2). Mechanism of porosity formation by hydrogen and magnesium," J. Light Met. Weld. Constr., 36 (11), pp. 1-17.

Lankalapalli, K. N., Tu, J. F., Gartner, M., 1996, "A model for estimating penetration depth of laser welding processes," J. Phys. D, Appl. Phys., 29, pp. 1831-1841.

Lenk, A., Witke, T., Granse, G., 1996, "Density and electron temperature of laser induced plasma – a comparison of different investigation methods," Applied Surface Science, 96-98, pp. 195-198.

Lu, Y.F., Tao, Z.B., Hong, M.H., 1999, "Characteristics of Excimer Laser Induced Plasma from an Aluminum Target by Spectroscopic Study," Jpn. J. Appl. Phys, 38, pp. 2958-2963.

Mandal, N. R., 2002, Aluminum Welding, 1<sup>st</sup> edition, Narosa Publishing House, pp. 1-19

Martukanitz, R. P., Smith, D. J., 1995, "Laser beam welding of aluminum alloys," Proc 6<sup>th</sup> Int. Conf. on Aluminum Weldments, AWS, pp. 309-323.

Matsunawa, A., 1994, "Defects Formation Mechanisms in Laser Welding and Their Suppression Methods," Proc. of ICALEO, pp. 203-219.

Matsunawa, A., Katayama, S., Fujita, Y., 1998, "Laser Welding of Aluminum Alloys— Defects Formation Mechanisms and their suppression methods," Proc. 7<sup>th</sup> Int. conf./INALCO '98: Joints in Aluminum, Cambridge, pp. 65-76.

Miyamoto, I., Park, S.-J., Ooie, T., 2003, "Ultrafine-Keyhole Welding Process Using Single-Mode Fiber Laser," Proc. of ICALEO: 203-212.

Molian, A., 2004, Private conversation.

Naeem, M and Lewis, S., 2006. "Micro joining and cutting with a single mode fiber laser," Proc. of PICALO 2006, pp. 400-405.

NIST Atomic Spectra Database, March 2009,  
<<http://physics.nist.gov/PhysRefData/ASD/>>

Oi, J.F., Tian, S., Chen, H., Xiao, R.S., Zuo, T.C., 2006. "Slab CO<sub>2</sub> laser welding of 7075-T6 high strength aluminum alloy," Zhongguo Jiguang/Chinese J. of Lasers, 33 (SUPPL). pp. 439-444.

Park, S. J., 2005, Private conversation.

- Paleocrassas, A.G. and Tu, J.F., 2007, "Low-speed laser welding of aluminum alloy 7075-T6 using a 300-W, single-mode, ytterbium fiber laser," 86 (6), pp. 179.s-186.s.
- Poueyo-Verwaerde, A., de Frutos, A.M., Orza, J.M., 1993. "Experimental study of laser-induced plasma in welding conditions with continuous CO<sub>2</sub> laser," J. Appl. Phys. 74 (9). pp. 5773-5780.
- Ramasamy, S., Albright, C. E., 2000, "CO<sub>2</sub> and Nd:YAG laser beam welding of 6111-T4 aluminum alloy for automotive applications," J. of Laser Appl., 12 (3), pp. 101-115.
- Ready, J.F., 1971. Effects of High-Power Laser Radiation. 1<sup>st</sup> edition, Academic Press, New York-London, pp. 127-211.
- Ready, J. F. and Farson, D. F., 2001, LIA Handbook of Laser Materials Processing, 1<sup>st</sup> edition, Laser Institute of America (LIA), pp 307-424.
- Salminen, A. S., Kujanpaa, V. P., Moisio, T. J. I., 1994, "Effect of Use of Filler Wire on Requirements of Laser Welded Butt Joints," Proc. of ICALEO: 193-202.
- Sanford, R.J., 2003, Principles of Fracture Mechanics, 1<sup>st</sup> edition, Prentic Hall, pp. 386-387
- Sokolowski, W., Herziger, G., Beyer, E., 1988, "Spectral Plasma Diagnostics in Welding with CO<sub>2</sub> Lasers," SPIE 1020, pp. 96-102.
- Steen, W. M., 2003, Laser Material Processing, 3<sup>rd</sup> edition, Springer-Verlag London Limited, pp. 61-106.

Tourin, R.H., 1966. Spectroscopic Gas Temperature Measurement. 1<sup>st</sup> edition, Elsevier Publishing Company, Amsterdam-London-New York, pp. 41-57

Tu, J. F., 2005, Private conversation.

Tu, J.F., Inoue, T., Miyamoto, I., 2003. "Quantitative characterization of keyhole absorption mechanisms in 20 kW-class CO<sub>2</sub> laser welding process," J. Phys. D: Appl. Phys. 36, pp. 192-203.

Tu, J.F., Miyamoto, I., Inoue, T., 2002, "Characterizing keyhole plasma light emission and plasma plume scattering for monitoring 20 kW class CO<sub>2</sub> laser welding processes," J. Laser Applications, 14 (3), pp. 146-153.

Venkat, S., Albright, C.E., Ramasamy, S., Hurley, 1997, "CO<sub>2</sub> laser beam welding of aluminum 5754-O and 6111-T4 alloys," Welding Journal, 76(7), pp 275.s-282.s.

Wagner, F., 2006. "Laser beam welding with single mode fibre lasers," Proc. of PICALO 2006. pp 339-343.

Weeter, L., 1998, "Technological advances in aluminum laser welding," Pract. Weld. Today, 2 (1), pp.56-58

Xu, L., Tian, Z., Peng, Y., Xiao, R., Yang, W., 2008. "Microstructure and mechanical properties of high strength aluminum alloy laser welds," Zhongguo Jiguang/Chinese J. of Lasers, 35 (3), pp. 456-461

Yoon, J.W., Wallach, E.R., 2008, "CW CO2 laser welding of Al-Mg alloys with filler wires," *Material Science Forum*, 580-582, pp. 539-542.

Yoshikawa, M., Kurosawa, T., Nakata, K., Kimura, S., Aoki, S., 1995, "YAG Laser Welding of Aluminum Alloys," *Journal of Light Metal Welding & Construction*, 32 (9), 15-23.

Zhao, H., White, D. R., DebRoy, T., 1999 "Current issues and problems in laser welding of automotive aluminum alloys," *Int. Mater. Rev.*, 44(6): 238-266.

## REFERENCES

## ***1.1 Aluminum Grinding and Polishing***

All of the welding samples from the above experiments went through a cross-sectioning, grinding and polishing process. Cross-sections of the welds were taken at near the end of the weld (to ensure samples from a steady state of the process). These sections were taken as close to perpendicular as possible to the welding direction. The samples were then placed in a cylindrical mold and mixed with a special epoxy resin, to create a hardened sample that fits into the head of the grinder/polisher. The samples went through four grinding stages and two polishing stages achieving a mirror finish.

The grinding stages used 120, 320, 800 and 2400 (grains per square inch) grit paper subsequently to remove major scratches and make them smaller and smaller with each stage. The grinding stage uses water for lubrication. The force used was 30 N and the grinding wheel was at 300 rpm. The duration of each stage was 2 minutes.

The polishing stage uses two different special cloths in addition to a special lubricant containing 3 and 1  $\mu\text{m}$  sized particles which create a very fine polishing effect. The end result creates a mirror finish to the sample. The force used was 25 N and the polishing wheel was at 150 rpm. The duration of each stage was 5 minutes.

Finally, the samples are etched by placing them in a 0.25 N sodium hydroxide solution for 15 minutes and then rinsed and submerged in water for another 15 minutes. The sodium hydroxide solution chemically reacts differently with the base material and the weld cross-sections, distinguishing them from the rest of the material. The weld cross-sections are then examined under the microscope, photographed and measured when necessary.

This process is repeated for several cross-sections in order to get an average of the dimensions of each weld.

## 1.2 *Matlab Code*

### 1.2.1 *Aluminum Alloy 7075-T6 Penetration Model*

```

clear;
clc;

% Material Properties of Al 7075-T6

k = 130;           % Thermal conductivity in W/(m*K)
alpha = 48.36e-6; % Thermal diffusivity in m^2/s
Tv = 2773.15;     % Vaporization temperature in K

% Model constants

C = [.7557 142.2 -1.727e4 1.266e6 -4.524e7 6.167e8];

% Welding conditions

Pi = [.2488 .2799 .311 3.5 4 4.5] * 1e3; % Incident power in W
T0 = 293.15; % Ambient temperature in K

Pe0 = 2.5e-4:2.5e-4:2.5e-2

for i = 1:100

    for j = 1:6

        d(i,j) = (Pi(j) / (k * (Tv - T0))) * (1 / ((C(1) / 1) * Pe0(i)^(1-1) + (C(2) / 2) * Pe0(i)^(2-1) + (C(3) / 3) *
        Pe0(i)^(3-1) + (C(4) / 4) * Pe0(i)^(4-1) + (C(5) / 5) * Pe0(i)^(5-1) + (C(6) / 6) * Pe0(i)^(6-1)));

    end

end

hold on;
plot(Pe0, d(:,1), 'r-');
plot(Pe0, d(:,2), 'k-');
plot(Pe0, d(:,3), 'g-');
% plot(Pe0, d(:,4), 'k+');

```

```

% plot(Pe0, d(:,5), 'k. ');
% plot(Pe0, d(:,6), 'k*');
%title('Penetration in 7075-T6 at different powers (240 W, 270 W and 300 W)');
xlabel('Péclet number');
ylabel('Penetration (m)');
% gtext('300 W');
% gtext('270 W');
% gtext('240 W');

grid
hold off;

```

### 1.2.2 Temperature Distribution Model

```

clear;

clc;

T0 = 293.15;           % Ambient temperature (K)
Tv = 2573.15;        % Vaporization temperature (K)
Pe = 1;              % Péclet number

delta = .1;          % Plot area resolution parameter
range = 10;          % Plot axis maximum range

x = -range:delta:range; % Determination of X-axis range
y = -range:delta:range; % Determination of Y-axis range

lim = (2 * range / delta) + 1; % Number of data points

for i = 1:lim
    for j = 1:lim

        % Conversion to Polar Coordinates

        r(i,j) = sqrt(x(i)^2 + y(j)^2);

        if r(i,j) < 1

            r(i,j) = 1;

        end

        if (x(i) == 0) && (y(j) >= 0)

```

```

    theta(i,j) = pi/2;
elseif (x(i) == 0) && (y(j) < 0)
    theta(i,j) = -pi/2;
elseif (x(i) > 0) && (y(j) >= 0)
    theta(i,j) = atan(y(j)/x(i));
elseif (x(i) < 0) && (y(j) >= 0)
    theta(i,j) = pi - atan(y(j)/x(i));
elseif (x(i) < 0) && (y(j) <= 0)
    theta(i,j) = pi + atan(y(j)/x(i));
else
    % (x(i) > 0) && (y(j) < 0)
    theta(i,j) = 2*pi - atan(y(j)/x(i));
end

% Calculation of Temperature Distribution

summ(i,j) = 0;
for n = 0:10
    if n == 0
        en = 1;
    else
        en = 2;
    end
    summ(i,j) = summ(i,j) + en*(BesselI(n,Pe)/BesselK(n,Pe))*BesselK(n,Pe*r(i,j))*cos(n*theta(i,j));
end

T(i,j) = Tv - (Tv-T0)*(1-exp(-Pe*r(i,j)*cos(theta(i,j))))*summ(i,j);
end
end

% Generation of Contour Curves for Material's Melting Temperature

```

```

[X,Y] = meshgrid(x,y);
v = [1675.65 1725.65];      % Tm = 750.15-908.15 (avg = 829.15) Al 7075
contour(Y,X,T,v);
grid;
set(gca, 'XTick', [-range:1:range], 'YTick', [-range:1:range]);
% xlabel('x (normalized)');
% ylabel('y (normalized)');

```

### 1.2.3 SUS 304 Penetration Model

```

clear;
clc;

% Material Properties of SUS 304

k = 21.5;      % Thermal conductivity in W/(m*K)
% Cp = 500;    % Specific heat capacity in J/(kg*K)
% ro = 8000;   % Density in kg/m^3
alpha = 4.05e-6; % Thermal diffusivity in m^2/s
Tv = 3273.15; % Vaporization temperature in K

% Model constants

C = [2.1995 6.2962 -4.994 .0461];

% Welding conditions

Pi = [25 45 50 65 85 90 100 130 170 200]; % Incident power in W
T0 = 293.15; % Ambient temperature in K

lim = 5;
delta = 0.1;

Pe0 = 0:delta:lim;

for i = 1:lim/delta + 1

    for j = 1:10

        d(i,j) = (Pi(j) / (k * (Tv - T0))) * (1 / ((C(1) / 1) * Pe0(i)^(1-1) + (C(2) / 2) * Pe0(i)^(2-1) + (C(3) / 3) *
        Pe0(i)^(3-1) + (C(4) / 4) * Pe0(i)^(4-1)));

    end
end

```

```

end

% hold on;
% plot(Pe0, d(:,1), 'ro');
% plot(Pe0, d(:,2), 'ko');
% plot(Pe0, d(:,3), 'kx');
% plot(Pe0, d(:,4), 'k+');
% plot(Pe0, d(:,5), 'k. ');
% title('Penetration in SUS 304 at different powers (50-200 W)');
% xlabel('Péclet number');
% ylabel('Penetration (m)');
% gtext('300 W');
% gtext('270 W');
% gtext('240 W');

% grid
% hold off;

```

#### 1.2.4 Beam Profile

```

clear;
clc;

% P = [15 20 25 30];    % Corresponding Power Percentages
P = [39 53.5 72 97 119]; % Power settings in Watts

D(1) = 1;           % Normalization of Spot Diameters

for i = 1:3

    D(i+1) = sqrt(P(i+1)/P(1))*D(1); % Calculation of Normalized Spot Diameters

end

% Resulting Measurements of Half of Weld Length

x = [-6.831 -5.673 -3.585 -1.849 1.849 3.585 5.673 6.831];

% Depth Calculation
x = x.*sin(12.2*pi/180);

% Conversion to Radii (applying symmetry)
R(1) = D(4)/2;
R(2) = D(3)/2;
R(3) = D(2)/2;

```

```

R(4) = D(1)/2;
R(5) = D(1)/2;
R(6) = D(2)/2;
R(7) = D(3)/2;
R(8) = D(4)/2;

% plot(x,R,'x')          % Initial(Normalized) Plot Generation
% xlabel('x (mm)');
% ylabel('R (microns)');
% axis([-2 2 0 1]);

% Actual Radii Calculation
for i = 1:8

    realR(i) = abs(R(i)*5.4/.4872); % Min Spot Radius = 5.4 microns
                                % Vertex of Parabola = .4872
                                % (@ D = 0)

end

% Final ("Denormalized") Plot Generation
plot(x,realR,'x')
xlabel('Distance Away from Most Focused Spot (mm)');
ylabel('Spot Radius (microns)');
title('Spot Radius Variation as the Distance Away from the Most Focused Spot changes')
axis([-2 2 0 10]);
% grid;

```